Multi-wavelength study of waves and Solar atmospheric magneto-seismology

A thesis

submitted for the degree of

Doctor of Philosophy

in

The Department of Physics,

Pondicherry University,

Puducherry - 605 014, India

by

Sudip Mandal

Indian Institute of Astrophysics,

Bangalore - 560 034, India

July 2018

Multi-wavelength study of waves and Solar atmospheric magneto-seismology

Sudip Mandal
Indian Institute of Astrophysics

Indian Institute of Astrophysics
Bangalore - 560 034, India

Title of the thesis	:	**Multi-wavelength study of waves and Solar atmospheric magneto-seismology**
Name of the author	:	**Sudip Mandal**
Address	:	Indian Institute of Astrophysics II Block, Koramangala Bangalore - 560 034, India
Email	:	sudip@iiap.res.in
Name of the supervisor	:	**Prof. Dipankar Banerjee**
Address	:	Indian Institute of Astrophysics II Block, Koramangala Bangalore - 560 034, India
Email	:	dipu@iiap.res.in

Declaration of Authorship

I hereby declare that the matter contained in this thesis is the result of the investigations carried out by me at the Indian Institute of Astrophysics, Bangalore, under the supervision of Prof. Dipankar Banerjee. This work has not been submitted for the award of any other degree, diploma, associateship, fellowship, etc. of any other university or institute.

Signed: _____

Date: _____

Certificate

This is to certify that the thesis entitled **'Multi-wavelength study of waves and Solar atmospheric magneto-seismology'** submitted to the Pondicherry University by Mr. Sudip Mandal for the award of the degree of Doctor of Philosophy, is based on the results of the investigations carried out by him under my supervision and guidance, at the Indian Institute of Astrophysics. This thesis has not been submitted for the award of any other degree, diploma, associateship, fellowship, etc. of any other university or institute.

Signed: _____

Date: _____

List of Publications

1. **Mandal, S.** Samanta, T., Banerjee, D., Krishna Prasad, S., Teriaca, L., 2015, "Propagating Disturbances along fan-like coronal loops in an active region", *Research in Astronomy and Astrophysics*, 15,1832 *

2. **Mandal, S.**, Mayagar, N, Yuan, D, Doorsselaere, T. V., Banerjee, D., 2016, "Forward Modelling of Propagating Slow Waves in Coronal Loops and Their Frequency-Dependent Damping", *The Astrophisical Journal*, 820, 1 †

3. **Mandal, S.**, Yuan, D., Fang, X., Banerjee, D. Pant, V., Doorsselaere, T.V, 2016, "Reflection Of Propagating Slow Magneto-acoustic Waves In Hot Coronal Loops : Multi-instrument Observations and Numerical Modelling", *The Astrophisical Journal*, 828, 2 ‡

4. **Mandal, S.**, Krishna Prasad, S., Banerjee, D., 2018, "A Statistical Study on the Frequency-dependent Damping of Slow-mode Waves in Polar Plumes and Interplumes", *The Astrophisical Journal*, 853, 134 §

5. **Mandal, S.**, Banerjee, D., 2016, " Sunspot Sizes and the Solar Cycle: Analysis Using Kodaikanal White-light Digitized Data", *The Astrophisical Journal Letters*, 830, 2, L33

6. **Mandal, S.**, Hegde, M., Samanta, T., Hazra, G., Banerjee, D., Ravindra, B., 2017, "Kodaikanal Digitized White-light Data Archive (1921-2011): Analysis of various solar cycle features", *Astronomy and Astrophysics*, 601, A106

7. **Mandal, S.**, Chatterjee, S., Banerjee, D., 2017, "Solar Active Longitudes from Kodaikanal White-light Digitized Data", *The Astrophisical Journal*, 835, 62

8. **Mandal, S.**, Chatterjee, S., Banerjee, D., 2017, "Association of Plages with Sunspots: A Multi-Wavelength Study Using Kodaikanal Ca II K and Greenwich Sunspot Area Data", *The Astrophisical Journal*, 835, 158

*presented in Chapter 3
†presented in Chapter 4
‡presented in Chapter 5
§presented in Chapter 6

9. Chatterjee, S., **Mandal, S.**, Banerjee, D., 2017, "Variation of Supergranule Parameters with Solar Cycles: Results from Century-long Kodaikanal Digitized Ca II K Data", *The Astrophisical Journal*, 841, 70

10. **Mandal, S.**, Chatterjee, S., Banerjee, D., 2017, "Association of Supergranule Mean Scales with Solar Cycle Strengths and Total Solar Irradiance", *The Astrophisical Journal*, 844, 24

11. **Mandal, S.**, Karak, B.B., Banerjee, D., "Latitude Distribution of Sunspots: Analysis Using Sunspot Data and A Dynamo Model", *The Astrophisical Journal*, 851, 70

Presentations

1. Oral presentation in the *IBUKS meeting* held at the KU Leuven, Belgium, during 13-19 June 2016.

2. Oral presentation in the *IAU340: Long term datasets for the understanding of solar and stellar magnetic cycles* held at Jaipur, India, during 19-24 February 2018.

3. Poster presentation in the *Dynamic Sun I: MHD Waves and Confined Transients in the Magnetised Atmosphere* held at the Indian Institute of Technology, Varanasi, India, during 22-26 February 2016.

4. Poster presentation in the *Astronomical Society of India meeting 2016 (ASI:2016)* held at the Kashmir University, Kashmir, India, during 5-10 May 2016.

5. Poster presentation in the *Hinode-10 meeting* held at the Nagoya University, Nagoya, Japan, during 5-9 September 2016.

6. Poster presentation in the *Hinode-9 meeting* held at the Queens University, Belfast, Northern Ireland, UK, during 10-14 November 2015.

7. Poster presentation in the international conference on the *Coupling and Dynamics of the Solar Atmosphere* held at the IUCAA, Pune, India, during 10-14 November 2014.

Acknowledgements

First and foremost, I offer my sincerest gratitude to Prof. Dipankar Banerjee, my thesis supervisor, who has been a constant source of support and inspiration for me during the entire time of my Ph.D tenure. His constant encouragement in exploring different fields of solar physics kept me going during all these years. Apart from research, we both have a common interest *i.e* sport. We had spent a considerable amount of time together in discussing and watching cricket or football matches :-) .

Many thanks to Dipu Da's research group members for their valuable inputs during various group meetings. Also special shout-outs to Tanmoy and Krishna Da for their immense help during my first research project.

I would like to thank the director, IIA and all the academic and admin staff of IIA for providing a research friendly atmosphere. I would also like to thank my doctoral committee members and the staff at the Pondicherry University for their timely help and relevant suggestions.

A special thanks to Mr. Fayaz and Mr. Ashok for me helping me out in computer related issues whenever I needed. Special thanks to Yogesh (the 'auditorium guy' :-)) and Murli sir (retd. IIA stuff) who gave me the name 'dada'.

During my tenure in IIA, I met lot of people (including some project students). Though I may not remember all the names but all of them have made my stay at IIA memorable. I have always been a sport enthusiast and my time at IIA was no exception. I played a lot of games in our 'hugely-small', 'multi-purpose' IIA ground. I feel amazed now that how we could manage to play volleyball, cricket, football, badminton in that same ground. I must mention some of the amazing players I have played with: Selvan sir, Mohan Sir, Anand Choubey, Anand

MN, Yogesh, Suresh Angdi, Sajal da, Varun, Sandeep, Avinash, Priyanka, Panini, Bhumika, Manoj, Aneswh, Tridiv, Subhamoy, Jobi, Prasanna Srinivasa, Chayan, Prashanto, Avrajit, Aritra, Phanindra, Rakesh, Subhankar, Tanmoy, Krishna da, Chandru Da, Partho, Soumya, Satabdwa, Bibhuti, Joice, Ritesh, Samrat, Pavan, Anirban, Raghubar, Manoj Kumar, Deepak, Rubinoor, Anirban Dutta, Candru, Chanappa, Mohan, Manju da, Arun, Ashish Da, Brajesh sirji, Kanhaiya.

I would like to thank Panini, my hostel (Bhaskara) roommate. He has been incredibly understanding and the coolest Telegu guy I have met till now. Special thanks to Mr. Chandrasekhar and Mr. Manjunath, two Bhaskara supervisors.

I must also mention two of my best friends since college days, Surajit and Shivcharan. Also, I thank my favorite teacher from Burdwan university, Prof. Avijit Chakraborty who inspired me to pursue a career in research.

Last but the most important, I would like to express my deepest gratitude to my parents who have always supported and encouraged me to purse a research career in Astrophysics. Special thanks to Didibhai, Jamaibabu and Hapu for their never ending support. At the end, special thanks to a special friend: Priyanka. She always stood beside me in my ups and downs. Thank you Priyanka for all the love, support and the delicious dishes (including 'rosogolla').

Sudip Mandal

Data usage

During different studies, presented in this thesis, I have used telescopic data from various space-based facilities. I duly acknowledge the data usage. I also want to thank the members and associates of these facilities for providing the data.

SDO Data supplied courtesy of the SDO/HMI and SDO/AIA consortia. SDO is the first mission to be launched for NASA's Living With a Star (LWS) Program.

Hinode is a Japanese mission developed and launched by ISAS/JAXA, with NAOJ as domestic partner and NASA and STFC (UK) as international partners. It is operated by these agencies in co-operation with ESA and NSC (Norway).

I would also like to thank KU Leuven, Belgium for providing the computing facility to carry out numerical simulations which are presented in this thesis. Apart from that, I also want to acknowledge the Joint Science Operations Center (JSOC) [¶] and the Hinode Science Data Centre Europe [‖] for providing the download links for the SDO and Hinode data.

[¶] `http://jsoc.stanford.edu/`
[‖] `http://sdc.uio.no/search/form`

Dedicated to

my

family and friends...

Abstract

Corona, the outermost layer of the solar atmosphere, is made up with very hot and taneous plasma material. The density and temperature structuring of this layer, is largely inhomogenous. Temperatures, at certain locations, can reach upto tens of million kelvin (MK). One of the key questions regarding the coronal physics is to identify the ubiquitous source(s) which can sustain this high temperature profile of the coronal plasma. One of the potential candidates in this case, is the family of magnetohydrodynamic (MHD) waves. These waves can propagate from the lower atmosphere to the solar corona and can partially (or fully) dissipate their energy to the surrounding coronal medium. In fact, different physical parameters such as the density, magnetic field and temperature of the host structure can also be inferred by studying the different properties of the propagating MHD wave.

This thesis is focused on examining the different properties of solar magnetohydrodynamic (MHD) waves, specifically the slow magnetoacoustic mode (also known as 'slow wave'), as seen with modern high resolution space based telescopes. Three key aspects: Generation, Propagation and Damping of these waves are studied rigorously in this thesis. A combination of high resolution spectroscopic and imaging data from the 'Extreme-ultraviolet Imaging Spectrometer', onboard Hinode and 'Atmospheric Imaging Assembly' (AIA), onboard Solar Dynamics Observatory (SDO), are used for the unambiguous detection of slow waves. Data from the 'Helioseismic and Magnetic Imager' (HMI) onboard SDO, and the 'X-Ray Telescope' (XRT) onboard Hinode, are also used to study the generation of these waves. Apart from the generation, we also study the damping of these waves while they propagate through large coronal structures, such as active region loops, polar plumes-interplumes etc. A large volume of AIA imaging data have been analyzed to statistically determine the various properties

of the damping mechanisms. To supplement the observed results, we performed 3-D numerical simulations, along with the advanced 'forward modelling' technique and explained the observed wave properties.

Contents

List of Figures

List of Tables

Abbreviations

NASA	**N**ational **A**eronautics and **S**pace **A**dministration
SOHO	**SO**lar and **H**eliospheric **O**bservatory
EIT	**E**xtreme ultraviolet **I**maging **T**elescope
MDI	**M**ichelson **D**oppler **I**mager
TRACE	**T**ransition **R**egion and **C**oronal **E**xplorer
XRT	**X- R**ay **T**elescope
SDO	**S**olar **D**ynamics **O**bservatory
AIA	**A**tmospheric **I**maging **A**ssembly
HMI	**H**elioseismic and **M**agnetic **I**mager
MHD	**M**agneto**H**ydro**D**ynamics
CCD	**C**harge **C**oupled **D**evice
EUV	**E**xtreme **U**ltra**V**iolet
UT	**U**niversal **T**ime
TR	**T**ransition **R**egion
$\mathbf{R}_\odot$	Solar **R**adius

Chapter 1

Introduction

Once upon a time, nearly 4.5 billion years ago, an enormously big and giant cloud of gas gave birth to a star which we now call as the Sun. Over the time, several planets started rotating around the star and constituted a gravitationally bound system, commonly referred as the 'solar system'. Contrary to the earlier belief, it turns out that our Sun is not the only star present in the universe. Infact, our Sun is an ordinary, average sized, second generation, G type star which has already spent half of its lifetime. Despite being a typical star, it's proximity from the earth, makes it an excellent laboratory to test out stellar evolutionary theories and other cosmological experiments.

Another aspect of the modern day solar physics research, is to understand the fundamental physical processes responsible for the violent solar events such as the solar flares, coronal mass ejections (CMEs) and the solar wind surges. In a technologically advanced space era with several commercial and research satellites operating in the space, it has become ever more important than before, to study the effects of these violent solar eruptions on our Earth and also on the space

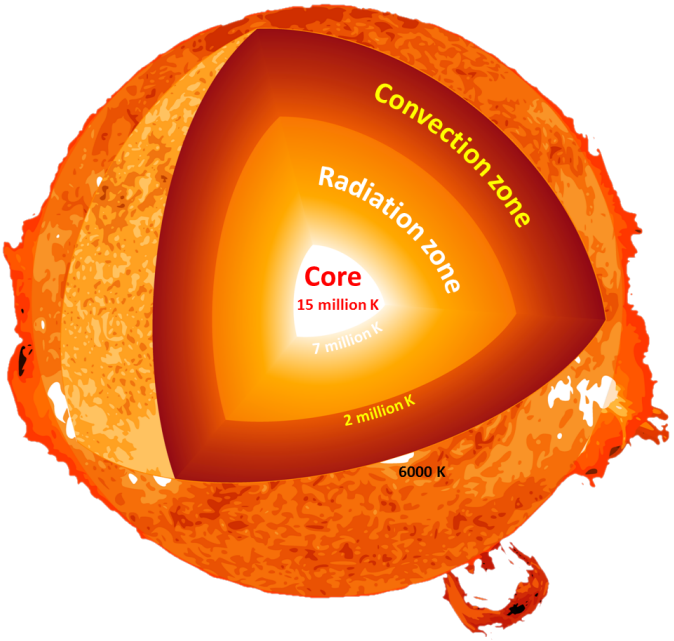

FIGURE 1.1: A cartoon diagram highlighting the inner structures of the Sun. *Image credit:* `https://commons.wikimedia.org/wiki/User:Kelvin13`

between the Sun and Earth, the 'space weather'.

1.1 The Solar Interior

The solar interior can be classified into three different layers (or zones): The 'Core', the 'Radiation zone' and the 'Convection zone'. These divisions are primarily based on the efficient mode of energy transportation in these regions. Figure 1.1 shows a schematic diagram of the solar interior highlighting the average temperatures of these different layers. The innermost region i.e the solar core, is the place where all the energy is being generated. Typical extension of this region is upto a distance about 0.3 $R_\odot$ from the center. Due to extreme pressure and temperature, Hydrogen gets converted into Helium (with small amount of mass loss) via the process of nuclear fusion and as a byproduct, energy gets released in the form of

high energetic γ ray photons. Upon release, these photons starts traveling upwards and enter the 'radiation zone' (extends upto the interface layer at 0.7 $R_{\odot}$). As the name suggests, radiation is the primary mode of energy transportation here. Interestingly, an individual photon bounces so frequently in this region that it takes a very long time (about a million years) to travel through this radiation zone.

As we move away from the Sun center, temperature keeps on dropping considerably, in accordance with the law of thermodynamics. A further away (0.7 $R_{\odot}$and beyond) from the radiation zone, the physical conditions become such that (referred as the Schwarzschild's criterion for instability (Kaniel and Kovetz 1967)), the convection serves as more efficient mechanism of energy transportation hereafter. Due to the convective motions, hot plasma rises upward and upon reaching the surface, releases its energy via radiation into the solar atmosphere. The cool plasma then plunge into the deep interior of the Sun and the cycle repeats. It is worth mentioning that the convection zone is the place where the solar magnetic fields are believed to be generated and stored by means of 'solar dyanmo'. Thus a clear understanding of these motions will help us to better explain the magnetic cycle of the Sun.

1.2 The Solar Atmosphere

Beyond the visible solar surface, there lies the solar atmosphere. As seen in the interior also, temperature and density values change significantly with heights. Infact, such stratification in the atmosphere, dictate the shape and size of the individual features which we see in the solar images as shown in Figure 1.2. Let us highlight the key aspects of these layers as described below.

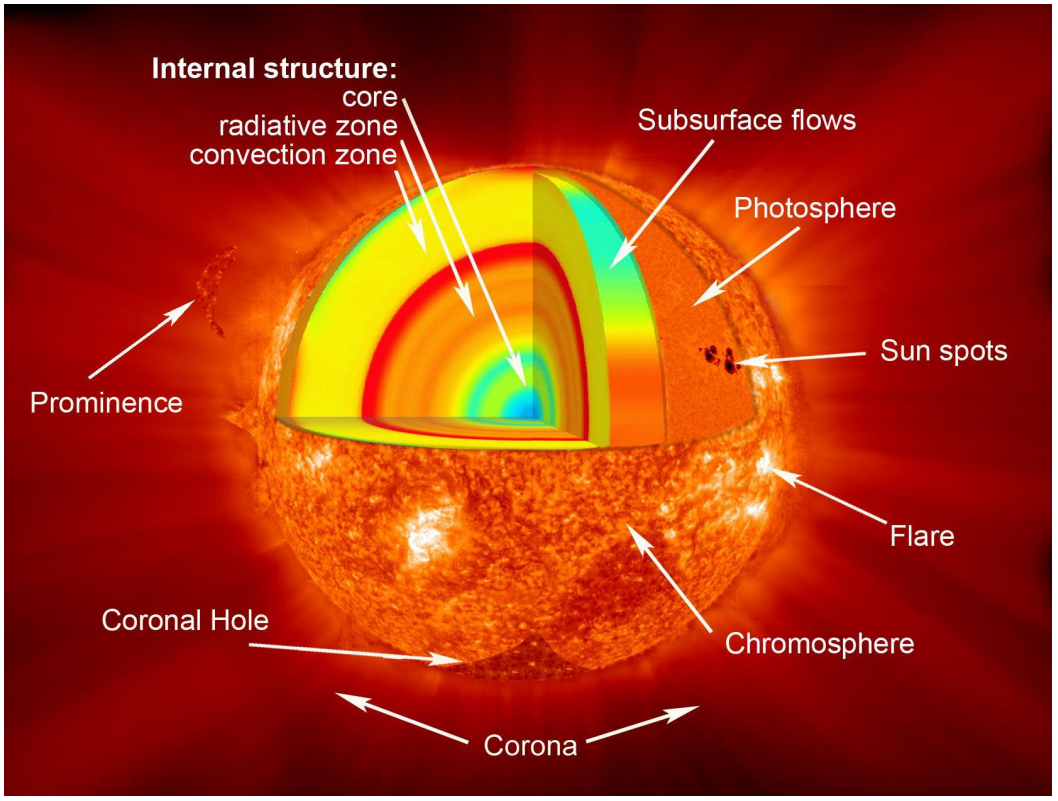

FIGURE 1.2: A schematic figure showing the different layers of the Sun. Commonly observed solar features are also highlighted. *Image credit:* `https://www.nasa.gov/`

1.2.1 Photosphere

The lowermost layer in the atmosphere is known as the 'photosphere'. In other-words, solar photosphere refers to the surface of the Sun when observed in the visible wavelength ($\lambda \approx 5000\mathring{A}$). The temperature of this layer, is 5770K and the total radiation which comes out of this surface, can be successfully explained by modeling it to a black body. The other interesting fact about this layer is that it hosts the strongest magnetic fields in the atmosphere. As discussed earlier, solar magnetic fields are being generated at the base of the convection zone, the so called 'tachocline'. Under suitable conditions, these fields (in the form of flux tubes) rise through the convection zone and break out of the photosphere (Choudhuri 2007). These flux tubes then appear as the Sunspots, the most prominent feature visible on the photosphere. Thus, one can get information about the solar magnetic

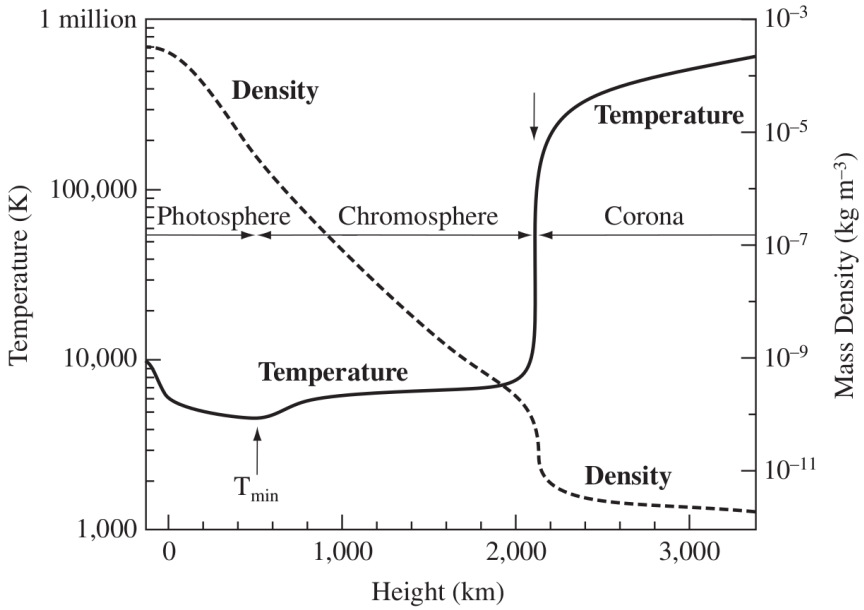

FIGURE 1.3: Schematic view of the temperature and density profiles in the solar atmosphere. Adapted from Priest (2014)

variability by tracing properties of the sunspots (Hathaway 2015). The other visible features on the photospheric images are the granulation patterns and faculae. Granulation is the pattern resulted from the convective motion. The boundaries of the granular cells (also known as 'granular lanes'), are infact the locations of small-scale magnetic fields (Priest 2014). On the otherhand, faculae the bright photospheric features which are mostly visible near the solar limb and they are generally associated with sunspots. Thus, it is now evident that if one needs to investigate the origin and evolution of the solar magnetic fields, then photosphere is the location to look for.

1.2.2 Chromosphere

As we move upwards from photosphere, the temperature initially drops and reaches to a minimum value of 4500 K at a height of 500 Km above the photosphere. This is marked as T_{min} in Figure 1.3. This region is referred as the 'temperature

minimum' region. Solar chromosphere is a ≈2000 Km thick layer whose lower boundary is the temperature minimum region. As see in Figure 1.2, temperature rises slowly at the beginning and rises considerably fast to reach a temperature about ≈15000 K. On the otherhand, density keeps on falling rapidly as we move away from the photosphere. Such rapid decrease in density and sudden increase in temperature, lead to a range of interesting solar features in the chromospheric images. When viewed in Hα line ($\lambda = 6563\mathring{A}$), we notice many different features such as filaments, prominences and spicules. Spicules are the short lived, jet like features, which appear on the solar limb. It is believed that there are two kind of spicules: Type-I, driven by the p-modes and Type-II, driven by reconnection like events (de Pontieu *et al.* 2007). Interestingly, these spicules carry mass from the lower atmosphere and deposit them in the corona. Infact, they are also conjectured to play a leading role in heating up the solar corona (de Pontieu *et al.* 2007). The other feature, called filaments are the extended, dark structures which appear on the solar disc. The off-limb counterpart of the same is referred as prominence. These structures lie along the magnetic neutral lines and are often observed to be related to coronal mass ejections (CMEs) (Zhang and Wang 2001).

About ≈2000Km from the photosphere (near the end of chromospheric layer), there is a only 100 Km wide region where the temperature suddenly rise from 20,000K to a whopping million kelvins (MK). This region is known as the 'transition region'. Understanding of the mass and energy flux passing through this region has been a great interest of study for past couple of decades (Judge 2008).

1.2.3 Corona

Beyond the chromosphere (and transition region), there lies the solar corona. Coronal plasma is very hot (few MK) and extremely low dense (10^{-12} kg m^{-3}). Historically, coronal observations were only restricted to the time of total solar eclipses

when the disc light of the Sun gets completely blocked by the moon. After the advent of artificial coronograph (an optical setup which mimics the event of a total solar eclipse), regular and continuous observations of solar corona became possible. Depending on the mechanisms of the emitted radiation, corona can be further segmented into three classes: K-corona (scattering due to free electrons), F-corona (scattering from dust particles) and E-corona (emission from coronal plasma).

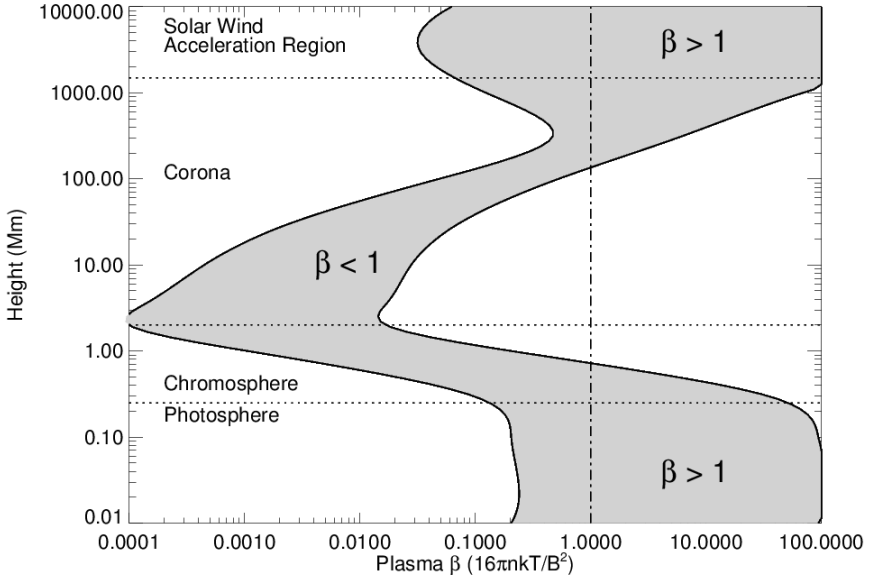

FIGURE 1.4: Variation of plasma-β across different layers of the solar atmosphere. Extracted from Aschwanden (2005)

Solar corona is highly structured and this results in beautiful solar features like coronal loops and arcades. The reason for structuring is the low gas pressure, at these heights, compared to the magnetic pressure. To quantitatively measure the interplay between these two pressure values, a parameter, plasma-β, has been defined as:

$$\beta = \frac{\text{gas pressure}}{\text{magnetic pressure}} \approx \frac{nk\mathrm{T}}{B^2/8\pi} \tag{1.1}$$

The profile of plasma-β with height is shown in Figure 1.4. Thus, a high plasma-β

refers to a 'gas dominated' region (such as the photosphere) whereas the opposite is true for the solar corona ('magnetic field dominated'). Another interesting feature of the solar corona, is the continuous flow of mass with an average speed of 500 Km s^{-1} (Bruno and Carbone 2013). The existence of solar wind can be shown theoretically by considering the hydrostatic equilibrium between the corona and the ambient medium (Parker 1958). Despite the first experimental confirmation in 1959 (by Soviet satellite Luna 1), the more comprehensive knowledge of solar wind emerged from the Ulysses probe in 1990 which orbited the Sun multiple times at high latitudes. In fact, the data from the satellite shows that the solar wind speed follows the sunspot cycle. Though this result is interesting but not a unique one, considering the fact that other coronal events such as flares, CMEs are also seen to have a similar signature of cyclic variations.

1.3 Waves in solar atmosphere

We now know that solar atmosphere is highly stratified in both density and temperature. Interestingly, even after moving further away from the source region, temperature continues to rise and reaches a high value of million kelvins. This forms one of the outstanding problems of solar physics, the 'coronal heating problem'. Many theories have been proposed to solve this issue but none of them could explain it fully (Sakurai 2017). One of the most accepted theory among them, is the heating by MHD waves. Let us briefly describe the different MHD wave modes that are present in the solar atmosphere.

1.3.1 Family of MHD waves

A wave is basically the response of a medium to a perturbing force. As an example, sound waves are generated when the medium (say, the air) is subjected to a pressure perturbation. In similar ways, MHD waves are the responses of a plasma embedded in magnetic fields. For an infinite, homogeneous static plasma, immersed in an uniform magnetic field, we get three wave solutions: the Alfven waves and the slow and fast magnetosonic waves (Poedts 2002). Alfven waves are supported by the magnetic tension whereas the slow and fast magnetosonic waves (or simply slow and fast mode) are sustained by a combination of magnetic and gas pressure (Priest 2014).

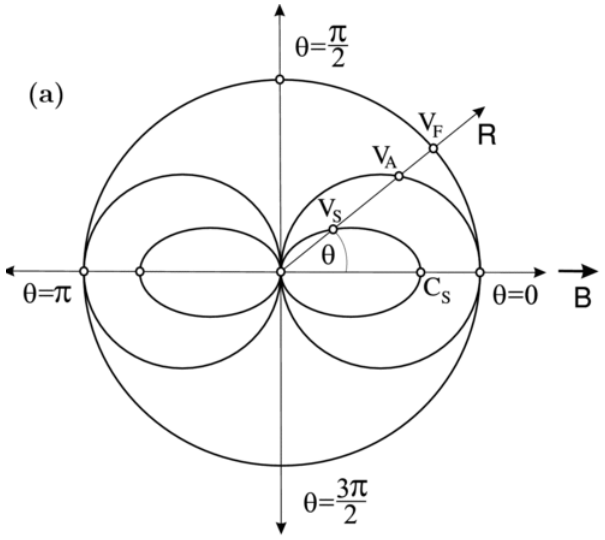

FIGURE 1.5: Phase diagram of different MHD modes. Extracted from Podladchikova *et al.* (2010)

According to the direction of propagation, Alfven waves are transverse in nature (i.e V $\perp$ K) and they are incompressible (i.e no density change) whereas the magnetosonic waves are longitudinal (i.e V $\parallel$ K) and compressible. In order to get a clearer picture, let us follow the phase velocity diagram of these waves as shown in Figure 1.5. As we notice, slow modes and Alfven waves can not propagate across the field whereas the fast mode can propagate isotropically.

An infinite, homogeneous plasma is a simplification of the true solar case, but it provides an insight to the understanding of the wave modes as a first approximation. Considering the finite geometry effects, we obtain consequences like damping, mode degeneracy, mode coupling *etc*. Below in Table 1.1 we summarize the main properties of the three MHD modes.

TABLE 1.1: Main characteristic of the three main MHD modes. Adopted from Kiddie (2014)

Wave	Driving Forces	Speed	Compressible?	Nature	Energy Propagation
Alfven	Magnetic Tension	$v_a \propto \mathrm{B}/\sqrt{\rho}$	No	V$\perp$ k	$\parallel$ to mag. field
Slow Mode	Pressure Forces (out of phase)	$c_s \propto \sqrt{\mathrm{T}}$	Yes	V$\parallel$ k	Cone $\parallel$ to mag. field
Fast Mode	Pressure Forces (in phase)	$c_f = \sqrt{v_a^2 + c_s^2}$	Yes	V$\parallel$ k	$\approx$ isotropic

1.3.2 Observations of waves in solar corona

As discussed earlier, solar atmosphere (specifically the upper chromosphere and the corona) is highly structured and thus, we are able to observe a variety of MHD wave modes in different solar structures. Being a dominant source of UV and EUV raiation, coronal observations got a tremendous boost with the launch of space-based telescopes such as the 'SOlar and Heliospheric Observatory'(SOHO) in 1995. One of the earliest detection of slow mode, was reported by DeForest and Gurman (1998) (also by Ofman *et al.* (1997)) where these authors observed propagating intensity disturbances in polar plumes as shown in Figure 1.6. Speed range of these disturbances (80-140 Km s^{-1}) was the main reason behind identifying them as slow waves. Similar observations were reported subsequently by Berghmans and Clette (1999); Nightingale *et al.* (1999). The other modes such as the global kink mode was first reported by Aschwanden *et al.* (1999b); Nakariakov *et al.* (1999) whereas the (shear) Alfven mode have been first reported in Tomczyk *et al.* (2007). There are lot of follow up observations after these initial reports and those are covered in details in De Moortel (2006); de Moortel (2009); Banerjee *et al.* (2011). The

other aspect of the wave studies, is its capabilities in plasma diagnostics, namely the 'coronal seismology' (De Moortel and Nakariakov 2012). Measuring the wave parameters such as amplitude and period can be further used, along with the theoretical understanding, to determine the temperature, magnetic field of the host plasma (Wang *et al.* 2007; Marsh *et al.* 2009).

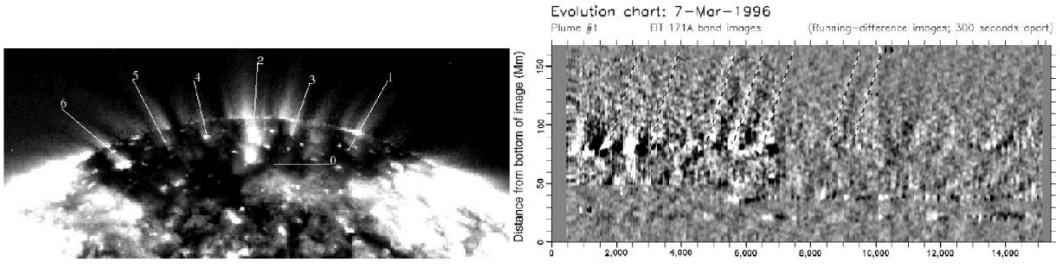

FIGURE 1.6: *Left* : Identified polar plumes on the solar south. Inclined white lines over the structures mark positions of the artificial slits used to create the time-distance maps. *Right* : Generated time-distance maps showing the alternative bright ridge structure. Average speeds, calculated through the slope of these rigdes, is ∼100 Km s^{-1}. Extracted from DeForest and Gurman (1998)

1.4 Synthesized observations: The forward modeling technique

In order to explain an observed phenomena, we sometime perform a numerical simulation and analyze the simulated data in-search of an explanation. Among many other observables we get in the model output, plasma density and temperature are the two important parameters in the context of coronal imaging. Before comparing the model output with telescopic observations, one must translate the density values into photon counts. This step is important as the observed intensity perturbation need not necessarily follow the model density and temperature (De Moortel and Bradshaw 2008). For an optically thin emission, the observed intensity is proportional to the square of density, integrated over the LoS. Thus, to

correctly synthesize the emission, we need three key ingredients: (i) plasma density and temperature values, (ii) ion abundance and, (iii) the instrumental response function. A proper treatment of three of these, will produce a synthesize coronal image which can be directly compared with a real-life observations. There are several forward modeling tools available in the solar physics community: FORWARD (Gibson 2015), GX_SIMULATOR (Nita *et al.* 2015), FoMo (Van Doorsselaere *et al.* 2016). The FoMo tool has been used in this thesis and more details on this particular tool is available at FoMo-Wiki*.

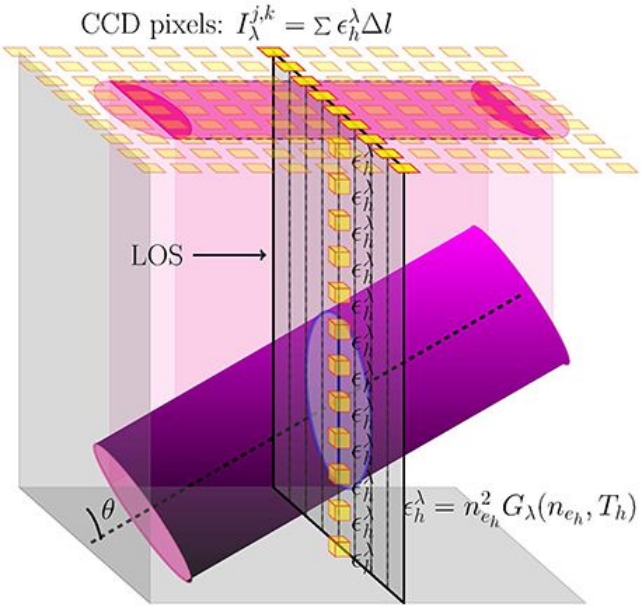

FIGURE 1.7: A cartoon image highlighting the process of LoS integration through the simulation domain. Extracted from Yuan *et al.* (2015)

1.5 Motivation for the Current Studies

Let's focus solely on the slow mode, the subject of interest of this thesis. This is a compressible wave mode *i.e* plasma density changes as the wave passes through the medium. This results in a change in coronal intensities which can be seen to propagate upwards along the structures as shown in Figure 1.6. Thus, such

*https://wiki.esat.kuleuven.be/FoMo/FrontPage

a scenario fits well with the wave description. Some authors also claimed these oscillations to be an effect of p-mode leakage (Bogdan *et al.* 2003). However the scenario changed quickly when simultaneous high resolution imaging and spectroscopic data became available. Tian *et al.* (2011a) found simultaneous oscillations in the spectroscopic line parameters to advocate these propagating disturbances as mass-flows rather than waves. Some other reports (Tian *et al.* 2011a; De Pontieu *et al.* 2009) also supported this upflow scenario whereas explanations of these events in terms of slow wave modes continues to exist (Verwichte *et al.* 2010). In this context we analyzed concurring imaging and spectroscopic data to address this issue and results are presented in Chapter 3.

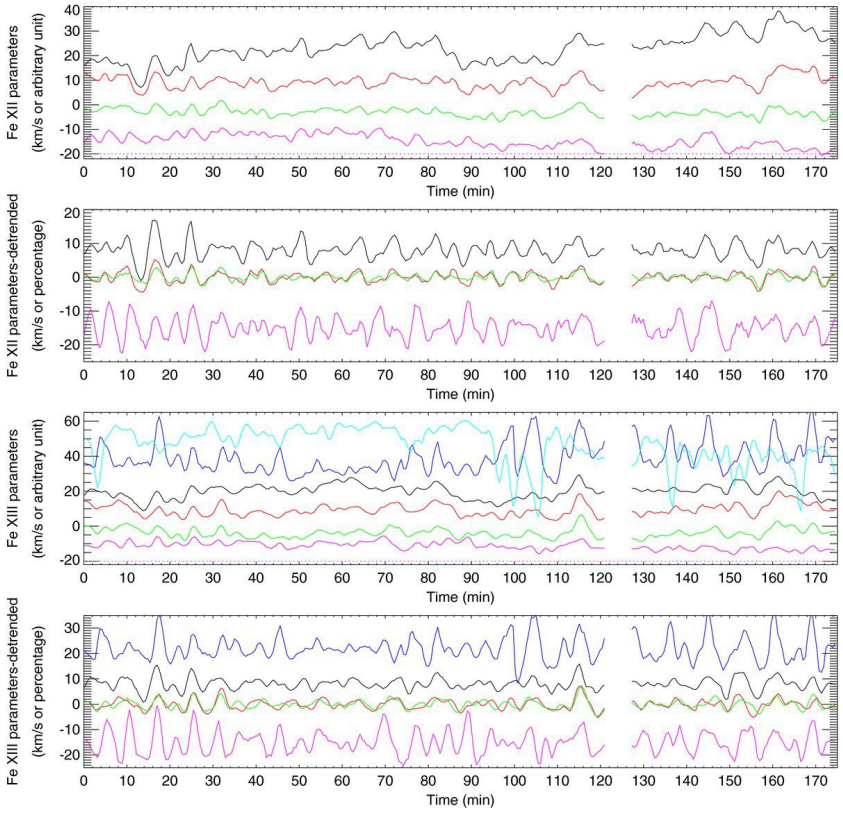

FIGURE 1.8: Time evolution of the line intensity (black), Doppler shift (red), non-thermal width (green), R-B (violet), intensity ratio (blue) between the secondary and primary Gaussian components, and the velocity difference of the two components (cyan) are shown for Fe XII 195.12 $\mathring{A}$ and Fe XIII 202.04 $\mathring{A}$. Extracted from Tian *et al.* (2011a)

Other aspect of the wave study, is to identify the source for these waves. As mentioned previously, p-mode leakage (Bogdan *et al.* 2003) is one of the potential

candidates whereas such oscillations could also be a flare driven phenomena (Wang *et al.* 2005). It has been shown, numerically, by Selwa *et al.* (2005) that flares occurring at the loop footpoints or at a position away from it, can in-principle work as a trigger for the generation of such waves. Infact, a correct identification of the sources can give us insights about the coupling between different layers, chromosphere, transition region and the lower corona. In this context we analyze a set of unique events involving flares and slow waves and the results are presented in Chapter 4.

Propagation of a waves is inevitably associated with loss of energy. This could happen in two ways: mode coupling $i.e$ energy from a specific mode can be transferred into another mode and the other way is to convert the energy into heat via some dissipative mechanisms. In case of slow waves, the damping rate is found to be comparatively rapid (Wang *et al.* 2005). A comparison between numerical simulations and the observations indicate that thermal conduction is primarily responsible for damping these waves (De Moortel and Hood 2003). However, such a description involving thermal conduction as the main damping mechanism, does not always explain all the aspects of the observed damping. One such case is the frequency dependent damping scenario. Investigating a case study involving the on-disc coronal loops, Krishna Prasad *et al.* (2014) found that the observed power law dependence of the wave damping with the wave frequency can not be explained from a theory which considers only thermal conduction as dissipative agent. In this context we perform a 3-D numerical simulation along with the state-of-art forward modeling technique to produce synthetic coronal images and analyze the frequency dependent damping of the produced slow waves. The results from this analysis are presented in Chapter 5.

It is expected that slow wave properties such as the speed will change as the temperature and density structure changes. Interestingly, Krishna Prasad *et al.* (2014) found that the frequency-dependent damping properties also change as one

moves from on-disc coronal loop to the polar plume and interplumes. As shown in Figure 1.9, the slope (of the log-log damping length versus period) becomes negative for the polar structures whereas it is positive for the on-disc loops. It must be noted though from Figure 1.9, there are significance scatters in the plots which suggest a need for a statistical study to confirm the presence of the weak but negative slope values. Using high resolution imaging data from SDO/AIA, we perform a rigorous statistical study on the frequency dependent damping of slow waves in polar plume and interplume regions and the results are presented in Chapter 6.

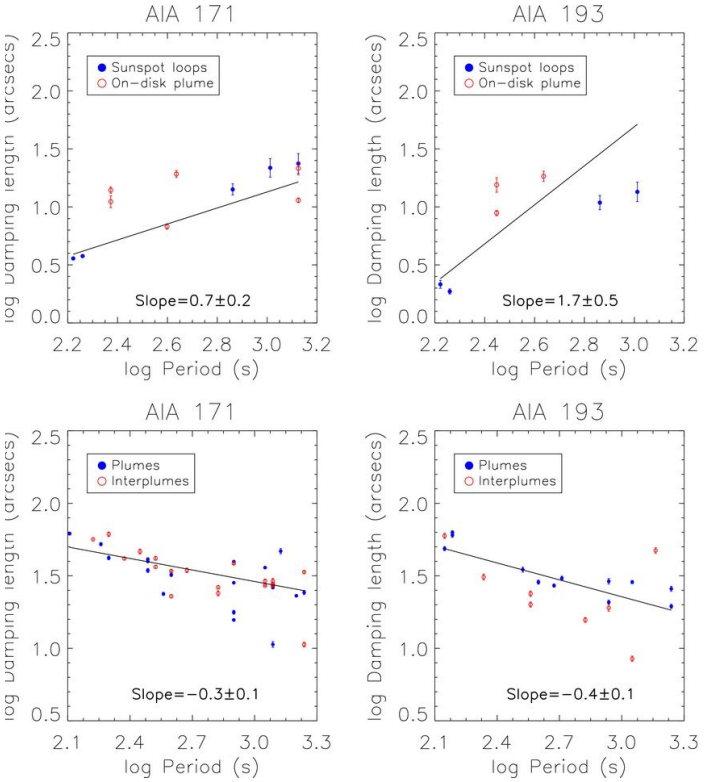

FIGURE 1.9: Variation of damping length with the calculated wave period. Top rows show the relation for the on-disc loop structures whereas the bottom rows show the same but for the polar plumes and interplumes. Extracted from Krishna Prasad *et al.* (2014)

1.6 Outline of the Thesis

This thesis is a combination of observational and numerical studies of slow waves in the corona corresponding to different wavelengths. A summary of each chapter of the thesis is outlined here.

Chapter 1 provides a brief introduction of various solar features. Some of the long standing problems in solar physics and their relevance in the context of this thesis work, are introduced in this chapter.

Chapter 2 outlines a short introduction to the space-based telescopic data that have been used in the thesis. It also highlights the unique capabilities, observational modes of these telescopes along with the data reduction techniques.

In Chapter 3, characterization of propagating disturbances, often observed in active region fan-like coronal loops, is studied. In this chapter, active region AR 11465 is studied using simultaneous imaging and spectroscopic data from the Extreme-ultraviolet Imaging Spectrometer (EIS) on board Hinode and the Atmospheric Imaging Assembly (AIA) on board the Solar Dynamics Observatory (SDO). Spectral properties (namely, the intensity, line width and the Doppler velocity) show coherent enhancements at the 'loop crossing points' (LCPs) which favors the upflow scenario. We also explore the 'Red-Blue' (R-B) analysis technique which quantifies the amount of asymmetry present in the line shape in addition to the velocity measurement of the small scale velocity perturbation which causes this asymmetry. Analyzing the multi-wavelength imaging data from AIA, we show that the propagation speeds of these propagating disturbances vary with the plasma temperature, a typical signature of slow magnetoacoustic waves.

Chapter 4 outlines the investigation on the reflection of propagating slow magnetoacoustic waves in hot coronal loops. Analysis of four such events shows that the wave appears after a micro-flare occurs at one of the loop footpoints with a complex magnetic structure. We estimate the density and the temperature of the loop plasma by performing the 'Differential Emission Measure' (DEM) analysis on the AIA image sequence. The estimated speed of propagation is comparable or lower than the local sound speed suggesting it to be a propagating slow wave. The intensity perturbation amplitudes, in every case, falls very rapidly as the perturbation moves along the loop and eventually vanishes after one or more reflections. To check the consistency of such reflection signatures with the obtained loop parameters, we perform a 2.5D MHD simulation, which uses the parameters obtained from our observation as inputs and performed forward modelling to synthesize AIA images. Analyzing the synthesized images, we obtain the same properties of the observables as for the real observation. We show that a footpoint heating can generate slow wave which then reflects back and forth in the coronal loop before fading out. Our analysis on the simulated data shows that the main agent for this damping is the anisotropic thermal conduction.

In Chapter 5, we explore the theoretical understanding of the frequency dependent damping mechanisms acting on the slow waves propagating through coronal loops. We investigate the relationship of the damping length (L_d) with the frequency of the propagating wave. We present a 3-D coronal loop model with uniform density and temperature and investigate the frequency dependent damping mechanism for the four chosen wave periods. We present a 3-D coronal loop model with uniform density and temperature and investigate the frequency dependent damping mechanism for the four chosen wave periods. This model includes thermal conduction to damp the waves as they propagate through the loop. The numerical model output has been forward modelled to generate synthetic images of AIA channels. The use of forward modelling, which incorporates the atomic emission properties into the

intensity images, allows us to directly compare our results with the real observations. We also explore the contributions of the emission properties on the damping lengths by using density values from the simulation. Theoretical dependence of L_d with wave periods is also examined here.

In Chapter 6, a statistical study on the frequency-dependent damping of slow waves propagating along polar plumes and interplumes in the solar corona, is presented. Analysis of a large sample of extreme ultraviolet (EUV) imaging data with high spatial and temporal resolutions obtained from AIA/SDO suggests an inverse power-law dependence of the damping length on the periodicity of slow waves (i.e., the shorter period oscillations exhibit longer damping lengths), in agreement with the previous case studies. Similar behavior is observed in both plume and interplume regions studied in AIA 171 Å and AIA 193 Å passbands. It is found that the short-period (2–6 min) waves are relatively more abundant than their long period (7–30 min) counterparts in contrast to the general belief that the polar regions are dominated by the longer-period slow waves. The slopes of the power spectra (α, the power-law index) is also explored statistically to better understand the characteristics of turbulence present in the region. The α values and their distributions, in both plume and interplume structures across the two AIA passbands, are also studied to understand the complexity of the underlying turbulence mechanism.

Chapter 7 presents a summary of the entire thesis. Important conclusions drawn from different studies in this thesis, are highlighted here. Possible follow up projects on these studies are also discussed here.

Chapter 2

Instruments

In this thesis, data from several telescopes have been used to study the wave properties in the solar atmosphere. All of these telescopes are operating in the space. Different operational and observational modes and a brief summary of different telescopes, is presented in this chapter.

2.1 Solar Dynamics Observatory (SDO)

Solar Dynamics Observatory (SDO; Pesnell *et al.* 2012) is a space-based, dedicated solar telescope, launched under NASA's Living With a Star (LWS) program. On February 11, 2010, SDO was launched from Cape Canaveral, USA. The main scientific objective of this mission, is to study the various physical processes which have an impact on the solar variability as well as on the space-weather forecasting. One crucial aspect of SDO lies in its capability of observing the Sun with high spatial and temporal resolutions along with a simultaneous multiwavelength coverage. In order to achieve an uninterrupted observations, SDO is placed in

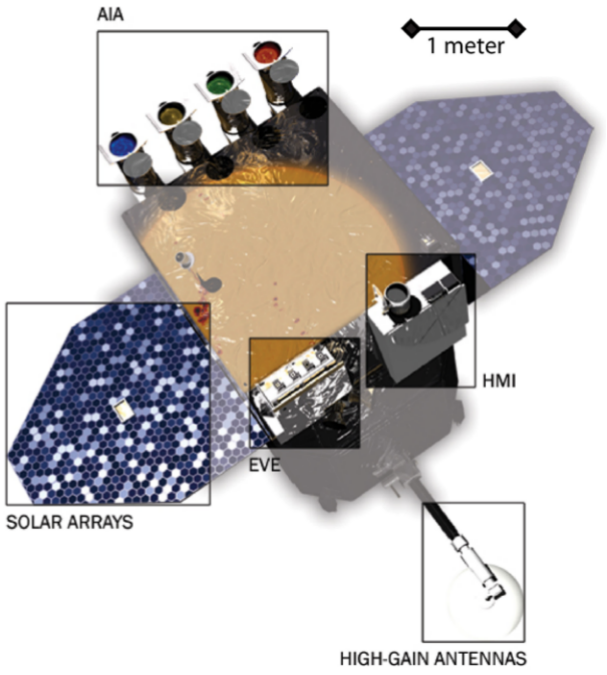

FIGURE 2.1: The SDO spacecraft along with the three onboard instruments. *Image credit:* Pesnell *et al.* (2012)

an inclined (28.5°) geosynchronous orbit. Though there are other ways (such as sunsynchronous orbits) to ensure a continuous observation, but a major restriction come from the volume of data that SDO produces due to its high spatial and temporal resolutions. Onboard storage for such volume of data is not very efficient and thus, with a geosynchronous orbit it transmit the data all day long to its dedicated ground station at White Sands Complex in New Mexico. However, such an inclined orbit also suffers from small interruptions due to two eclipse seasons and three Lunar transits per year. Initially planned for a 5 years of mission lifetime, SDO started its science operations on May 2010 and it is still continuing its regular observations.

SDO hosts there instruments onboard; the Atmospheric Imaging Assembly (AIA) which is built in association with the Lockheed Martin Solar & Astrophysics Laboratory (LMSAL), the Helioseismic and Magnetic Imager (HMI) in association with Stanford University, and the Extreme Ultraviolet Variability Explorer (EVE) in

FIGURE 2.2: AIA. *Image credit:* Pesnell *et al.* (2012)

association with the University of Colorado at Boulder's Laboratory for Atmospheric and Space Physics (LASP). Figure 2.1 shows the SDO spacecraft along with the three onboard instruments. In this thesis, only AIA and HMI data have been used and details of these two instruments are discussed below.

2.1.1 Atmospheric Imaging Assembly (AIA)

Atmospheric Imaging Assembly (AIA; Lemen *et al.* 2012) is an array telescopes. Four identical, dual-channel, normal-incidence telescopes observe the Sun in seven extreme-ultraviolet (EUV) and three UV-visible channels. These observations are near simultaneous which facilities in capturing the dynamics of multiple atmospheric layers at the same time. Each telescope has a primary aperture of 20 cm and captures full disk image of the Sun on a highly efficient back-thinned CCD with 4096×4096 pixels. The effective spatial resolution of these images, is $\approx 0.6''$ per pixel. With all the wavelength channels of AIA, one can effectively cover a wide temperature range of 6000 K to 20 MK (photosphere to corona). In order to

follow the eruptive coronal events such as CMEs, prominence eruptions *etc*, AIA provide a circular field of view (FOV) of diameter 41 arcmin (0.28 $R_{\odot}$ above the limb). Candaces of the EUV and UV and visible channels are 12 sec, 24 sec and 3600 sec respectively. It must be mentioned though, some of the channels do have the facility of reading out small region of interest with a reduced cadence of 2 sec. More details about the observing modes, filter responses, instrument calibration and other technicalities can be found in Boerner *et al.* (2012).

2.1.2 Helioseismic and Magnetic Imager (HMI)

The Helioseismic and Magnetic Imager (HMI; Schou *et al.* 2012) is aimed to study the evolution of photospheric magnetic field at high spatial and temporal resolutions. It also produces Doppler measurement at photospheric heights which can be used to probe the solar interior by using helioseismic techniques. HMI Uses the Fe I 6173 Å absorption line to carry out the measurements. This line is magnetic field sensitive and produces polarised light through the Zeeman effect. By measuring full Stokes parameters, HMI produces full disc Dopplergrams, intensity images along with longitudinal and vector magnetograms. The cadence is 45 sec with a spatial resolution of 0.5″ per pixel. Similar to AIA, HMI also records images on a 4k×4k CCD.

2.2 Hinode

Hinode, formerly known as Solar-B (Kosugi *et al.* 2007), is a space-based solar observatory with a primary goal of understanding the generation and transportation of solar magnetic field and its role in the eruptive solar phenomenon such as solar flares, CMEs. Hinode, originally conceived under a collaborative project

between Japan, the United States and the United Kingdom, has been launched and operated by the Institute of Space and Astronautical Science (ISAS), a division of the Japanese Aerospace Exploration Agency (JAXA). The spacecraft was launched from the Uchinoura Space Center, on September 23, 2006. Ino rder to have uninterrupted observations, it was placed in a circular, Sun-synchronous orbit with an inclination of 97.9°. However such an arrangement poses restrictions on the spacecraft telemetry. Hinode has a limited contact time with its two ground stations: Uchinoura space center station and the Norwegian high-latitude at Svalbard. The data which could not be transmitted to the ground, gets stored in an onboard recorder of 8 Gbits storage. Further details on spacecraft operation and observing modes can be found in Kosugi *et al.* (2007).

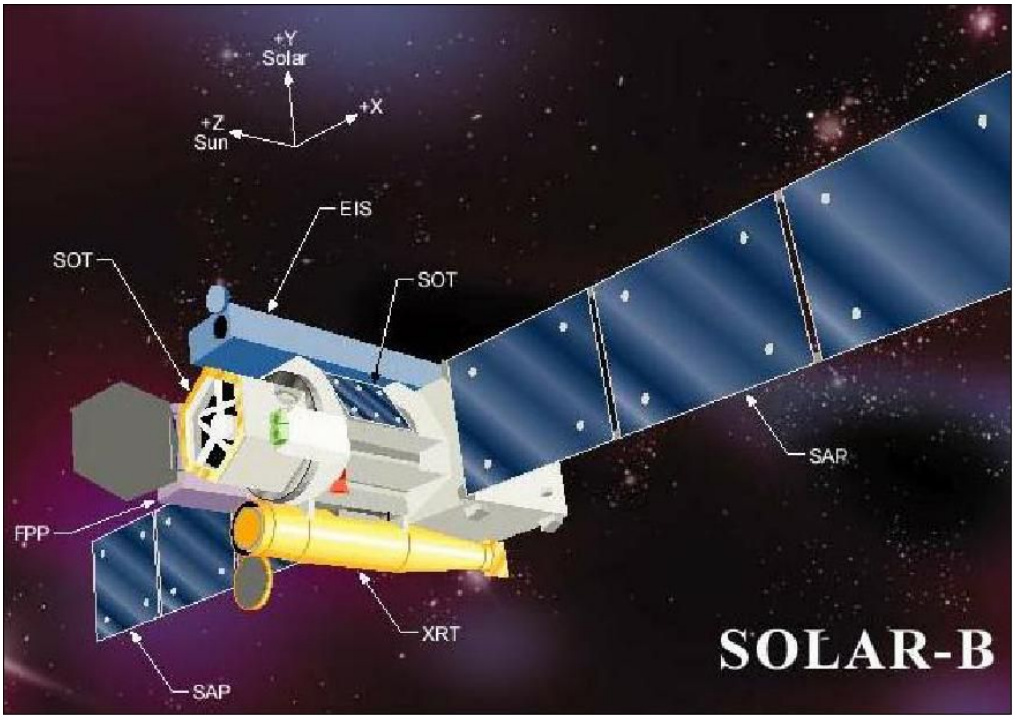

FIGURE 2.3: Artists impression of Hinode spacecraft. Three onboard instruments (SOT, EIS, XRT) are also highlighted. *Image credit:* JAXA

There are three instruments onboard Hinode: the Solar Optical Telescope (SOT), the Extreme ultraviolet Imaging Spectrometer (EIS) and the X-Ray Telescope (XRT). Combining these three instruments, Hinode has a wavelength coverage

from optical to X-ray. Following sections provide further details about the EIS and XRT instruments, of which data have been used in this thesis.

2.2.1 Extreme ultraviolet Imaging Spectrometer (EIS)

The Extreme ultraviolet Imaging Spectrometer (EIS; Culhane *et al.* 2007) is aimed to diagnose the heating mechanisms in active and quite regions of the Sun through measuring the plasma velocities and line broadening. It operates in the wavelength range of 170–210 Å and 250–290 Å which covers the transition region and the corona. There are two prime observing modes of EIS: 'sit and stare' mode where the slit stays fixed on a spatial location and the 'raster mode' where the slit scans a particular region over a certain observing time. The available spectral slits are of $1''$ and $2''$ whereas two slots of $40''$ and $266''$ are used for spectral imaging. One of the advantages of EIS is that it can simultaneously observe 25 spectral lines covering a temperature range of log T=4.7–7.3 K. Further details on the instrument design and optical layout can be found in Culhane *et al.* (2007).

2.2.2 X-Ray Telescope (XRT)

The X-Ray Telescope (XRT; Golub *et al.* 2007) captures images of the highest temperature coronal plasma. It covers a temperature range of $6.1 < \log T\ (in\ K) < 7.5$. In order to maximize the observation efficiency, XRT uses two sets of filters: 'pre-filters' which blocks the visible part of the light and allows only X-rays to pass through and the 'analysis filters' which act as the bandpass filters for plasma diagnostics. There are total nine 'analysis filters': Al-mesh, Al-poly, C-poly, Ti-poly, Be-thin, Al-med, Be-med, Al-thick, Be-thick. These filters are of different thicknesses and generally the thick filters are used for flare studies whereas the

thin filters are preferred for structures (or regions) with fainter emissions. XRT is equipped to capture the Sun in different modes. It has an effective spatial resolution of 1.03″ when operating in small region of interest whereas the value changes to 4.1″ when it operates in full-disc capturing mode. More details on the XRT optical design, mirror efficiency and the filter performances can be read in (Golub *et al.* 2007).

The following table provides an overview of the different datasets which have been used in the thesis.

TABLE 2.1: List of the general properties of the instruments of which the data have been used in this thesis.

Spacecraft	Instrument	Abbrev.	Observation Type	Full Disc?
Solar Dynamics Observatory	Atmospheric Imaging Assembly	AIA	Imaging	Yes
	Heliospheric and Magnetic Imager	HMI	Magnetogram	Yes
Hinode	Extreme ultraviolet Imaging Spectrometer	EIS	Spectroscopic	No
	X-Ray Telescope	XRT	Imaging	Yes †

†small field of view observation is also available

2.3 Data reduction procedures

Data captured on the CCDs are not immediately ready for scientific usage. One needs to follow certain calibration steps (sometimes instrument specific also) to improve the data quality. To indicate the level of calibration, in general, different 'level numbers' are assigned to the data. Let us first review some of the standard calibration steps which are being applied onto the data before moving into the instrument specific ones.

After reading the initial CCD data which is referred as Level 0, two common reduction steps are performed: the dark corrections (including bias) and flat fielding. The first step accounts for the digital offsets and the thermal currents whereas the flat-fielding takes care of the pixel to pixel variations of the CCD. The dataset

is then checked and diagnosed for bad pixels, cosmic ray hits and saturated pixels. For the AIA and XRT full disc data, the images are also aligned such that the solar north is always at the top of the array. On the other hand, EIS data go through further calibrations for flagging of hot pixels, warm pixels and dusty pixels. These calibrations generate Level 1 datasets. For AIA, these steps are already implemented in the data reduction pipeline by Joint SDO Operations Centre (JSOC) science-data processing (SDP) facility before they are available to the public. However, further calibrations, such as equivalent plate scale in all the channels, correcting for different roll angles *etc*, are required on the AIA data after the download and can be achieved by using a Solar SoftWare (SSW) routine aia_prep.pro. After the completion, Level 1.5 data gets generated and this level can now be used for scientific analysis. A similar routine, xrt_prep.pro is used for the XRT data to generate the Level 1 XRT data.

In case of EIS, to generate Level 1 data, the user needs to apply eis_prep.pro which takes care of all the above corrections. It also generates an error file which contains 1-σ errors of the calibrated intensities. At this point, EIS slot datasets are ready for scientific analysis whereas two major corrections are still needed for the spectroscopic data from the slit(s). One of these two effects come from the fact that the EIS slits are tilted with respect to the CCD axes. The other effect is related to the motion of the spacecraft around the Earth. Both of these effects cause a shift of the line center. Another SSW routine eis_auto_fit.pro corrects these issues and computes the line parameters (intensity, Doppler velocity, and the line width) by fitting a single Gaussian to the observed line profile. For further details on the above calibration processes can be found at EIS Wiki page*.

*http://msslxr.mssl.ucl.ac.uk:8080/eiswiki/

Chapter 3

Nature of the propagating disturbances as seen in coronal fan-like loops[†]

3.1 Introduction

Coronal loops are made up of hot plasma controlled by magnetic fields. According to magnetohydrodynamic (MHD) wave theory these loops can support different MHD wave modes (Roberts 2000; Banerjee *et al.* 2007). With the recent high resolution observations, quasi-periodic propagating disturbances (PDs) are commonly observed in the solar atmosphere (DeForest and Gurman 1998; Gupta *et al.* 2012; Krishna Prasad *et al.* 2011, 2012a). The apparent propagation speed of these PDs ranges from 50 to 200 km s^{-1} which is close to the sound speed in the corona

[†]Results of this work are published in Mandal *et al.* (2015).

All the animations that are referred to in this chapter are available at `https://doi.org/10.1088/1674-4527/15/11/006`

(Kiddie *et al.* 2012). This led to their interpretation as slow magneto-acoustic waves. Time series analysis shows that these quasi-periodic PDs in coronal loops have periods ranging from 3 to 30 min (Banerjee *et al.* 2001; Wang *et al.* 2009a,b; Gupta *et al.* 2009; Krishna Prasad *et al.* 2012b). Spectroscopic observations reveal that these longitudinal disturbances often show a correlation between the line intensity and Doppler shift (Kitagawa *et al.* 2010). It was suggested that these oscillations are due to the leakage of the p-mode oscillations which are modified in the presence of magnetic field and travel to the higher atmosphere along the loops (Bogdan *et al.* 2003; De Pontieu *et al.* 2004; Srivastava and Dwivedi 2010). The signatures of damping in these PDs have also been reported (De Moortel and Hood 2003; Wang *et al.* 2002; Krishna Prasad *et al.* 2014).

Recent spectroscopic observations indicate that these PDs not only show periodic oscillations in intensity and Doppler velocity but sometimes also in line width (Tian *et al.* 2011a). Although in the past, oscillations observed in the loops were generally interpreted as signatures of various modes of MHD waves, Tian *et al.* (2011a) suggested that the observed quasi-periodic oscillations are not necessarily due to the slow magnetoacoustic waves. They reported that the footpoint regions of the loops show a coherent behaviour in all the four line parameters (line intensity, Doppler shift, line width and profile asymmetry) based on which they proposed that PDs can also be due to high-speed quasi-periodic upflows. They found that there are some faint enhancements in the blue-ward wing of the line in addition to the bright core of the line which indicates coronal upflows. A strong upflow with a velocity of 50 to 150 km s^{-1} have been reported by De Pontieu *et al.* (2011). To distinguish the upflow emission component from the bright core, De Pontieu *et al.* (2009) and Tian *et al.* (2011b) have used the asymmetry measurement in emission line profiles. To quantify the asymmetry, they subtracted red wing from blue wing (B-R) of the spectral lines. They show that the dominant primary emission component is superimposed with a faint secondary component

which causes asymmetry in the line profiles. These quasi-periodic upflows create a profound asymmetry in the blue wing of the spectral line. The secondary component also enhances the line intensity and line width and cause a change in Doppler shift periodically. Tian *et al.* (2012) found that footpoints of active region loops show oscillations with period around 10 min. They also found that all the line parameters (line intensity, Doppler shift, line width, and profile asymmetry) vary coherently and show apparent blueshifts and blue-ward asymmetry in the line profiles. They proposed that these oscillations are due to quasi-periodic upflows which supply hot plasma and energy to the corona. Quasi-periodic upflows have also been reported in coronal loops using spectroscopic observations by many authors (Ugarte-Urra and Warren 2011; Martínez-Sykora *et al.* 2011; Brooks and Warren 2012; Sechler *et al.* 2012; Tripathi and Klimchuk 2013). Tripathi *et al.* (2012) have pointed out that upflows are strong at the loop footpoints and their strength decreases with height.

These recent observations challenge the well established explanation of PDs as slow magnetoacoustic waves. But, Verwichte *et al.* (2010) have shown that due to the in-phase behaviour of velocity and density perturbations, upward propagating slow waves generally have the tendency to enhance the blue wing of the emission line. Wang *et al.* (2012) have used a different method (which includes photon noise) to measure the velocity of secondary emission component due to flows and showed that it was overestimated due to the saturation effects. They argued that the flow interpretation of the observed PDs is less favorable compared to the wave interpretation. Nishizuka and Hara (2011) found blueward asymmetry in the line profiles at the base of an active region but with increasing height along the loop, line profiles become symmetric. At higher locations intensity disturbances are in phase with the velocity which favours upward propagating slow-mode waves scenario.

It is believed now that both the waves and flows might actually coexist close

to the foot points of the loops and imaging observations alone are insufficient to distinguish them. One needs to perform a detailed analysis of all the line parameters using spectroscopic data which we attempt to do in this study.

3.2 Observation and data preparation

The dataset used in the present study is obtained from the observations of an active region AR11465 on 2012 April 26, by the EUV imaging spectrometer (EIS) onboard HINODE and the Atmospheric Imaging Assembly (AIA), onboard Solar Dynamic Observatory (SDO).

3.2.1 EIS observation

The EIS observation was taken in two modes. The first one is a raster scan obtained with the 2″ slit from 13:02 UT to 13:33 UT covering the active region via 30 raster steps. The X and Y pixel scales are 2″ and 1″ respectively. The Field Of View (FOV) covered by the raster is $60'' \times 512''$, shown as white box in Figure 3.1 (I). The second mode is a sit-and-stare observation obtained with the 2″ slit placed at two positions (as shown in white dashed line in Fig.3.1 (I)) between 13.35 UT and 14.35 UT. The first sit and stare observation (slit-1) is obtained from 13:35 UT to 14:05 UT and the second one (slit-2) is from 14:05 UT to 14:35 UT. The cadence of these observations is 47 s and the total duration of each set is 31 min. We performed the standard data pre-processing for all the EIS data with *eis_prep*.pro.

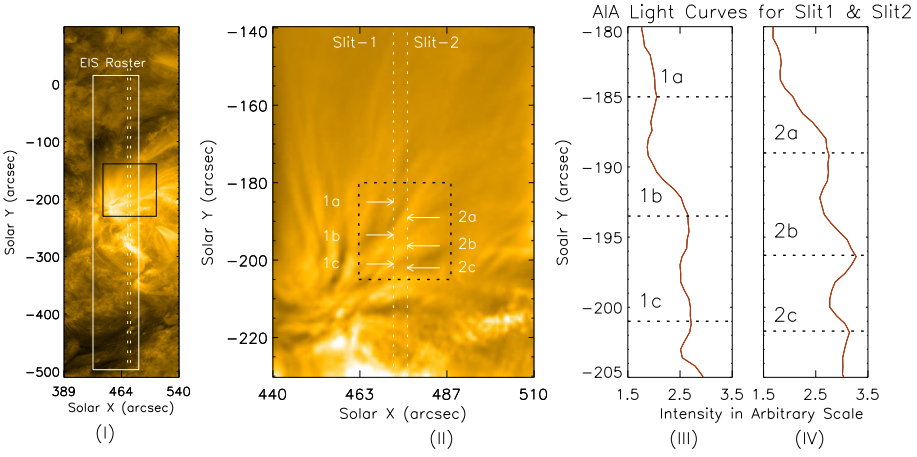

FIGURE 3.1: (I) AIA 171 Å image displaying fan-like loop structures at an active region boundary. The white rectangular box marks the region covered by the EIS raster. Two vertical dashed lines represent the positions of two EIS slits used for sit-and-stare observations. The small rectangular black box shows our Region Of Interest (ROI). (II) Zoomed-in view of the ROI showing the two slit positions and 6 analysis locations (1a-1c and 2a-2c). (III) & (IV) Average 171 Å AIA intensity profiles along slits 1 & 2 respectively, showing the identification of loop crossing points (LCPs).

3.2.2 AIA observation

We have used the corresponding SDO/AIA data in the 171 Å and 193 Å channels taken from 13:00 UT to 15:00 UT which covers the EIS observation period. The cadence is 12 s. The level 1.0 data have been reduced to level 1.5 using the *aia_prep.pro* which makes the necessary instrumental corrections. The final pixel scale is $\approx 0.6''$ in both X and Y directions. Inorder to use AIA and EIS data together, one must need to align the two datasets first. Data from the AIA 193 Å channel is used for coalignment between the two instruments. The coaligment has been achieved by cross-correlating the EIS 195 Å raster scan with the corresponding AIA 193 Å image. The final positions of the EIS sit-and-stare slits after correcting for the obtained offsets, are shown as vertical dashed lines in Figure 3.1.

Figure 3.1 clearly shows the EIS slits positioned over the fan-like loop structures.

We identify 6 locations, three (1a-1c) over the first slit and three (2a-2c) over the second slit, where the fan loops are found to cross the EIS slits. These locations, referred as Loop Crossing Points (LCPs), are identified from the peaks in time averaged AIA 171 Å intensity profiles along the respective slits (see panels III and IV of Figure 3.1).

3.3 Data analysis and Results

3.3.1 Spectral Analysis

Data from Fe XII 195.12 Å and Fe XIII 202.04 Å lines are used in the present analysis. The Fe XII 195.12 Å line is self-blended with another Fe XII line at 195.18 Å (Young *et al.* 2009). So we have used a double Gaussian fitting for this line to derive all the spectral line parameters *i.e.* intensity, Doppler velocity, and line width using *eis_auto_fit.pro*. While fitting the line profile with two Gaussians, the separation between the lines was fixed at 0.06 Å and the line widths were restricted to be same. Equal widths are expected since both the lines are from the same ion. The spectral parameters for the Fe XIII 202.04 Å line are derived from a single Gaussian fitting. We also estimated the "Red minus Blue" (R-B) asymmetry in the line profiles by following a method similar to that described in Tian *et al.* (2011b). The exact procedure for obtaining the R-B asymmetry involves the following steps: (i) First we use spline interpolation to increase the line profile sampling by a factor of 10 times more than the original. (ii) Then we select the peak intensity position as the line centroid (following RB_p method in the reference). (iii) Two narrow spectral windows are then selected at a chosen distance on both sides of the centroid *i.e.* at the red and at the blue wing. We have selected these spectral windows to be at wavelength positions corresponding to 60-125 km s^{-1}. (iv) The total intensity in this window at the blue wing is then

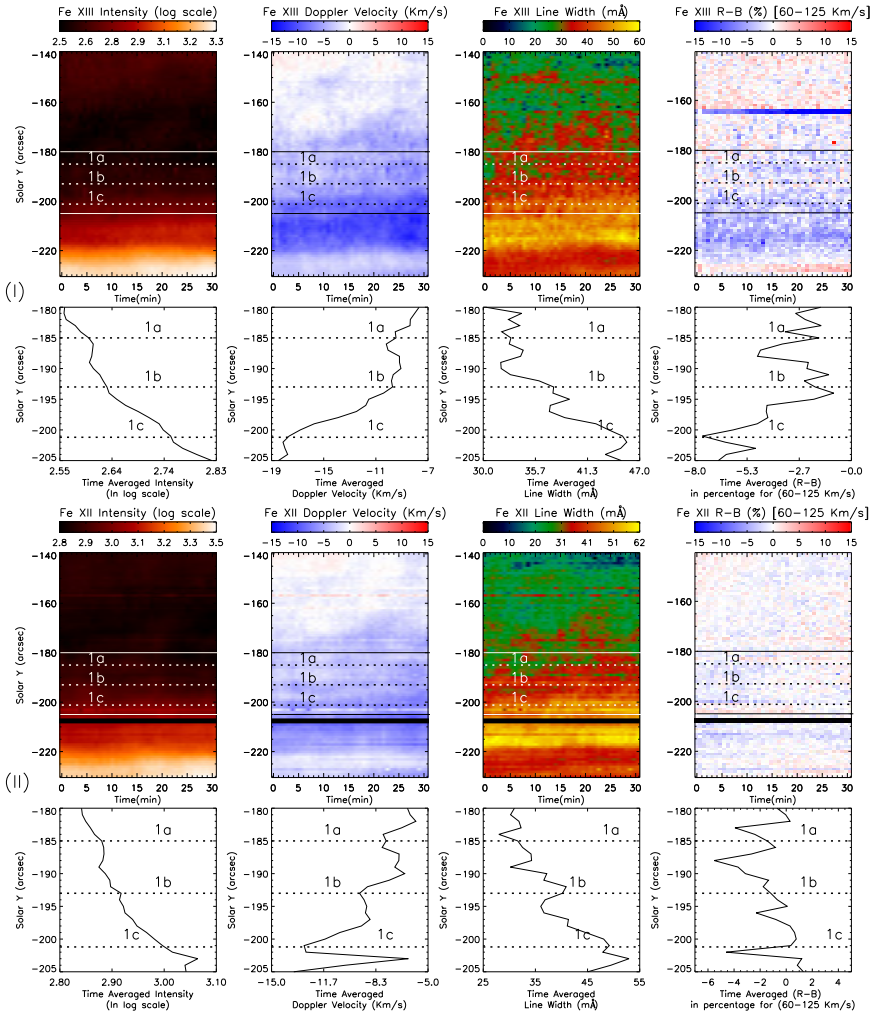

FIGURE 3.2: (I) Top panels (from left to right) show the temporal evolution of the peak intensity, Doppler shift, line width, and R-B asymmetry, in the Fe XIII 202.04 Å line for slit-1. Bottom panels show the time averaged values in these parameters for the region bounded by the solid lines marked in top panels. LCPs corresponding to slit-1 are marked in all these figures. (II) Same as the above for the Fe XII 195.12 Å line. The black horizontal band near $Y \approx -207''$ correspond to missing data due to bad pixels.

subtracted from that at the red wing to obtain the R-B value. For the 195.12 Å line, the corresponding contribution from the 195.18 Å line in the red wing is also subtracted. The obtained R-B values are normalised with the peak intensity to give (%) asymmetry in the line profile.

The constructed time-distance maps of line intensity, Doppler shift, line width, and R-B asymmetry, corresponding to the slit-1, for the EIS Fe XII 195.12 Å and Fe XIII

202.04 Å lines are shown in Figure 3.2. The bottom panels, for each spectral line, in this figure show the time-averaged variation in these parameters for the region bounded by the solid lines in the top panels. The LCPs corresponding to slit-1 are also marked in this figure. An interesting feature to note is the corresponding increase in Doppler shift and line width at the LCPs (Tian *et al.* (2011b) found similar results). The R-B asymmetries for both the lines show enhancements in blue wings leading to a negative R-B value.

3.3.1.1 Coherence in Line Parameters

The temporal evolution of the EIS 195 Å and 202.04 Å lines at LCPs indicate oscillations in all the line parameters. We show the variation in intensity, Doppler shift, and line width, for all the LCPs (for 195.12 Å line) in Figure 3.3. All these light curves are trend subtracted by a 15 point running average to filter out long period variations. To explore the possible coherency in oscillations and to quantify it, we computed cross-correlation coefficients between different line parameters for both the lines and listed them in Table 3.1. Carefully looking at the table, we notice that the correlation values between intensity and velocity, are relatively high and persistent in all the LCPs for both the lines.

3.3.1.2 Periodicity of Oscillations

To measure the periodicity in the observed oscillations, we performed wavelet analysis on all the line parameters at the LCPs. Before performing the analysis, a 3-point running average has been considered to improve the signal-to-noise.

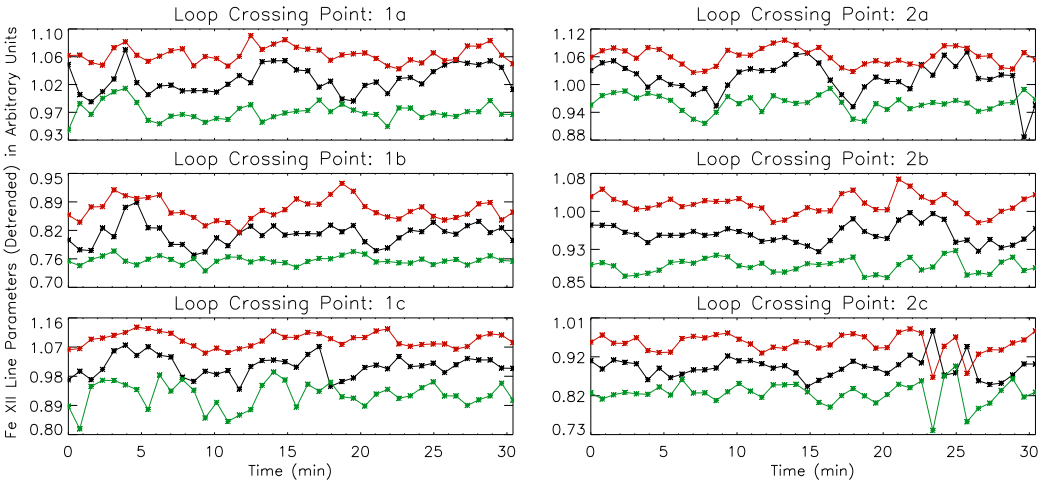

FIGURE 3.3: Variation in intensity, Doppler shift, and width of the Fe XII 195 Å line for all the LCPs is shown in red, black, and green curves respectively, in each panel.

TABLE 3.1: Cross-correlation Coefficient values

Position	*Intensity−Doppl.Velocity*		*Doppl.Velocity−LineWidth*		*LineWidth−Intensity*	
	195.12	202.04	195.12	202.04	195.12	202.04
1a	0.51	0.62	0.18	0.64	0.36	0.55
1b	0.43	0.64	0.05	0.63	0.46	0.50
1c	0.55	0.15	0.24	0.52	0.56	0.24
2a	0.56	0.64	0.48	0.56	0.70	0.55
2b	0.53	0.57	0.20	0.30	0.60	0.68
2c	0.76	0.76	0.24	0.56	0.47	0.62

The sample wavelet plots corresponding to the LCP 1b are shown in Figure 3.4. Wavelet results for the corresponding AIA intensity are also shown in this figure (bottom-right plot). In all these plots, the upper panel shows the trend-subtracted light curve, the bottom-left panel shows the wavelet power spectrum and the bottom-right panel shows the global wavelet power which is nothing but the wavelet power at each frequency scale averaged over time. The contours in

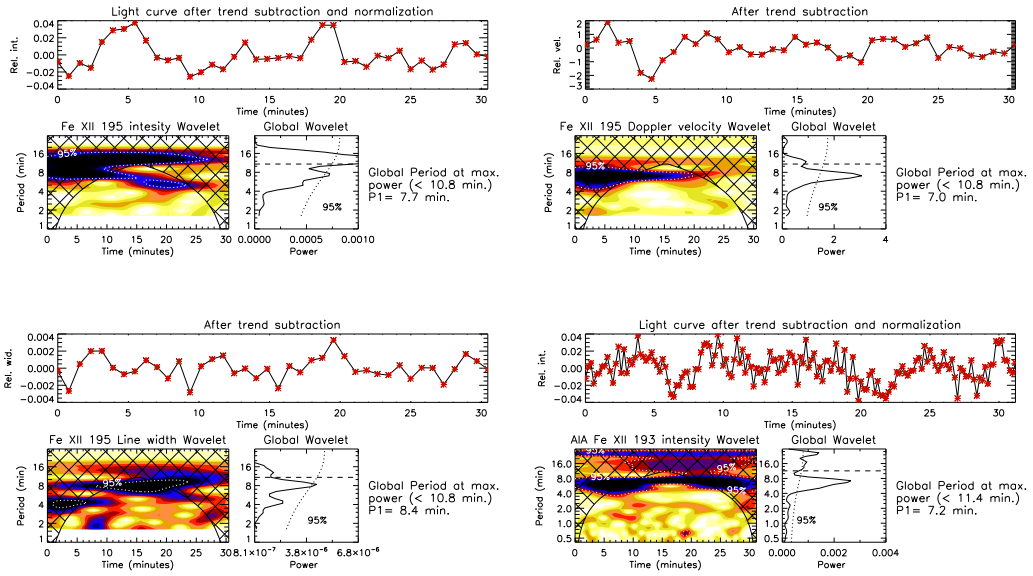

FIGURE 3.4: Results of wavelet analysis for the variations in intensity (top left), Doppler velocity (top right), and width (bottom left) of EIS Fe XII 195 Å line and AIA 193 Å intensity (bottom right), corresponding to the LCP 1b. Top panel of each plot show the trend-subtracted light curve. Bottom-left panel shows the wavelet phase plot and the bottom-right panel shows the global power plot. The contours in the wavelet phase plot and the dotted curve in the global wavelet plot represent 95% significance level for white noise (Torrence and Compo 1998). The periods with the maximum significant power are listed adjacent to the global wavelet plot.

the wavelet plot and the dotted line in the global wavelet plot represent the 95% significance level calculated for white noise (Torrence and Compo 1998). The cross-hatched region in the wavelet plot indicates the cone of influence (COI) where edge effects come into play. In the global wavelet plot, the horizontal dashed line marks the maximum measurable period (due to COI), which is ≈11 min for our 31 min observation. The periods with the maximum significant power are listed adjacent to the global wavelet plot. These plots suggest a periodicity of 7.7 min in EIS 195.12 Å intensity, 7.0 min in Doppler velocity, 8.4 min in line width, and 7.2 min in AIA 193 Å intensity at LCP 1b. The results for other LCPs (in other EIS lines and AIA channels) are listed in Table 3.2 which are in the range of 3 to 10 min.

TABLE 3.2: Periodicities obtained from the wavelet analysis (in min)

Position	*EIS*		*EIS*		*EIS*		*AIA*	
	Intensity		*DopplerVelocity*		*LineWidth*		*Intensity*	
	195.12	202.04	195.12	202.04	195.12	202.04	171	193
1a	7.7	5.0	7.7	4.6	5.0	5.4	7.9	7.2
1b	7.7	7.0	7.0	7.7	8.4	7.7	7.2	7.2
1c	8.4	8.4	5.9	4.2	5.4	5.4	7.9	6.1
2a	5.9	7.0	7.7	7.0	5.9	6.5	6.1	6.6
2b	7.0	9.1	4.6	9.1	5.0	9.0	6.1	6.1
2c	3.8	6.5	7.0	5.9	3.5	6.5	5.1	9.4

3.3.2 Image Analysis

3.3.2.1 Powermaps

We have created a movie (Movie 1, available online) of the ROI from the AIA 171 Å image sequence. One can clearly see the presence of PDs travelling outward in the movie. However, it requires further analysis to figure out their relation with the oscillations observed at LCPs.

Using AIA images, we constructed powermaps of the selected region in three period bands, 2 – 4 min, 4 – 6 min, and 6 – 10 min (see Figure 3.5). To create these maps, we perform wavelet analysis on the light curve at each pixel within the selected region and obtain the power at all possible periods. Then the power in a selected period window is averaged to make a powermap corresponding to that period range. Loop-like structures are clearly visible in the powermaps and in the 6 – 10 min period range which is observed at LCPs, these structures are visible up to the EIS slit positions. This might indicate that the PDs travelling along the loops, and the oscillations observed at the LCPs are related.

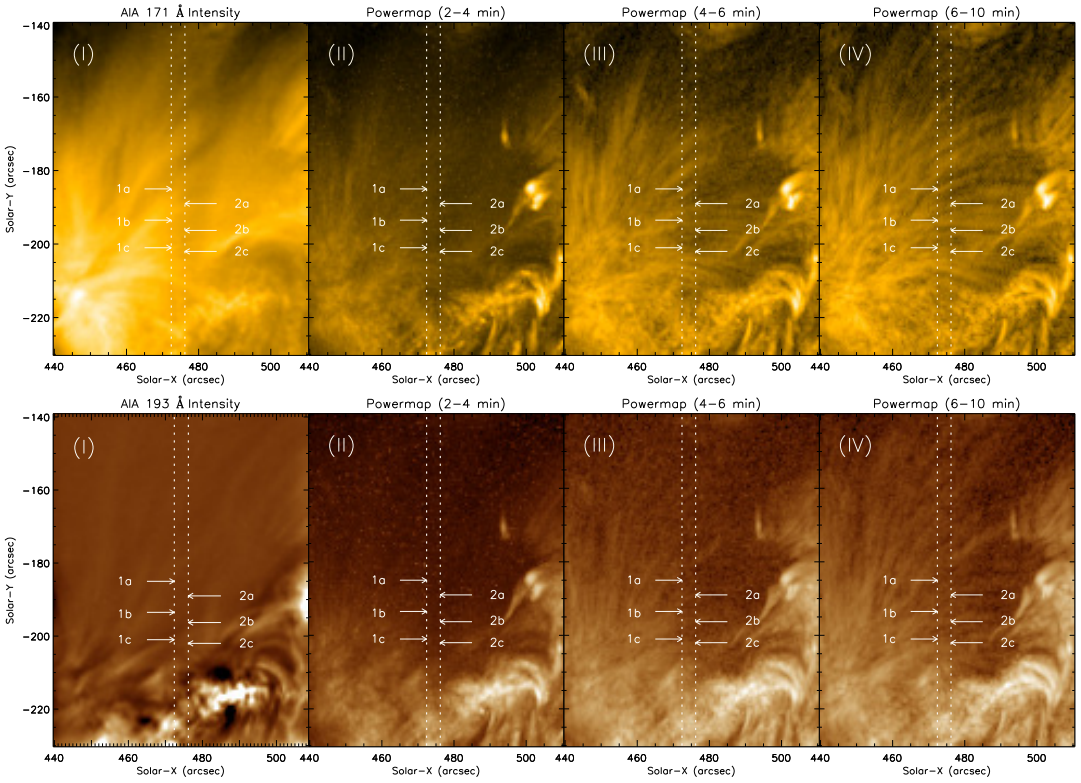

FIGURE 3.5: AIA 171 Å (top panel) and 193 Å (bottom panel) intensity images for the ROI shown in Figure 3.1 and the corresponding powermaps in three period bands as indicated. The locations of the EIS slits and selected LCPs are also marked. The loops which are faintly visible in the intensity image of the 193 Å channel are seen clearly in the respective powermaps.

3.3.2.2 Propagation Speeds

Propagation speed is one of the important parameters to understand the nature of PDs. To examine the typical speeds in this region we performed time-distance analysis. Two fan loops, crossing the EIS slits, were selected and artificial slices were made along those loops. Time-distance maps were then constructed for these slices using the AIA image sequence. The locations of the two slices and the corresponding time-distance maps, for the two AIA channels, are shown in Figure 3.6. The time-distance maps were enhanced by subtracting longer trends at each spatial position. Bright ridges of varying intensity and inclination are visible in these maps. These ridges represent the observed PDs and their inclination gives

the apparent propagation speed. The positions of the local maxima were identified along each ridge and fitted with a linear function to calculate the propagation speed. The obtained speeds for the individual ridges are marked in the figure. The values range from 17 – 60 km s^{-1} (with errors less than 7 km s^{-1}) for the 171 Å channel and 37 – 87 km s^{-1} (with errors less than 11 km s^{-1}) for 193 Å channel. The speed ratios, calculated from the common ridges appearing in the two AIA channels, range from 1.1 to 2.0. This shows the speeds of the PDs are temperature dependent. Note that these measured speeds are the apparent speeds in the plane of sky. Hence, the real speeds can be much higher.

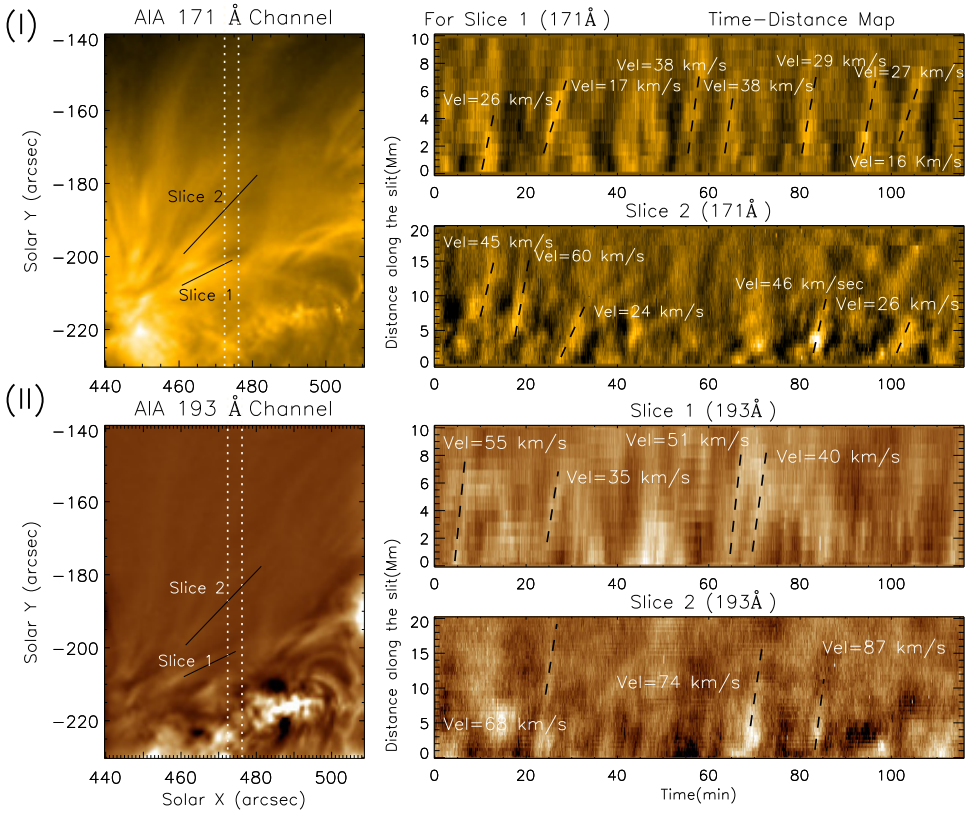

FIGURE 3.6: (I) *Left*: AIA 171 Å image showing the locations of the slices chosen for time-distance analysis. The vertical dashed lines mark EIS slit positions. *Right*: Enhanced time-distance maps constructed from slice 1 (top) and slice 2 (bottom). The inclined black dashed lines represent the slope of the individual ridges used in the propagation speed estimation. (II) Corresponding plots for AIA 193 Å channel.

3.4 Summary and Conclusions

We have studied the properties of PDs in an active region fan loop system using simultaneously observed imaging data from SDO/AIA and spectroscopic data from Hinode/EIS. At the 6 loop-crossing locations, identified from the AIA 171 Å images, we observe oscillations in all the line parameters for the two EIS lines (Fe XII 195.12 Å and Fe XIII 202.04 Å). The periodicity of these oscillations ranges from 3 to 10 min. The intensity oscillations obtained from AIA 193 Å and 171 Å also show a similar periodicity. AIA image sequence and the powermaps of the region clearly indicate that these oscillations are connected with the PDs propagating along the fan loops. The apparent propagation speeds of PDs were found to be different for the AIA 193 (T≈1.3 MK) and AIA 171 (T≈0.6 MK) channels. The average speed ratio is ≈ 1.5 compared to the theoretical value 1.47 expected for these two channels.

We also performed correlation analysis to find coherency between different line parameters which reveals a relatively high correlation between intensity and Doppler shift at all the LCPs. It may be noted that in some cases the periods of different line parameters are not exactly the same (see Table 3.2). The listed values in Table 3.2 are only the dominant periods which are in most cases accompanied by other peaks (although not significant). The existence of multiple periods often degrades the correlation value. It may be useful to filter the time series to improve this but the small amplitudes of oscillations combined with the noise make it difficult to achieve.

The temperature-dependent propagation speeds and relatively high correlation between intensity and Doppler shift which are expected for a propagating slow magneto-acoustic wave, favour the wave interpretation for the observed PDs. On the other hand, the observed PDs were not so regular, with changing inclinations and intensities from one ridge to the other as can be seen from the time-distance

maps. The R-B asymmetry analysis also reveals a negative R-B value for both the EIS lines indicating a blue wing enhancement. These properties suggest the possible interpretation of the observed PDs as quasi-periodic upflows. In fact, some of the latter properties can actually be explained with a propagating slow wave scenario if one considers the line profile resulting from the superposition of a high-speed component on a nearly stationary background. This supersposition leads to profile asymmetry producing a blue-wing enhancement and also results in coherent oscillations in all the line parameters (Verwichte *et al.* 2010; Hara *et al.* 2008).

Based on the observed properties, we suggest a possible co-existence of waves and flows causing the PDs found in this region. Here we want to emphasise that it is very difficult to distinguish these two effects from each other from the intensity images as well as from the spectroscopic observations as presented here. Recently De Moortel *et al.* (2015) made synthetic spectra to justify one scenario over the other and they found that most of the observables which can give us an indication for the same (between wave and flow scenario), are not measurable with the current instrument capabilities. Efforts shall be made to combine theoretical modelling with observations which will help us to decouple these two phenomena from each other.

Chapter 4

Reflection Of Propagating Slow Magneto-acoustic Waves In Hot Coronal Loops[†]

4.1 Introduction

MHD waves play an important role in understanding the solar structures and the coronal heating process (Roberts *et al.* 1984; Nakariakov and Verwichte 2005; Banerjee *et al.* 2007; De Moortel and Nakariakov 2012). Extreme ultra-violet (EUV) imaging analysis provides access to the loop diagnostics i.e loop density, temperature, flows including estimation of magnetic field (Roberts *et al.* 1984; Aschwanden *et al.* 1999a; Nakariakov *et al.* 1999; Nakariakov and Ofman 2001; Verwichte *et al.* 2013). Slow MHD waves in the solar corona were first observed by Ofman *et al.* (1997); DeForest and Gurman (1998); Berghmans and Clette

[†]Results of this work are published in Mandal *et al.* (2016b).

All the animations that are referred to in this chapter are available at `https://doi.org/10.3847/0004-637X/828/2/72`

(1999) as quasi-periodic propagating disturbances(PDs) channeling through coronal structures. Using various properties of these observed disturbance from imaging data, they were initially categorized as slow waves (Kiddie *et al.* 2012; Marsh *et al.* 2009; Marsh and Walsh 2009). On the otherhand, analysis of simultaneous imaging and spectroscopic data shows that such disturbances could well be the upflows (De Pontieu *et al.* 2009; Tian *et al.* 2011a; Mandal *et al.* 2015). Despite these facts, Verwichte *et al.* (2010) showed that slow wave is still a preferred explanation for these propagating disturbances.

Standing slow waves have also been studied very closely by many authors. Wang *et al.* (2002, 2003a,b) observed damped Doppler shift oscillations in hot coronal lines with SoHO/SUMER. They interpreted these oscillatory Doppler shifts of the high temperature (T $>$ 6 MK) Fe XIX and Fe XXI lines as standing slow waves generated by an impulsive trigger at one of the loop footpoints. Wang *et al.* (2005) analyzed 54 Doppler shift oscillations in 27 flare-like events from SOHO/-SUMER and interpreted them as being caused by standing slow waves because they exhibit a quarter period phase shift between the intensity and velocity oscillations. Mariska (2005) reported Doppler shift oscillations in S XV and Ca XIX lines observed with BCS/Yohkoh where they found oscillations with a period of few minutes (Mariska 2006) (from HINODE/EIS). Using forward modelling, Yuan *et al.* (2015) synthesized SDO/AIA and SoHO/SUMER emissions to study the standing slow wave modes in a hot flaring loop. Apart from recovering the quarter period phase shift between intensity and Doppler velocity, these authors also found asymmetric emission intensity during the positive and negative temperature perturbation phase.

Selwa *et al.* (2005) generated slow waves numerically by applying temperature perturbation pulses at different positions in the loop and observed that the generated mode depends upon the location of the pulses. The study of various aspects of the slow wave generation have been extensively carried out using 2D and 3D MHD

models (Selwa *et al.* 2007; Selwa and Ofman 2009; Ofman and Selwa 2009; Ofman *et al.* 2012). Using a 3D MHD model Ofman *et al.* (2012) concluded that the impulsive injection of the energy at the active region loop footpoint can excite slow and fast waves simultaneously along with the observed outflows. Damping of the Doppler oscillations (observed with SUMER) have also been studied thoroughly by Ofman and Wang (2002). Using a 1D MHD code simulation, these authors concluded that the thermal conduction plays the significant role in damping of these waves rather than the compressive viscosity. Damping of the waves have been further studied by De Moortel and Hood (2003, 2004); De Moortel *et al.* (2004) where they have included the gravitational stratification, field line divergence and mode coupling apart from thermal conduction and viscosity to damp these waves.

Reflection of slow MHD waves propagating through the coronal loops have been reported recently by Kumar *et al.* (2013) using high resolution imaging data from the SDO/AIA high temperature 131 Å and 94 Å channels. Slow wave generated at one of the footpoints, was reflected back and forth, a couple of times from the loop footpoints before fading out. The propagation speed of the wave was about 460-510 km s^{-1}, which is very close to the sound speed at the temperature obtained from the DEM analysis. Fang *et al.* (2015), using a 2.5D MHD simulation and forward modelling, reproduced such slow wave reflections in a hot coronal loop. A flare-like instantaneous energy perturbation at the footpoint evaporates a plasma blob which then propagates as a slow wave front. The wave then bounces back and forth along the loop as observed by Kumar *et al.* (2013). Fang *et al.* (2015) also used line parameters of the synthesized SUMER Fe line to show that these are propagating mode. With the use of a particle tracer, these authors confirm that such propagating disturbances better agree with a dominant wave scenario along with a mass flow component. Recently Kumar *et al.* (2015) reported quasi-periodic intensity oscillations in AIA extreme ultraviolet (EUV) channels along with the X-ray channel of Fermi gamma ray burst (GRB) monitor. These authors also propose the repetitive reconnection scenario on a fan-spine magnetic topology

to explain the observed periodicity.

4.2 Observation and Data reduction

The datasets used in this study are obtained from different active regions observed by the X-Ray Telescope (XRT) (Golub *et al.* 2007) on board HINODE (Kosugi *et al.* 2007) and the Atmospheric Imaging Assembly (AIA) onboard Solar Dynamic Observatory (SDO).

The XRT data is calibrated using xrt_prep.pro which performs the correction for near-saturated pixels, removal of spikes, correction for contamination spots and removal of the CCD bias and the dark current. The final pixel scale and the cadence for each XRT observations are given in Table 4.1. The AIA level 1.0 data have been reduced to level 1.5 using the *aia_prep.pro* which makes the necessary instrumental corrections. The final pixel scale, in both X and Y directions, is $\approx 0.6''$. The cadence is 12 seconds.

TABLE 4.1: Details of the XRT ('Be-thin') observations

Date	Time (UT)	Active Region	FOV	Cadence (s)	Pixel scale
10-Dec-2015	04:30-05:16	AR 12465	$2106'' \times 2106''$	121	$4.1''$
22-Jan-2013	08:30-09:29	AR 11654	$394'' \times 394''$	61	$1.03''$
27-Jan-2013	20:09-20:59	AR 11661	$394'' \times 394''$	61	$1.03''$

4.3 Data analysis and results

4.3.1 XRT Observation on 10^{th} December 2015

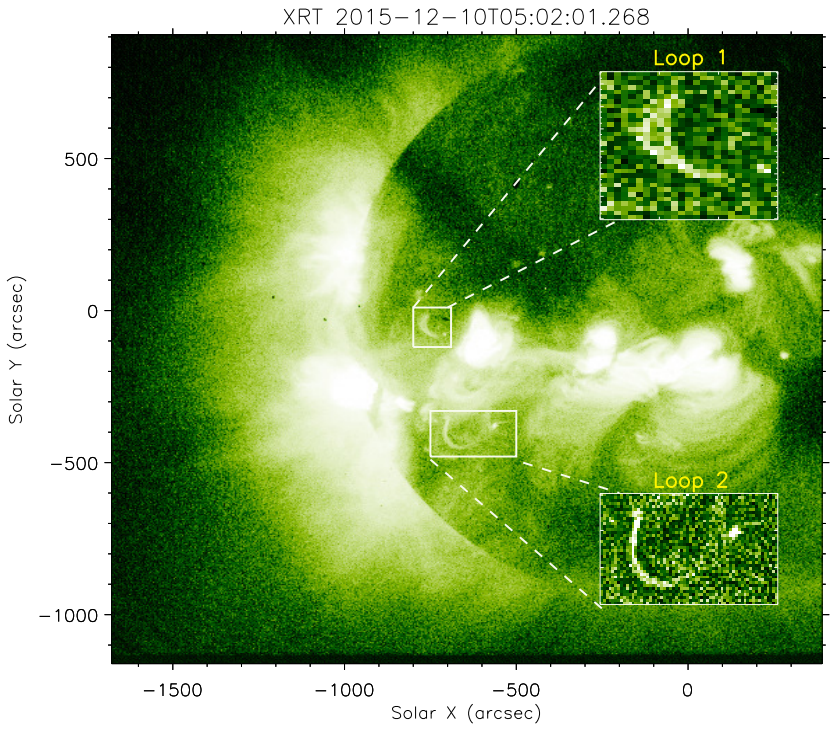

FIGURE 4.1: The context image showing the full field of view of the observation on 10^{th} December, 2015. Two white boxes highlight the loops of our interest. The zoomed in view of these individual boxes are also plotted on top of the image.

We used HINODE/XRT data taken in Be-thin filter on 10^{th} December 2015. Figure 4.1 shows the context image of the observation along with the two loops, (loop 1 and loop 2) from an active region AR 12465, which show reflecting wave propagation.

From the movie (movie 1, available online) we see that the onset of the propagating intensity disturbance is caused by a flare which occurred at one of the footpoints. The disturbance then reflects back and forth a couple of times before fading out. To see the propagation of this perturbation through the loop, we stacked different

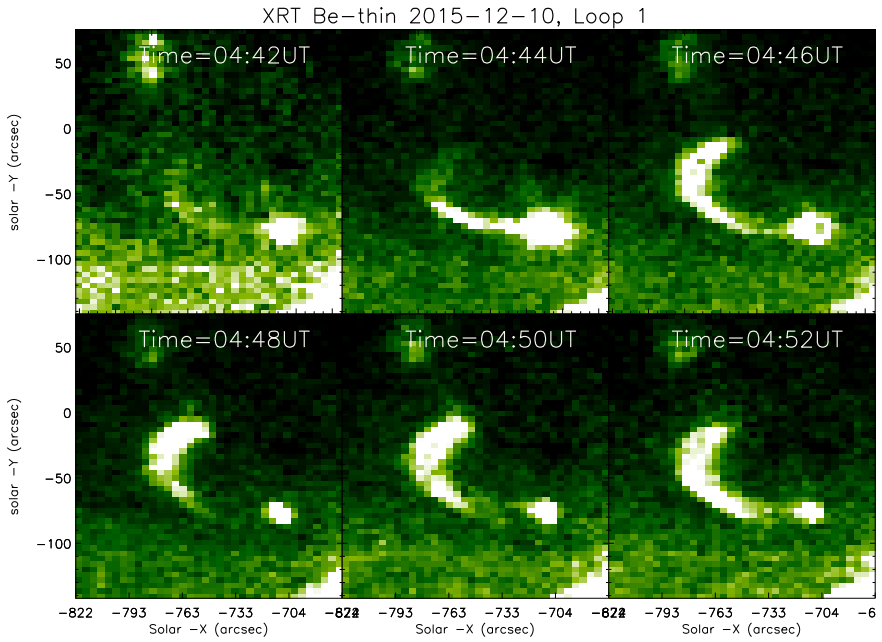

FIGURE 4.2: Sequence of base difference images for loop 1. The bright intensity perturbation starts from one footpoint at 04:42 UT and then reflects back from the other footpoint at 04:52 UT. An animated version (movie 1) is available online.

snapshots of the loop 1 in Figure 4.2 where one full reflection is seen clearly. We scaled each image to enhance the propagating intensity for better visualization. Speeds of these perturbations are estimated by using the time-distance maps. We put artificial slits tracing the loops to create the time-distance maps. Figure 4.3 shows the artificial slit positions and the time-distance maps, created using base difference image sequence, for both loop 1 and loop 2.

For the loop 2 (panel (a) in Figure 4.3) we see a single reflection within the duration of the observation. The period obtained from the time-distance map (panel (b) in Figure 4.3) is $\approx$ 20 minutes. The slopes of the bright ridges are an estimate of the speeds and we obtained a speed of 433 km s^{-1} and 257 km s^{-1} for the ridge 1-2 respectively. For the second loop (loop 2, panel (c) in Figure 4.3) we see two clear reflections before the signal faded off. The estimated speeds for the ridges

3-5 are 391 km s^{-1}, 219 km s^{-1}, 251 km s^{-1} respectively. Loop lengths obtained by tracing the loops are 172 Mm and 61 Mm for loop 1 and loop 2 respectively. These loop lengths are projected lengths and thus can be an underestimation of the actual lengths.

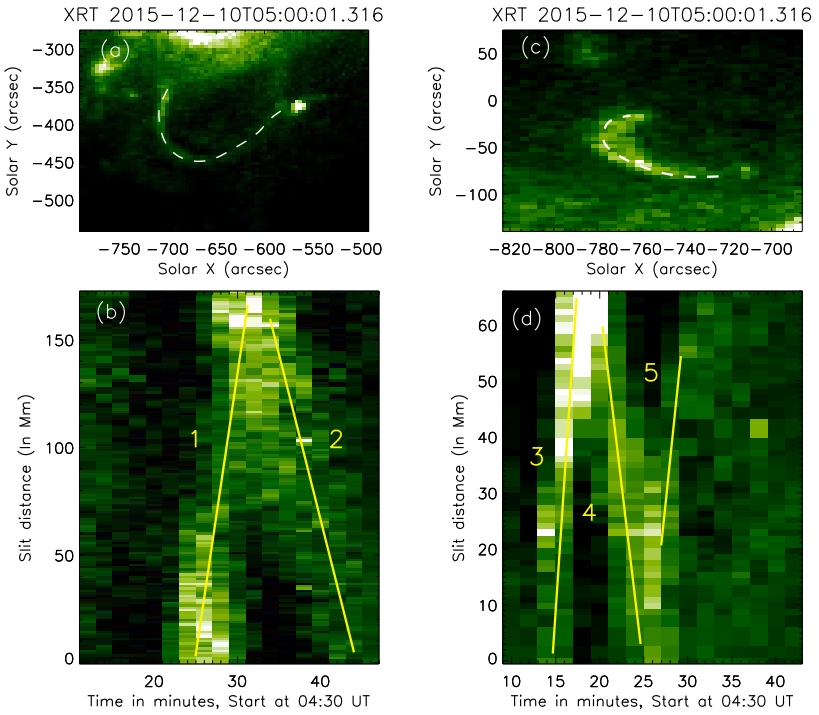

FIGURE 4.3: (a)-(b) Snapshot of the loop 2 and the obtained histogram equalized time-distance map. The dashed lines show the slits used to generate these maps. (c)-(d) Same as previous but for loop 1. The yellow solid lines (1-5) in both the time-distance maps, highlight the slope of ridges.

As we see from the time-distance maps and also from the movie, the intensity amplitudes get damped as they propagate along the loop. To get a quantitative measure of the damping we chose a box as shown in panel (a) in Figure 4.4 to see the evolution of the averaged box intensity with time. The box is chosen close to the footpoint to avoid the line of sight integration effect because of the loop orientation and also to get a good signal to noise ratio near the footpoint. The averaged box intensity is plotted in panel (b) where each peak corresponds to one reflection.

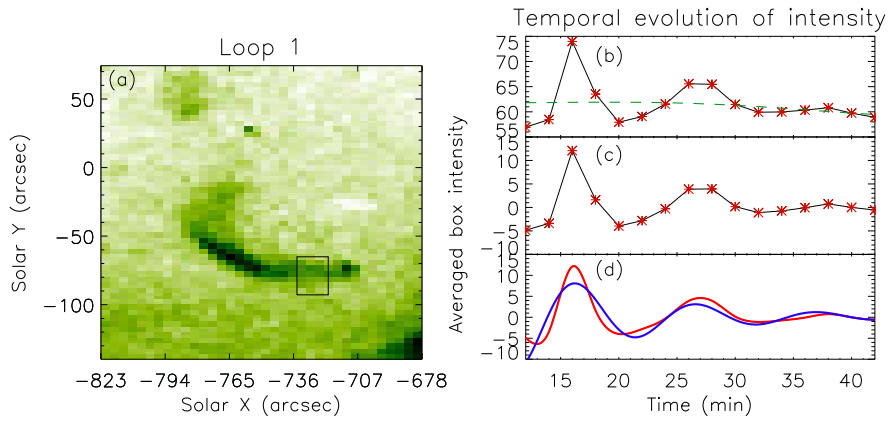

FIGURE 4.4: (a) Snapshot of the region showing the loop structure (in inverted color). The black box outlines the region selected to extract the intensity. (b) Temporal evolution of the averaged intensity over the box. The small trend, highlighted with a dashed green line, has been subtracted from the original curve to produce the detrended light curve as shown in panel (c). (d) Interpolated light curve is shown with the red line and the fitted decaying sinusoidal is shown in the blue solid line. Start time of these profiles are 04:30 UT. An animated version (movie 2) is available online.

We see that with each reflection the amplitude is decreasing. A small trend, as obtained by smoothing the original curve with an increasing window size between 3 to 6 points (i.e time frames), is subtracted from the original curve (panel (b)) to produce the detrended curve shown in panel (c) in Figure 4.4. To measure the period and the decay time, we first do a 20 fold spline interpolation of the original detrended curve, shown as red solid line in panel (d), to produce a smooth curve. Then we fit the interpolated profile with a damped sinusoidal function of the form

$$I(t) = \mathrm{A}\sin(\frac{2\pi t}{\mathrm{P}} + \phi)\exp(\frac{-t}{\tau}) \tag{4.1}$$

where A,P, τ and ϕ are the amplitude, period, decay time and the phase respectively. The best fitted curve is shown in blue solid line in panel (d) of Fig.4.4. The estimated period is 10.1 minutes whereas the damping time is 10.6 minutes.

4.3.2 XRT observation on 22^{nd} January 2013

We used XRT data taken in Be-thin filter on 22^{nd} January 2013 from 8:30 UT to 9:29 UT. The full field of view, shown in panel (a) in Figure 4.5, is $394'' \times 394''$. The loop of our study is located in active region AR NOAA 11654 in the westward solar limb. We further selected a region of interest (ROI) where the loop is seen clearly and all the analysis has been done on this selected region (panel (b) in Figure 4.5).

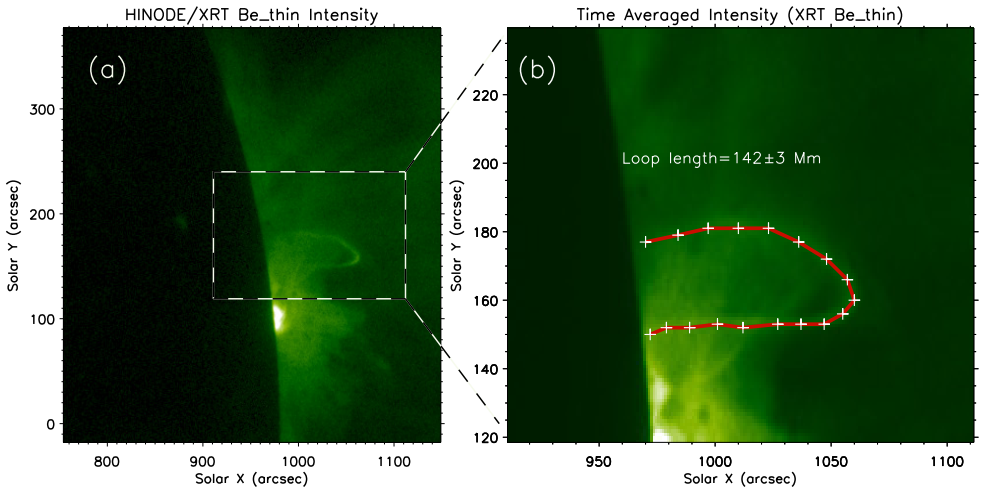

FIGURE 4.5: Panel (a) shows the full field of view of the 22^{nd} January XRT data. The black-white rectangular box shows the region of interest (ROI) selected for the analysis. A movie of the ROI is available online (Movie 3). Panel (b) shows the time-averaged image of the ROI. The loop length calculated by tracing the loop (white '+' signs) is printed on the plot. The red line is used to create the time-distance plot.

The wave, appearing from one of the loop footpoints (located on the far-side of the limb) at 08:59 UT, gets reflected from the other footpoint and travels along the loop before fading away. To see the propagation of the wave clearly, running difference images have been created as shown in panels (a-h) in Figure 4.6. We see the onset of the propagation at 08:59 UT and we mark it with a white arrow (panel (a) in fig 4.6). We also mark the position of the intensity enhancement in

the previous frame, seen as a black region following the white, with the yellow arrows. At 9:07UT the wavefront reaches the other footpoint and gets reflected back from there. We have estimated the projected loop length to be 142±3 Mm by tracing the points along the length of the loop (the '+' signs in Fig. 4.5). Using the measured loop length and the time the wavefront takes to travel from one footpoint to another (08:59 UT to 09:07 UT), we have an estimate of the average speed of wave propagation and it is $\sim$ 295 km s^{-1}.

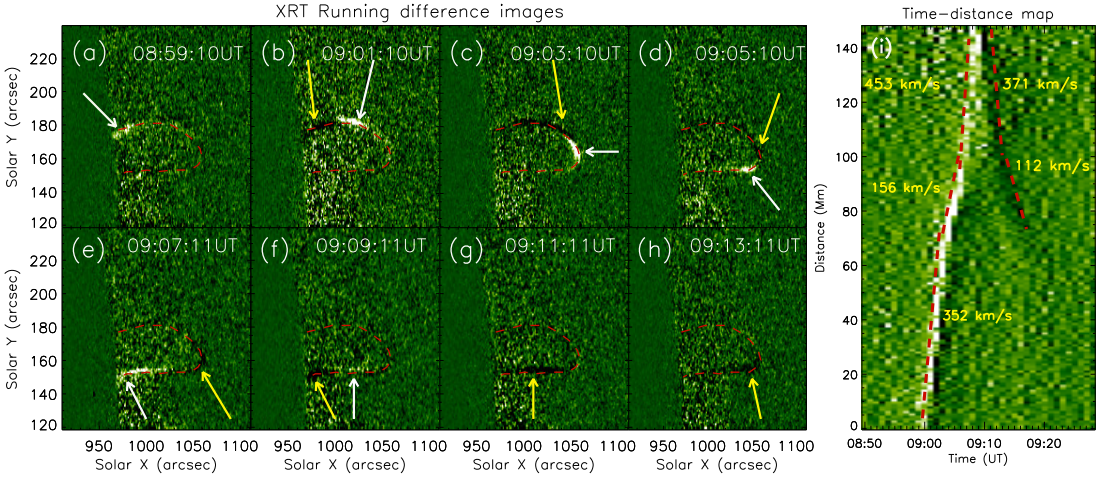

FIGURE 4.6: Panels (a-h) show the running-difference images created from the XRT Be-thin filter intensity image sequence. The white and yellow arrows show, in each time frame, the current and the previous position of the wavefront respectively. Panel (i) shows the time-distance map from the running-difference image sequence. The white and black inclined ridges show the forward and reflected wave propagation along the loop while the red lines indicate the slope of these ridges.

To measure the propagation speed more accurately we have created the time-distance map from the running difference image sequence, as shown in the panel (i) in Figure 4.6. The time-distance map has been created using an artificial slit which traces the loop (white '+' signs in panel (b) in Figure 4.5 represent the slit position) and extends the slit width by two pixels across to increase the signal to noise ratio. From the map we clearly see the reflection of the wave from the other end of the loop and then the wave propagates back along the loop before fading away around midway. The slopes of the ridges represent the propagation speeds. Different slopes of the ridges in the time-distance map reflect the change of the

loop orientation with the line of sight as the wave propagates along the loop. This event was also co-observed by the 'Ti-poly' filter, but neither the loop nor the intensity disturbance was seen in this channel.

4.3.3 XRT observation on 27^{th} January 2013

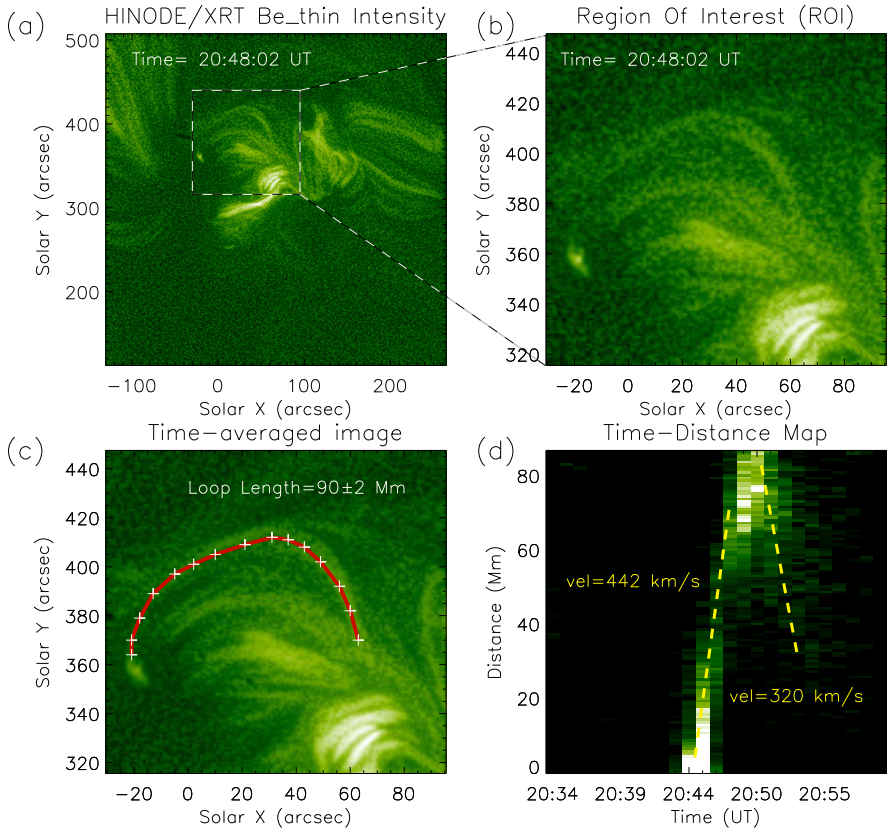

FIGURE 4.7: Panel (a) shows the full FOV of the XRT data. The white box indicates the 'region of interest'(ROI) that we have selected for the analysis. The zoomed view of the ROI is shown on the panel (b). Panel (c) shows the manually traced loop to calculate the loop length. Processed time-distance map for the traced loop is shown on the panel (d). Estimated speeds are printed on the panel. An animated version (movie 4) is available online.

On 27^{th} January 2013, a similar event was observed with the XRT Be-thin filter. A flare like brightening at one of the footpoints is the source of the wave which propagates along the loop. The top panel in Figure 4.7 shows the full FOV of the XRT observation and the region of interest respectively. We have estimated the

loop length by tracing points along the loop and the length is equal to 90 Mm (with errors less than 5 Mm).

From the movie (Movie 4) we see that the wave is damped rapidly as it propagates through the loop and it faints away as soon as it gets reflected from the other footpoint. This is also seen in the processed time-distance map (bottom last panel in Figure 4.7) we created by placing an artificial curved slit following the loop as shown by the '+' signs in Figure 4.7. The processed time-distance map has

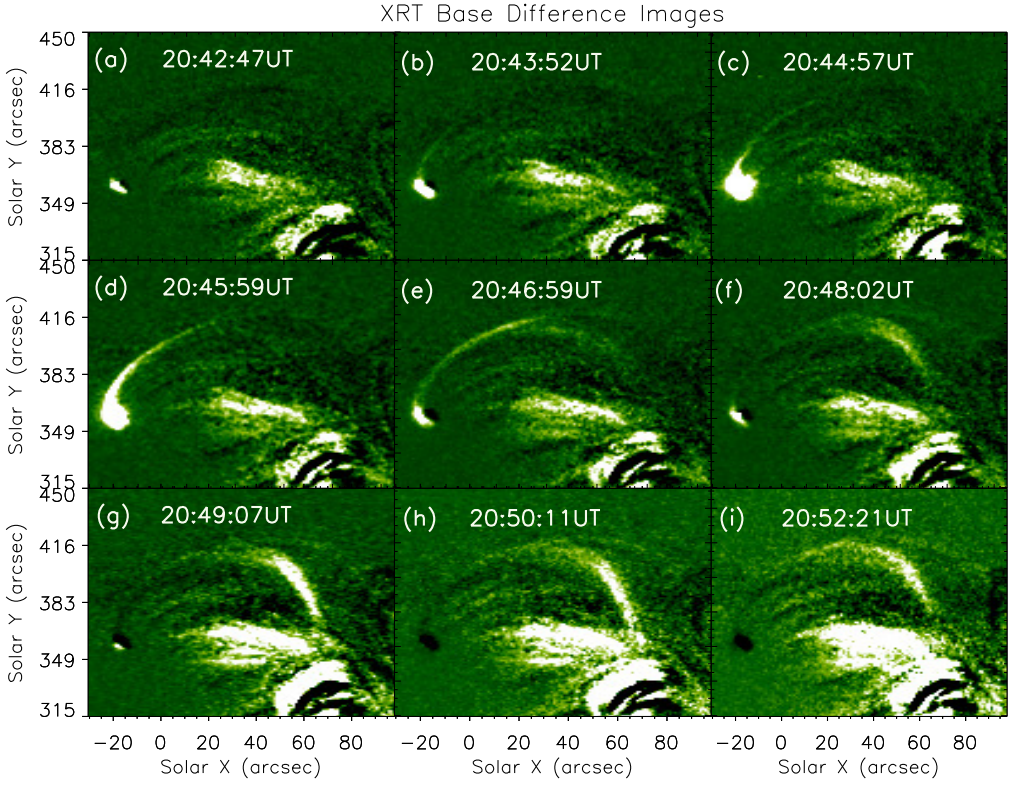

FIGURE 4.8: Base difference XRT images of the ROI, showing the wave propagation from one loop footpoint to the other. Each image is scaled individually to highlight the wavefront.

been created by scaling individual time in the original map to enhance the bright pixels. In the processed time-distance map we see a reflection signature, though not prominent, from the other footpoint before the signal dropped down considerably.

The speed calculated from the inclined ridges (highlighted with yellow dashed line) are 442 km s^{-1} and 320 km s^{-1} respectively.

The propagation and the reflection of the wave is prominently visible in the base-difference images shown in Figure 4.8. Panel (a-h) shows the intensity propagating from the one footpoint to other and in panel (i) we see the reflected part moving in the other direction.

4.3.4 AIA observation

The XRT 'Be-thin' filter mostly observes the 'hot' plasma (the response function of 'Be-thin' filer peaks at 10MK). This leads to the fact that the event observed in this filter is likely to be captured in hotter channels of AIA (94 Å and 131 Å). Despite of this, we found only one event (on 22^{nd} January, 2013) where the loop is also simultaneously seen with AIA. This is because the AIA 94 Å and AIA 131 Å channels have a second peak around 1.5 MK and 0.5 MK respectively, next to their expected response at 10 MK. These secondary peaks contaminate heavily when the loop is on disc rather than when it is on the limb. Also for the other events, the plasma may be too hot to be seen in any of the AIA channels. It must be mentioned here that though we did not see the loop (except for the event on 22^{nd} January, 2013), we have captured the time evolution of the loop footpoints for all the other events. For the event on 22^{nd} January, 2013 we could not locate the footpoint as it was on the far side of the Sun.

For the event on 22^{nd} January 2013, we found that the loop is also detected in the AIA 94 Å channel (only) indicating the presence of a high temperature plasma in the observed loop. We have used corresponding SDO/AIA data in the 94 Å channel taken from 8:30 UT to 9:30 UT. We used this data to co-align the two instruments and the final XRT coordinates are obtained after correcting

for the offsets. The left panel in Figure 4.9 shows the time averaged image of base-difference image sequence of the AIA 94 Å channel. We also estimate the loop length in a similar way as the XRT measurement and the length is equal to 137 ± 2 Mm. From the movie (movie 5, available online) we clearly see that the wave starting from one footpoint gets reflected from the other footpoint and faints away after traveling a certain distance along the loop-length. This feature is also seen clearly from the time-distance map created from the AIA base-difference image sequence. Two oppositely inclined ridges are visible in the map indicating a clear reflection signature. We also estimated the propagation speed from the slope of the ridges and they are shown in Figure 4.9.

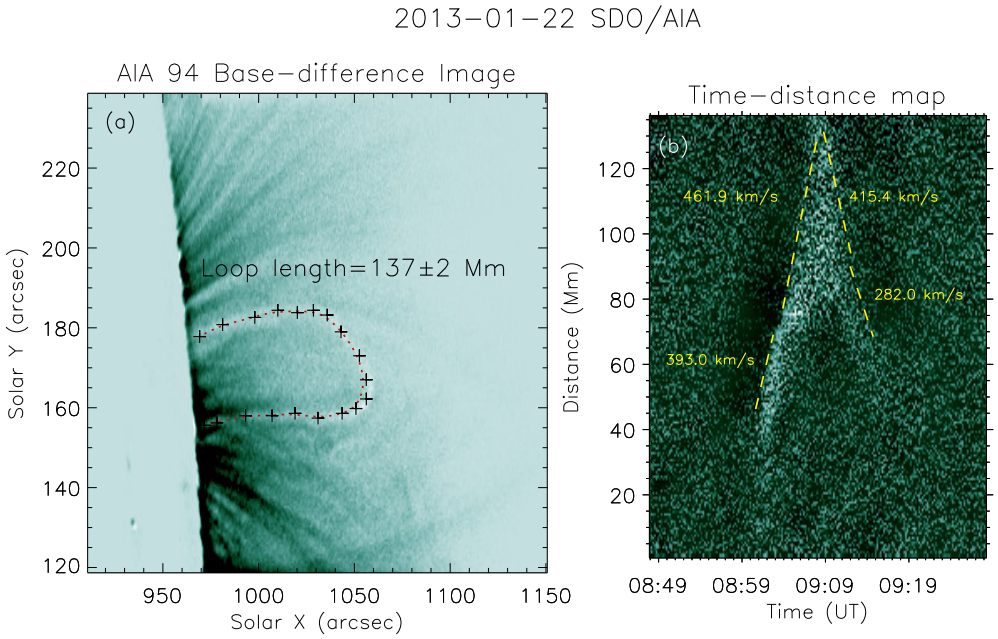

FIGURE 4.9: (a) AIA 94 Å time averaged image created from the base-difference image sequence. The detected loop is marked by '+' signs. (b) The time-distance plot showing two oppositely inclined white ridges. Yellow lines indicate the slope of these ridges. An animated version (movie 5) is available online.

4.4 DEM analysis

Wave propagation through a loop largely depends upon the physical parameters of the loop density, temperature etc. Since the sound speed in a medium depends on its temperature, we performed automated temperature and emission measure analysis, using a SolarSoft code, as developed by Aschwanden *et al.* (2013) to estimate average density values and temperature inside the coronal loop.

In order to estimate the DEM, the SolarSoft code co-alignes AIA images in different EUV passbands (94 Å, 131 Å, 171 Å, 193 Å, 211 Å, 335 Å) using solar limb fit. Using the forward fitting of the observed DEM distribution with that of the model DEM distribution, the peak emission measure and the peak temperature at a particular pixel is determined. In our case, the loop is only poorly visible in AIA 94 Å channel. Thus the density and temperature values, obtained from the DEM analysis, are only rough estimations for both the parameters. This order of magnitude estimate is sufficient for our purpose as we insert these values in our numerical model (described in subsequent section) as initial loop parameters. To check for any spatial as well as temporal evolution of the loop parameters, we performed DEM analysis at three different locations at three different times. One such case is shown in detail in Figure 4.10. The estimated average loop density and temperature are $\approx 10^9$ cm^{-3} and $\approx$10 MK respectively. Using this temperature value, the sound speed within the loop is $c_s \sim 152\sqrt{T(\mathrm{MK})} \sim 480$ km s^{-1}. The other two DEM measurements are shown in Figure 4.11.

4.5 Generation Mechanism

The generation mechanism of such waves is not fully understood yet. There are evidences of small (-micro) flares, occurring at the loop footpoints, as seen in our

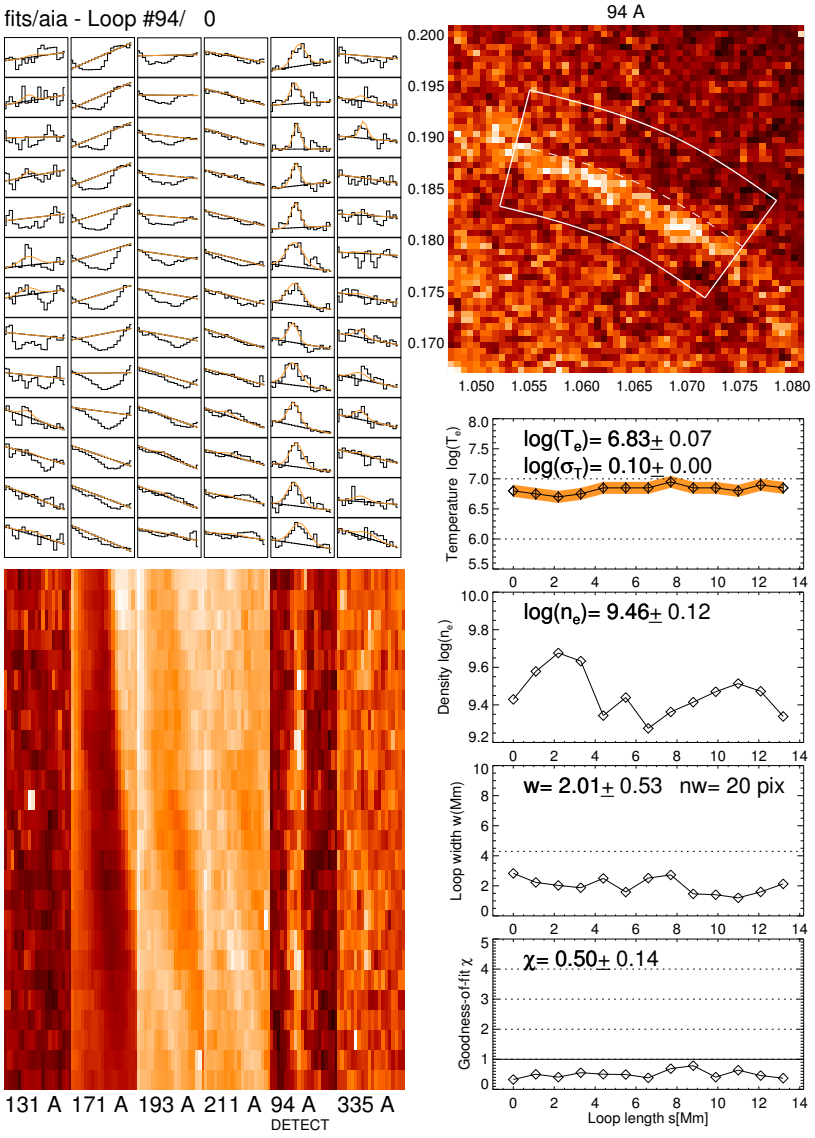

FIGURE 4.10: Automated DEM analysis performed with the AIA dataset. The loop is only seen in the AIA 94 Å. The top left panels show the Gaussian fits performed on the selected loop structure (top right panel) to estimate the loop width. The obtained loop density (n_e), loop temperature (T_e) and the goodness of fit (χ) is also plotted in different panels.

events also, to be the generator of the waves. See Wang (2011) for a complete review on this.

In the event on 22^{nd} January, the flare happened at the far side of the Sun and thus it was hidden from us (STEREO also did not capture the event due to corser cadence of 5 minutes). We did capture the loop footpoint for the event on 27^{th}

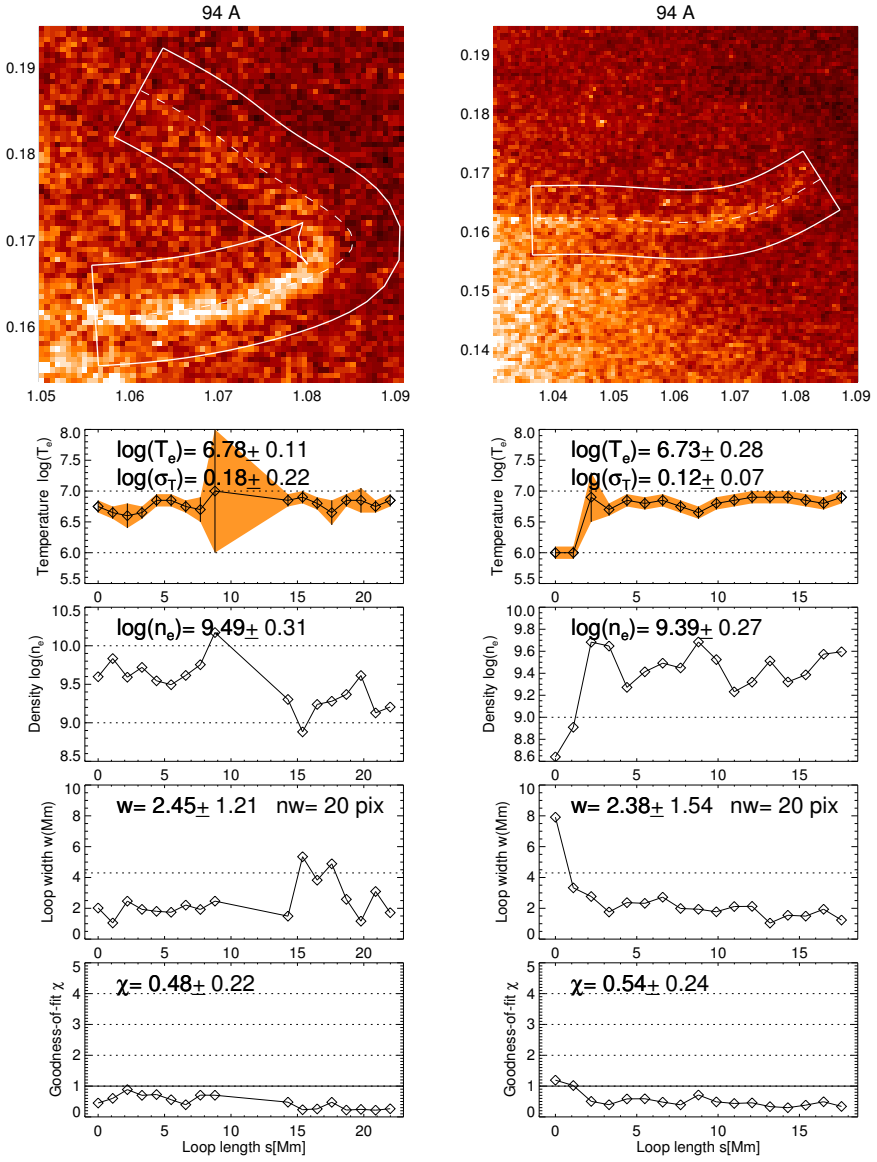

FIGURE 4.11: Automated DEM measurements same as Figure 4.10 but for two different location at the loop. The error values are derived from the width of the Gaussian fitting (see Aschwanden *et al.* (2013) for details) and may be an underestimation of the actual uncertainties.

January from XRT as well as from AIA EUV channels. Figure 4.12 shows the time evolution of the loop footpoint as seen with XRT. We notice a complex mini-loop like structures at the footpoint with many spines as revealed in the image sequence of Figure 4.12. We also notice that an intense brightening which starts at the right end of the loop footpoint (panel (c)) moves towards the left in the next time frame (panel (d)). This observed occurrence and evolution of the brightening at the

loop footpoint resembles very much the 'blowout-jet' examples found previously (Moore *et al.* 2013).

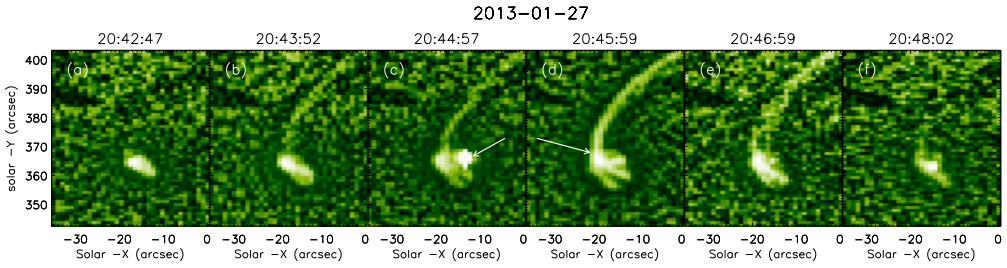

FIGURE 4.12: Snapshots showing the loop footpoint and its temporal evolution, for the event on 27^{th} January, as seen by the XRT Be-thin filer. All the images have been scaled to highlight the footpoint. The white arrows in panels (c) and (d) indicate the brightening position in the corresponding frames.

Though the loop is not visible in any of the AIA channels but the loop footpoint is clearly visible in all the EUV channels. Figure 4.13 shows the time evolution of the footpoint in five EUV channels of AIA (171 Å, 131 Å, 94 Å, 193 Å, 304 Å). Panels (a-e) show the snapshots of the footpoints at the time when the flare peaks. We see a complex loop arcade with a spine forming at the top of the structure. From the movie (movie 6) we also notice that the AIA cooler channels (171Å and 304Å) along with a hotter channel (193Å) capture a small 'filament like' dark feature rising with the evolution of the flare (Sterling *et al.* 2015). Though we must emphasize the fact that the initial location of the filament before the flare is not clearly visible. To see the photospheric magnetic filed configuration associated with this structure, we overlay the Helioseismic and Magnetic Imager (HMI) line of sight (LOS) magnetic filed contours ($\pm$ 20 G) on top of the AIA images. We do not see a clear bipolar structure around the footpoint region in this case suggesting the fact that the reconnection might have happened higher in the atmosphere. Panels (f-j), in Figure 4.13, show the snapshots of the same region when the ejecta is seen to propagate through the spine. Though the ejected material is poorly visible in the AIA 94 Å channel but it shows up in rest of the channels. A yellow rectangular

box, which marks the footpoint region in panels (a-e), is also overplotted in panels (f-j) for better comparison.

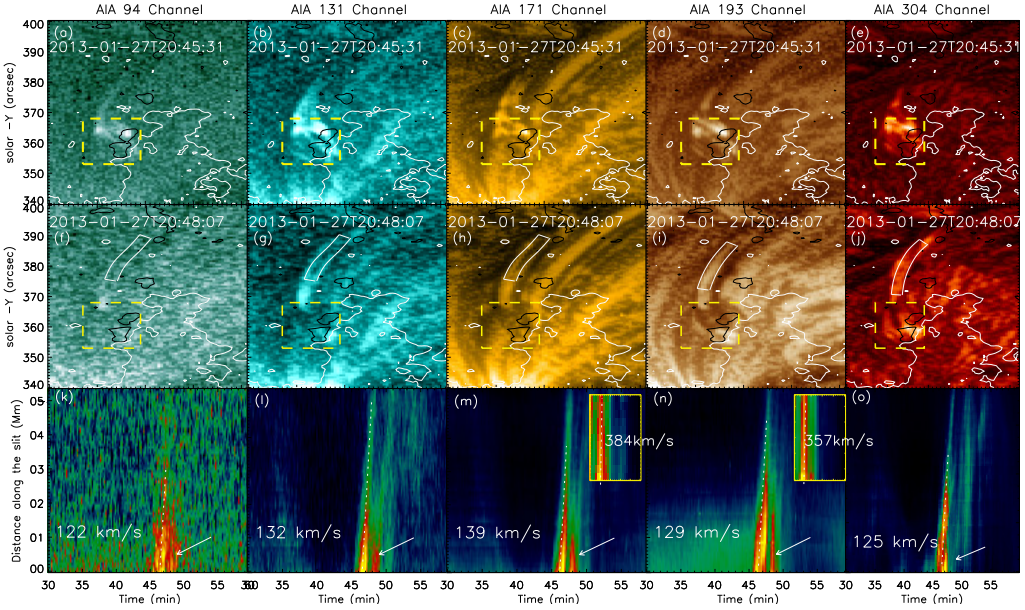

FIGURE 4.13: Panels (a-e) show the snapshots of the footpoint at the peak flare time in five AIA EUV filters (171 Å, 131 Å, 94 Å, 193 Å, 304 Å). The black and white contours represent the HMI LOS negative and positive fields (±20 G). The yellow rectangular box covering the footpoint is used create the light curved shown in Figure 4.14. Panels (f-j) show the same region at a later time. White rectangles highlight the position of the artificial slit used to generate time-distance maps (histogram equalized for better visualization) shown in panel (k-o). Speeds measured by calculating the slope of the white dotted line, are printed in each panel. A second peak in the time-distance map is highlighted by a white arrow in each panel ((k)-(o)). Speed measurements for this second peak is also shown in insets (panel (m)-(n)). Start times of the time-distance maps are 08:00 UT.

The footpoint structure almost disappeared at this moment (panels f-j) leaving the spine through which the ejected plasma moves. To measure the propagation speed of the plasma, in the plane of sky, we create the time-distance maps for all the channels by placing an artificial slit as indicated by a white curved rectangle in panels (f-j). The obtained time-distance maps for individual channels are plotted in the bottom panel of Figure 4.13 (panels (k-o)). Here we see two slanted ridges in all the channels except the 304 Å channel where the second ridge is not visible.

The speeds, calculated from the slopes of the first ridge in all the cases, ranges from 122-139 km s^{-1}.

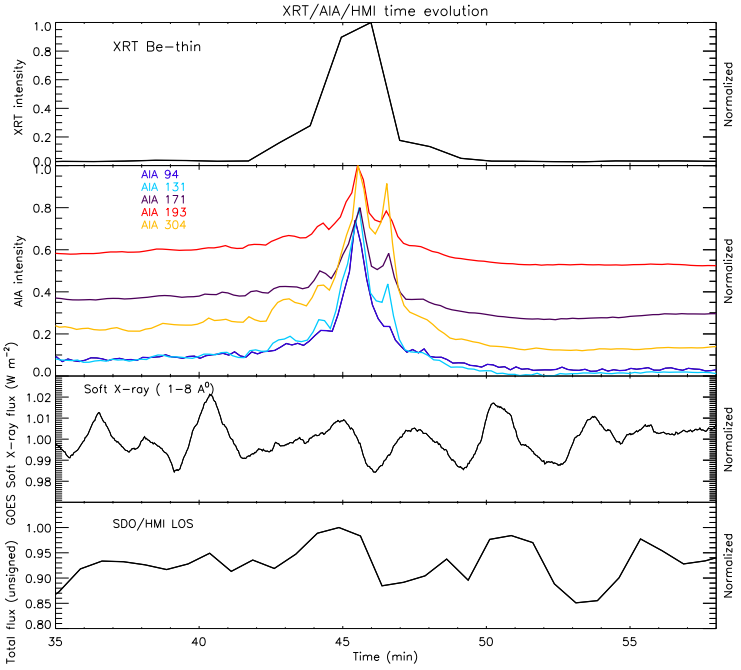

FIGURE 4.14: Top panel shows the time evolution of the box averaged intensity for the XRT data. AIA intensities for the five AIA channels, are plotted in the middle panel. Bottom two panels show the light curve for GOES soft X-ray flux (1-8Å) and the HMI unsigned total flux (averaged over the box). Start times of the profile are 08:00 UT.

The occurrence of this ejecta coincides with flare peak time (at 20:45 UT) as seen from XRT . The second ejecta, which occurred $\approx$ 2.5 minutes later, propagates with a much faster velocity than the first ejecta. The measured speeds in this case are 384 km s^{-1} and 354 km s^{-1} in 171 Å and 193 Å channels respectively.

To understand the evolution of the observed footpoint intensity and its association with the photospheric magnetic field, we plot in Figure 4.14, the temporal evolution of the intensities from AIA and XRT and the unsigned HMI magnetic flux

averaged over the yellow box shown in panel (a) of Figure 4.13. GOES soft X-ray flux (1-8 Å) is also in the plot. We see a clear association of the XRT intensity peak with intensity increments in all the AIA EUV channels. Also this increment is accompanied by a soft X-ray flux enhancement. A closer investigation on the AIA light curves shows another peak, approximately 1 minutes later, with smaller magnitude than the first one. It is worth to mention here that the second peak is very weak in 94 Å channel and there is no such peak seen in XRT intensity profile. The absence of the second peak in the XRT profile can be explained by considering the coarser time and spatial resolution of the XRT compared to the AIA and also the filter response of the XRT 'Be-thin' filter. In the last panel of Figure 4.14 we plot the total (unsigned) flux from the boxed region and we notice that there are two dips on the profile around the flare time (though these dips are not significantly strong and comparable to the fluctuations seen in the time series). Note the second ridge, found in the time-distance maps in Figure 4.13, originates due to the second peak found in the intensity profiles of AIA. We propose a scenario where the chromospheric plasma gets heated rapidly due to the flare and produces the high speed ejecta which is seen to propagate in all the coronal channels. Here we want to highlight the fact that there is a delay of ≈1.5 minutes between the second intensity enhancement and occurrence of the high speed plasma. Such a scenario of rapid heating of the chromospheric material also explains the absence of this second ejecta in chromospheric 304 Å channel.

Now we analyze the event occurred on 10^{th} December, 2015. XRT has observed this event with 4×4 spatial binning, resulting in a spatial scale of $4.1''$ in both x and y directions. Thus we could not resolve the footpoint from the XRT data (the cadence was also coarser in this case, 121 seconds). Using the AIA data, we do not see the loop structure in this case too but the footpoints (for both loop1 and loop2) are seen in all the AIA EUV channels. Panels (a1-e6), in Figure 4.15, show the temporal evolution of the loop1 footpoint in five EUV channels of AIA. Similar to the previous event, here also we see a jet spine at one side of the

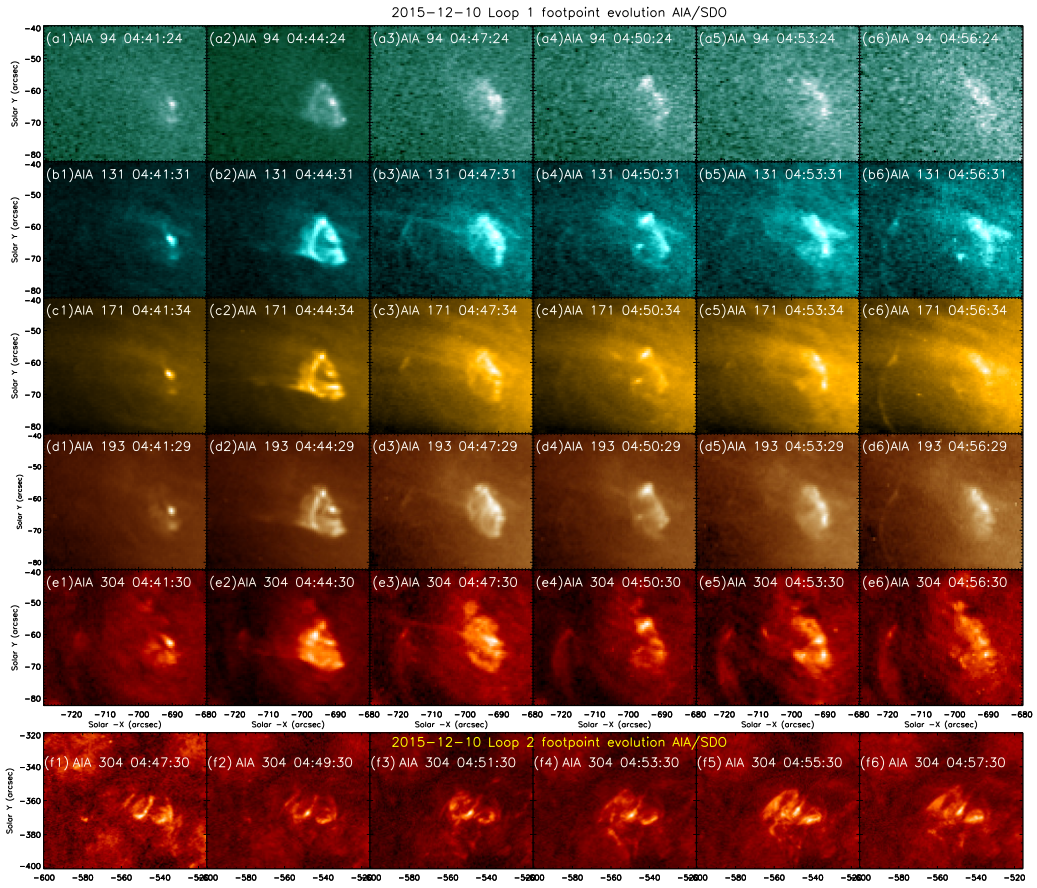

FIGURE 4.15: Panels (a1-e6) display the time evolution of the loop footpoint for the event on 10^{th} December, 2015 in five EUV channels during the flare time. Panels (f1-f6) show the same but for footpoint of loop2.

footpoint. Snapshots of the footpoint, for the loop2, are shown in panels (f1-f6). In this case, we do not see a clear jet spine structure like the previous events though we see multiple 'mini-loops' at the footpoint similar to the other events. Figure 4.16 shows the temporal evolution of the footpoint intensities for both the loops. Panel (a) of Figure 4.16 highlights the yellow rectangular box chosen for the intensity evolution study of the footpoint and also highlights the artificial slit (white rectangular box) used to create the time-distance maps (shown in panels (c-g) in Figure 4.16). From the time evolution of the intensities in different AIA channels, shown in panel (b), we notice that a major peak occurs at 04:45 UT which matches with the onset of the wave propagation as seen by XRT (panel (d) in Figure 4.3). Now, from the time-distance maps (panels (c-g)) we see that

an inclined ridge appears, in all the AIA channel, co-temporally with the intensity peak. The speeds of propagation, as measured from the slope of the ridges, range between 127-157 km sec^{-1}. We have also overplotted the HMI LOS magnetic field contours ($\pm$30 G) in panel (a). We see the presence of both positive and negative polarities within the yellow box but the dioplar structure is not clearly visible. For the footpoint of loop2 (panel (h)), we do not see any clear jet or spine structure but the footpoint evolution of the intensities, in all the channels, shows a peak at 04:27 UT which again matches with the onset of the wave propagation seen from XRT (panel (b) in Figure 4.3). We could not use the GOES data in this case due to the presence of multiple active regions and other co-temporal events occurring on the disc (close to the event location).

In summary, we see that a micro-flare at one of the footpoints of the loops, acts as a trigger for the slow waves. The micro-flare originally ejects a plasma which, as soon as it becomes detached from the source, evolves as a wave packet and exhibits slow wave properties. We test our idea of such flare generating the slow waves in our numerical model (described in next section) by injecting heat equivalent to such flare energy at one of the loop footpoint.

4.6 Numerical Experiment

4.6.1 The setup

From the observations we obtained an estimate about the speed of the wave propagating through the loop. The the density and temperature values of the loop plasma are also calculated using DEM analysis using the AIA data. Now we use a numerical simulation with the obtained loop length, density and temperature as the input parameters, to model the observations. Our simulation uses a

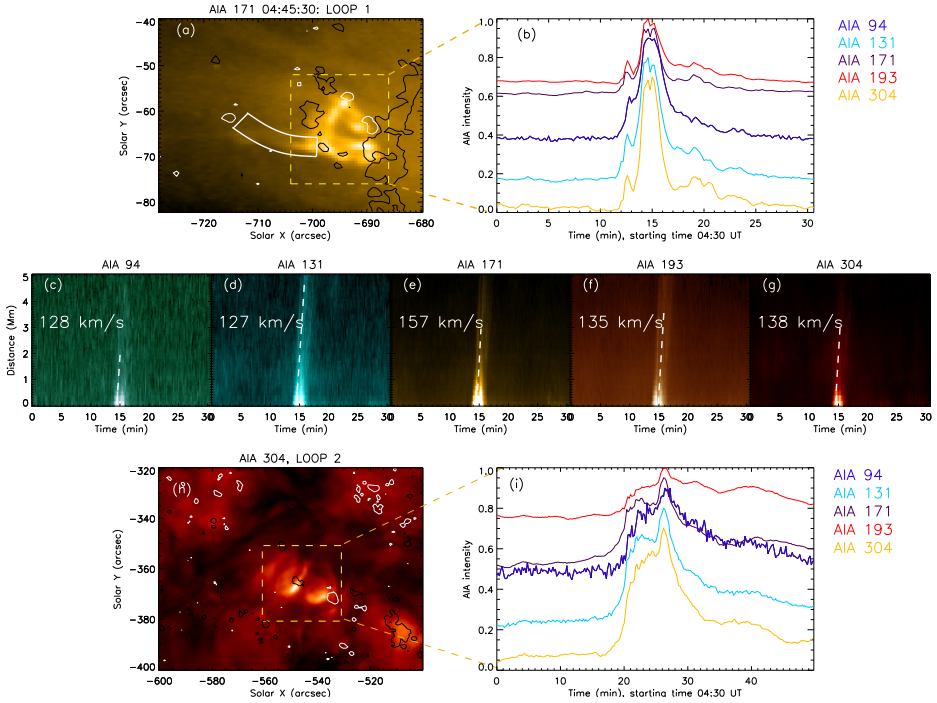

FIGURE 4.16: Panel (a) shows the snapshot of the loop1 footpoint in AIA 171 Å channel. The yellow box highlights the region used to calculate the footpoint intensity evolution in five AIA EUV channels as shown in panel (b). The white rectangular box in panel (a) marks the artificial slit used in creating time distance maps (panel (c-g)). Panel (h) shows the footpoint of the loop2 and the corresponding intensity evolution (within the yellow box) is presented in panel (i). The black and white contours in panel (a) and (h) represent the negative and positive polarities of the LOS magnetic fields (±30G) as obtained from HMI.

2.5D thermodynamic MHD model as in Fang *et al.* (2015) which includes gravity, anisotropic thermal conduction and radiative cooling. The box domain is defined as -60 Mm $\leq x \leq$ 60 Mm and $0 \leq y \leq$ 80 Mm. These values are chosen to obtain a comparable loop length of ≈140 Mm as estimated from our observations.

We initialize with a linear force-free magnetic field given by

$$B_x = -B_0 \cos\left(\frac{\pi x}{L_0}\right) \sin\theta_0 \exp\left(-\frac{\pi y \sin\theta_0}{L_0}\right) ,$$

$$B_y = B_0 \sin\left(\frac{\pi x}{L_0}\right) \exp\left(-\frac{\pi y \sin\theta_0}{L_0}\right) ,$$

$$B_z = -B_0 \cos\left(\frac{\pi x}{L_0}\right) \cos\theta_0 \exp\left(-\frac{\pi y \sin\theta_0}{L_0}\right), \tag{4.2}$$

with the angle $\theta_0 = 30^\circ$ between the arcade and the neutral line ($x = 0, y = 0$) and the horizontal size of our domain setting $L_0 = 120$ Mm (-60 Mm $\leq x \leq$ 60 Mm) and we take $B_0 = 50$ G. We set the temperature below a height of 2.7 Mm as a uniform 10,000 K for the initial thermal structure. The distribution of initial density is calculated based the assumption that a hydrostatic equilibrium with a number density of 1.2×10^{15} cm^{-3} lies at the bottom of the simulation box. We assume the initial setup with a background heating rate which decays exponentially with height for approaching a self-consistent thermally structured corona, $H_0 = c_0 \exp\left(-\frac{y}{\lambda_0}\right)$ where $c_0 = 10^{-4}$ erg cm^{-3} s^{-1} and $\lambda_0 = 80$ Mm. This heating is used to balance the radiative losses and anisotropic heat conduction related losses of the corona in its equilibrium state. With this initial setup, we integrate the governing MHD equations until the above configuration reaches a quasi-equilibrium state, when we reset time to zero.

We use the MPI-parallelized Adaptive Mesh Refinement Versatile Advection Code MPI − AMRVAC (Keppens *et al.* 2012; Porth *et al.* 2014) to run the simulation. Inorder to mimic the flare like scenario, we use a finite duration heat pulse H_1 located at the right footpoint and the form of the pulse is governed by:

$$H_1 = c_1 \exp(-(y - y_c)^2/\lambda^2) f(t) \quad \text{if} \quad A(x_1, 0) < A(x, y) < A(x_2, 0) \tag{4.3}$$

$$A(x, y) = \frac{B_0 L_0}{\pi} \cos\left(\frac{\pi x}{L_0}\right) \exp\left(-\frac{\pi y \sin\theta_0}{L_0}\right), \tag{4.4}$$

$$f(t) = \begin{cases} t/30 & 0 \leq t < 30 \quad \text{s} \\ 1 & 30 \leq t < 150 \quad \text{s} \\ (180 - t)/30 & 150 \leq t < 180 \quad \text{s} \end{cases} \tag{4.5}$$

where $\lambda^2 = 10$ Mm^2, $x_1 = 40$ Mm, $y_c = 3$ Mm and $x_2 = 39$ Mm.

Since flares are only a transient event, we allow the pulse to be switched on only

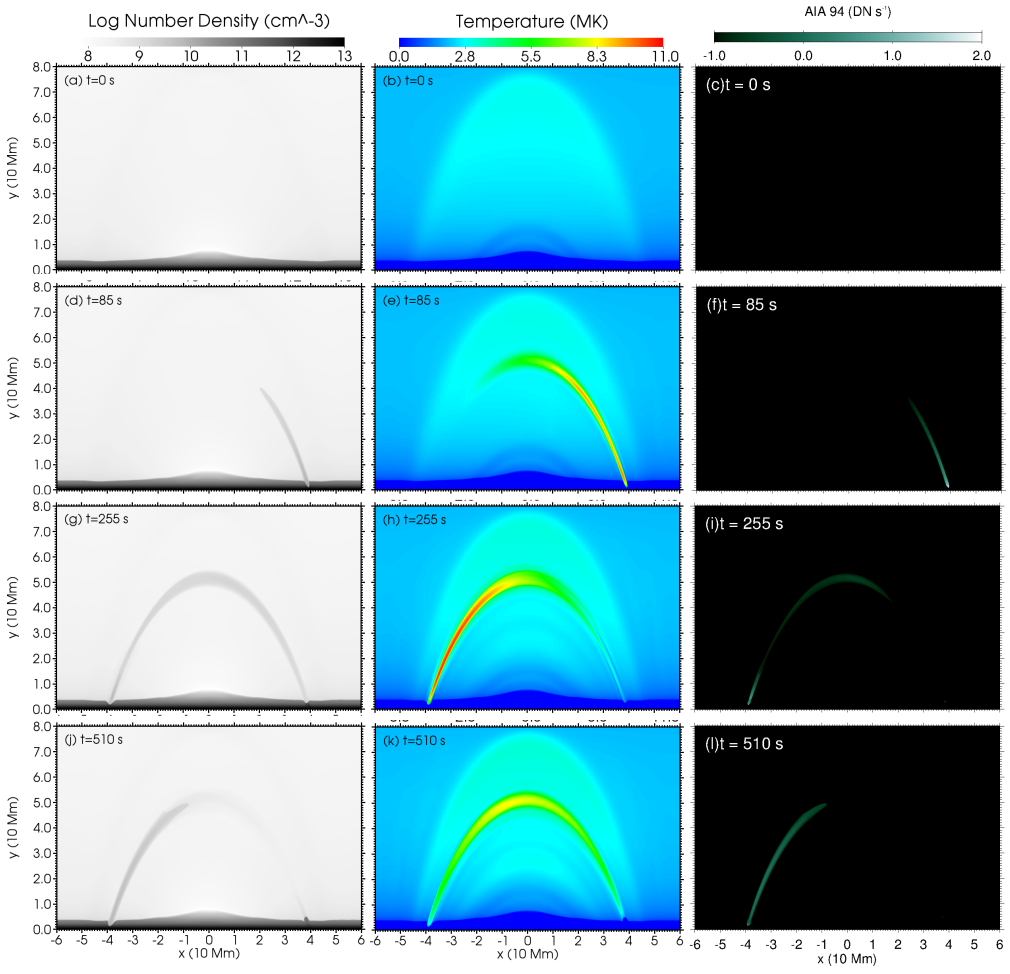

FIGURE 4.17: Snapshots showing the density (n_e), temperature (T) and the AIA 94 Å intensity images respectively at different time of the simulation. An animated version is also available online.

for a time $t = 0$ to $t = 180$ seconds. we set the c_1 to 12 erg cm^{-3} s^{-1} in our simulation input. To damp the disturbances, we introduced anisotropic thermal conduction along the magnetic field lines specified by the Spitzer conductivity $\kappa_{||}$ defined as $10^{-6}T^{5/2}$ erg cm^{-1} s $^{-1}$ K $^{-3.5}$. Apart from thermal conduction, we also introduced radiative loss function of the form Q=1.2n$_H^2\Lambda$(T) above 10,000 K (optically thin plasma) (Colgan *et al.* 2008).

To synthesize the observational features of SDO/AIA channel we use the FoMo code* to perform forward modelling (Antolin and Van Doorsselaere 2013; Antolin

*`https://wiki.esat.kuleuven.be/FoMo/FrontPage`

et al. 2014, 2015; Yuan *et al.* 2015). Using the AIA temperature response function (Del Zanna *et al.* 2011; Boerner *et al.* 2012) the FoMo code converts the density to the intensity. We have synthesized the AIA 94 Å channel emission which has a characteristics log(T) ≈6.8 .

4.6.2 Analysis of the synthesized AIA data

Now in observations, we see that the wave propagates back and forth before fading out of the loop. A similar scenario is also seen in the synthesized data as shown in Figure 4.17.

Different panels in the figure show the temporal evolution of density, temperature and the AIA 94 Å channel intensity. In order to establish a quantitative comparison between the observed wave properties and the synthetic one, we adopt a similar procedure as of the observational data analysis. A slit, tracing the loop, is drawn to extract the time distance map as shown in Figure 4.18-b. The propagation speeds, as calculated from this time-distance map, are 499 km s^{-1} (line A) and 357 km s^{-1} (line B). We must highlight here that consistency of these speed values with the observed values, validate our result obtained from DEM analysis which shows a temperature ≈ 10MK.

To estimate the damping of the observed propagating intensity disturbance, we take the time evolution of the intensity profile averaged over a chosen box (shown as yellow rectangle in Figure 4.18.a) and we fit the function (Equation 4.1) on that profile and obtained the best fit curve, shown as the red dotted line in bottom panel of Figure 4.18. The period and the damping times are 10.1 minutes and 10.3 minutes respectively. These values are comparable with the values obtained for the event on 10^{th} December.

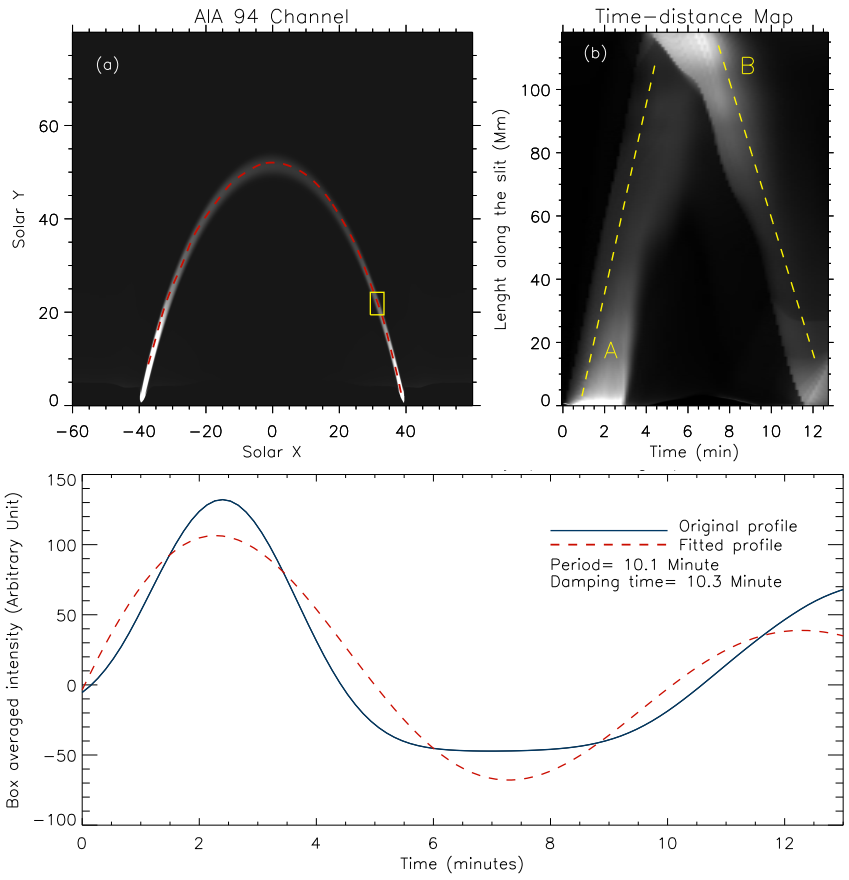

FIGURE 4.18: *Top row* : Panel (a) shows the time averaged synthesized AIA 94 Å intensity image. The red dashed line indicates the artificial slit used for constructing the time-distance map which is shown in panel (b). *Bottom row* : Panel shows the intensity evolution (averaged over the yellow box in panel (a)) over the time.

4.7 Summary and conclusion

We report, for the first time, simultaneous observation of propagating and reflecting intensity disturbance in a hot coronal loop as seen with HINODE/XRT and SDO/AIA. We also report three other cases of such reflections of the propagating disturbances from XRT. Analysis of the events shows that the observed waves appear after a micro-flare occurs at one of the loop footpoints. The DEM analysis performed on the AIA image sequence revealed that the loop temperature and

density to be 10 MK and $\approx 10^9$ cm^{-3} respectively. The average speed of propagation, as estimated from the time-distance maps, is lower than or comparable to the sound speed of the local medium estimated from the DEM analysis. This classifies the wave to be a slow propagating mode. We have studied in depth about the generation mechanism of such waves and also propose a scenario where a rapidly heated chromospheric plasma acts as a source for the high speed flows we observed in the coronal channels.

From the base-difference images and the time-distance maps we find that the waves are subject to a very fast damping as they propagate along the loop. We have quantitatively measured the damping and found out that the damping time (1/e fall from the initial amplitude) is almost equal to the period of the wave.

We implemented these aspects in a numerical setup where the input loop parameters are the same as obtained from our observations. Injecting a small energy pulse at one of the loop footpoints which mimics the micro-flare trigger, we find a slow MHD wave propagating through the loop and gets reflected back from the other footpoint. We have introduced thermal conduction as the dominant damping factor and found that the wave actually damps very quickly as observed in the our events. Analyzing the synthesized data, we have obtained the propagation speeds which matches well with the observed speeds from XRT and AIA. Using the observed density and temperature values we have reproduced similar time period of the propagating wave from our synthesized AIA data. We also find a good match between the damping time calculated from the synthesized data with the observed damping time. The wave seem to get damped quickly as it propagates through the loop (damping time comparable to the wave period). This fast damping could only be explained by the thermal conduction acting as the major damping mechanism for the propagating slow MHD mode along with the contribution from radiative cooling. Colgan *et al.* (2008) have estimated the radiation loss from the coronal plasma using different abundance ratio and models and found that the loss due

to radiation to be $\sim 10^{-22}$ erg s^{-1} cm^3. This loss is small compared to the total energy output from the flare which is $\sim 10^{28}$ erg s^{-1}.

In conclusion we have identified and studied a set of unique events from HINODE/XRT (and SDO/AIA) where a micro-flare excites a slow MHD wave in a hot coronal loop and the wave gets reflected from other footpoint before fading away. Further study with simultaneous imaging and spectroscopic data where we can quantify the changes in the time evolution of the line parameters and their relation to the observed brightening will greatly improve our understanding about the origin as well as the propagation properties of such phenomena.

Chapter 5

Forward Modelling of Propagating Slow Waves in Coronal Loops and Their Frequency-Dependent Damping.[†]

Slow waves are often used for seismological studies (King *et al.* 2003; Wang *et al.* 2009b; Van Doorsselaere *et al.* 2011; Yuan and Nakariakov 2012). These waves also get damped as they propagate along the magnetic structures. Damping of slow waves has been studied intensively from observations as well as theoretical modelling (Ofman and Wang 2002; De Moortel and Hood 2003, 2004; De Moortel *et al.* 2004; Selwa *et al.* 2005; Voitenko *et al.* 2005; Krishna Prasad *et al.* 2014; Gupta 2014; Banerjee and Krishna Prasad 2016a). Using boundary driven oscillations and including thermal conduction and viscosity as the damping mechanisms De Moortel and Hood (2003) found the thermal conduction to be the dominant

[†]Results of this work are published in Mandal *et al.* (2016a).

All the animations that are referred to in this chapter are available at `https://doi.org/10.3847/0004-637X/820/1/13`

mechanism for damping of propagating slow waves in typical coronal condition and these results match very well with the observed damping lengths from TRACE observations. The contributions of gravitational stratification, field line divergence (De Moortel and Hood 2004) and the mode coupling (De Moortel *et al.* 2004) on the wave damping are negligible compared to the damping due to thermal conduction. The dependence of the damping lengths with the observed periods have also been studied in the past. Propagating slow waves with different periodicities are detected up to different heights in the solar atmosphere and thus it indicates a frequency dependent damping mechanism operating on these waves (Krishna Prasad *et al.* 2012a). Using observational data from SDO/AIA, Krishna Prasad *et al.* (2014) investigated the frequency dependent damping of the propagating slow waves in on-disk sunspot loops as well as polar plume-interplume structures. In the low thermal conduction limit, the theory predicts a slope of 2 in the log-log plot of damping length versus the wave period but these authors found a small positive slope (less than 2) for the on-disk structures and even negative slopes for the polar structures. They concluded that the deviations of these slope values indicate some missing element in the damping theory and may point towards the existence (or dominance) of a different damping mechanism, other than thermal conduction, operating in these structures. Studying the slow waves in a polar coronal hole, Gupta (2014) found a frequency dependent damping behavior for which the lower-frequency waves can travel to greater heights whereas the higher-frequency waves are damped heavily. The author also found that the wave is getting damped heavily within the first 10 Mm and after that damping affects the waves slowly with height.

The forward modelling technique has been used previously to study various phenomena in the solar corona (De Moortel and Bradshaw (2008); Antolin *et al.* (2014, 2015); Yuan *et al.* (2015) and references within). De Moortel and Bradshaw (2008) studied the intensity perturbations using the forward modelling in a long coronal loop. They synthesized the SOHO/TRACE 171Å and the HINODE/EIS 195Å line

and found that the observed intensity perturbation need not necessarily follow the model density and temperature. The discrepancy comes because of nonlinear interaction between the density, ionization balance and the instrumental response function. This shows the necessity of the forward modelling when comparing the numerical model results with the real observation.

In this work we set out to explain the discrepancies between the observed and theoretical values of the slope in a log-log plot of the damping length versus period. We present a 3-D numerical loop model with constant density and temperature along the loop length and implemented anisotropic thermal conduction as the damping mechanism. In our model we have not included the gravitational stratification and the flux tube divergence as they have no contributions towards the frequency dependent damping length (see Table 1 in Krishna Prasad *et al.* (2014)). We have used forward modelling to generate synthesized SDO/AIA images from our numerical model output. The forward modelling technique converts the model output parameter (e.g density) into observable (e.g intensity) with the use of the instrumental filter response function. Thus the synthesized images contain information about the MHD wave theory as well as the atomic emissions as would be observed by the SDO/AIA. Here we want to emphasize the fact that we use a 3-D model to fully exploit the advantage of forward modelling (which takes into account the effects due to LoS angle, column depth and pixel size (Cooper *et al.* 2003)) to create synthesized images which allow us to compare our results immediately with the observation which was not possible with the previously mentioned 1-D loop models.

5.1 Numerical Model

Our 3D numerical model consists of a straight, density enhanced flux tube embedded in a background plasma, the whole region being permeated by a uniform magnetic field, parallel to the flux tube (see Figure 5.1). The density varies smoothly from the interior of the flux tube to the background value, with an inhomogeneous layer (at the boundaries perpendicular to the loop length) of width $l \approx 0.1R$, for numerical stability. We neglect the effect of gravity and loop curvature. The values of relevant physical parameters are listed in Table 5.1.

In order to excite slow waves in the flux tube, we perturb the pressure at its footpoint near the boundary of the computational domain, acting only inside the flux tube and going to zero outside the loop diameter. This time-dependent pressure perturbation ($p\prime$) has the following form:

$$\frac{p'(t)}{p_0} = \text{constant} + \sum_{i=1}^{n} \alpha_i \sin\left(\frac{2\pi t}{T_i}\right), \tag{5.1}$$

where p_0 is the initial pressure, n is the number of different single-period waves, α_i is the relative amplitude of the perturbation, and T_i is the wave period. We drive the waves during the whole simulation time. Simulations were run with one ($n = 1$) and four ($n = 4$) periods. The relative amplitudes chosen for the multi-period driver are $\alpha_1 = 0.2, \alpha_2 = 0.203, \alpha_3 = 0.206, \alpha_4 = 0.21$, while for the single-period driver, $\alpha_1 = 0.2$. The corresponding wave periods are $T_1 = 3$ min, $T_2 = 5$ min, $T_3 = 7$ min, $T_4 = 10$ min and $T_1 = 3$ min. At this (bottom) boundary, we have reflective boundary conditions for the velocity, and zero-gradient for the other variables. At the top end of the flux tube, we apply open (or zero-gradient) boundary conditions, letting the waves leave the domain, though producing minor reflections. The other perpendicular boundaries are periodic. Note that the tube length for the multi-period runs is longer than that of the single-period runs, in

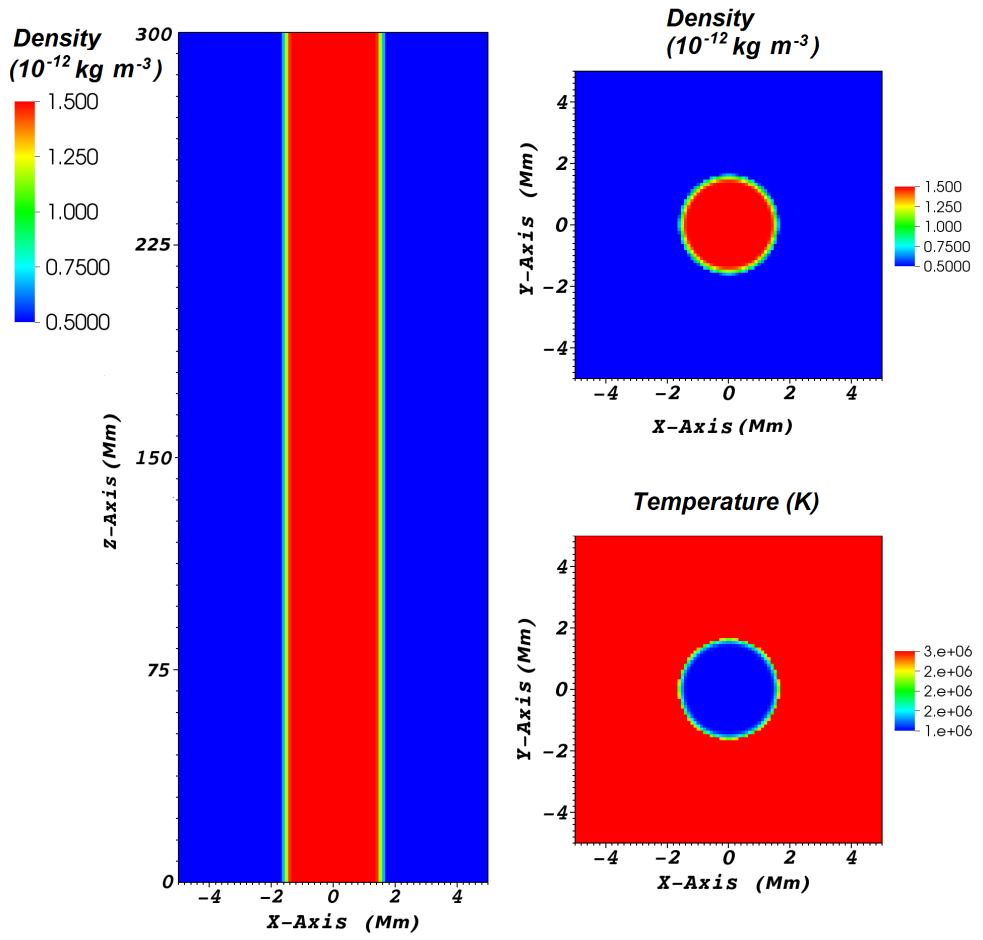

FIGURE 5.1: Plot showing the initial condition: slice along the tube (left) and cross-section (right) showing the density (left, upper right) and temperature (lower right). The spatial dimension of the numerical domain is 10 Mm × 10 Mm × 300 Mm (for the multi-period runs).

order to accommodate three wavelengths of the longest period wave (T_4). This is necessary in order to get a reliable fit to the damped amplitudes in the analysis to follow.

The MHD problem is solved numerically, using `MPI-AMRVAC` (Keppens *et al.* 2012; Porth *et al.* 2014) using HLL solver . The uniform grid consists of 96 × 96 × 600 numerical cells, enough to eliminate the damping of the oscillations due to numerical dissipation, as test runs have shown. We include anisotropic thermal conduction, i.e. along the magnetic field lines, with the Spitzer conductivity set to

TABLE 5.1: The values of relevant physical parameters used in the simulations.

Parameter	*Value*
Tube length (multi-period run) (L)	300 Mm
Tube length (single-period run) (L)	100 Mm
Tube radius (R)	1.5 Mm
Magnetic Field	12.5 G
Tube density ($\rho_{\rm inside}$)	$1.5 \cdot 10^{-12}$ kg/m^3
Density ratio ($\rho_{\rm inside}/\rho_{\rm outside}$)	3
Tube temperature	1.0 MK
Background plasma temperature	3.0 MK
Plasma β	0.04

$\kappa = 10^{-6}\, T^{5/2}$ erg cm^{-1} s^{-1} K^{-1}, where T is the temperature (see Van Doorsselaere *et al.* (2011); Xia *et al.* (2012)).

5.2 Synthesizing AIA observation

We synthesize imaging observations in the SDO/AIA 171 Å ($\approx$ 0.6MK) and 193 Å ($\approx$ 1.2MK) bandpasses, within which the 1MK loop could be prominently detected. We use the FoMo code* to perform forward modelling. It has been used for forward modelling by Antolin and Van Doorsselaere (2013); Antolin *et al.* (2014, 2015); Yuan *et al.* (2015). The FoMo code uses the AIA temperature response function (Del Zanna *et al.* 2011; Boerner *et al.* 2012) and performs numerical integration along selected LOS angles (see details in Yuan *et al.* 2015). We obtain synthetic AIA observation along LOS angles at 30 deg and 90 deg (see Figure5.2) for both bandpasses. The output image data are coarsened to AIA pixel size (0.6") while in the numerical LOS integrations of the emission, the discretization

*`https://wiki.esat.kuleuven.be/FoMo/FrontPage`

has a slightly better resolution than the numerical simulation. The time interval between two successive synthesized AIA images is 23 seconds.

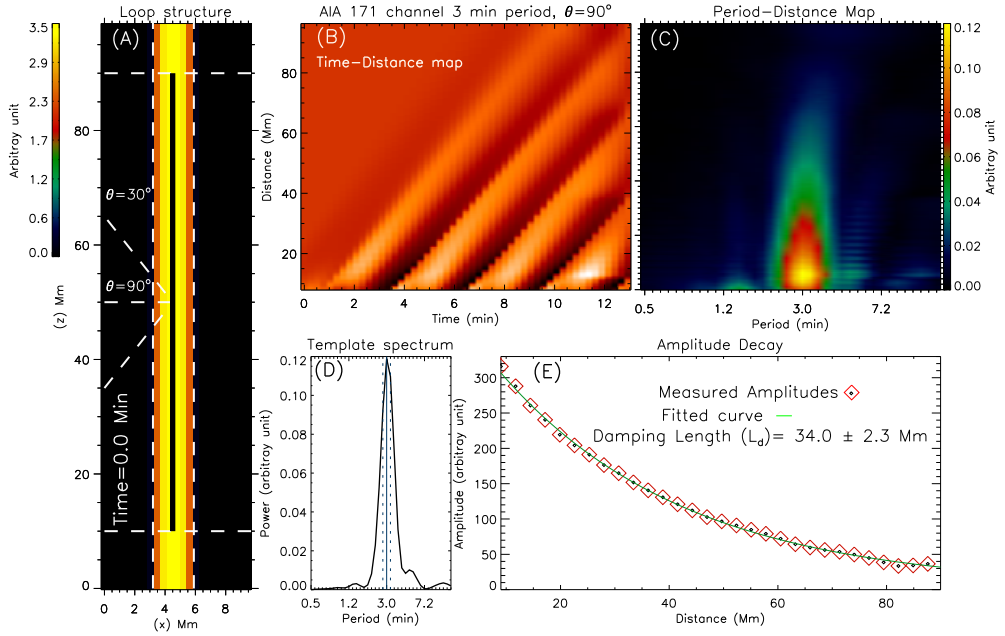

FIGURE 5.2: (A) : The initial intensity snapshot for AIA 171 Å channel for θ= 90. Two horizontal white dashed line indicate the region of the loop selected for the analysis. The LOS angles (θ) are also marked in the panel (B) : Time-distance plot produced from AIA 171Å image sequence by placing an artificial slit marked by a black vertical line in panel-A. (C) and (D) : corresponding period-distance map and the template spectrum (made from bottom 5 pixels of panel-c) using the time-distance map. (E) : The amplitude decay plotted with the distance along the loop length. The damping length obtained from a fitted exponential function is printed on the plot.

5.3 Analysis of the model output

5.3.1 Single-period driver

The initial intensity image (before switching on the driver) for the AIA 171 Å channel is shown in panel-A of Figure 5.2.

In the analysis, we choose our region of interest along the length of the loop leaving ≈10 Mm, from each side of the loop-footpoints, to avoid any kind of boundary effects (shown as horizontal white dashed lines in panel-A). In this paper, we followed a similar approach as used by Krishna Prasad *et al.* (2014). To generate a slow wave with a period of 3 minutes, we implement a continuous driver of the same period situated at one of the loop footpoint. From the movie (movie 1, available online) we see that the waves, propagating from one footpoint to the other, are getting damped as they move along the length of the loop. This property is clearly visible in the time-distance map which we construct by placing an artificial slit of thickness 1 Mm along the length of the loop, shown as a black thick line in panel-A. To construct an enhanced time-distance map (panel-B), we have subtracted a 15 points (i.e time frames) running difference from the original map to remove the background.

To analyze the propagation of the power along the distance of the loop, we convert the time-distance map into a period-distance map. We use the wavelet transform (Torrence and Compo 1998) on the time series at each spatial pixel on the time-distance map to obtain the period-distance map. As shown in panel-C of Figure 5.2, we notice that the power is concentrated only around the 3 minute period (expected as the driver period is 3 minutes) and the fact that the power decreases as we move along the length of the loop. The power distribution as function of the period is plotted in panel-D. This template spectrum is obtained using the bottom 5 pixels of the period distance map. To obtain a trend of the power decrement, we follow the amplitude (which is the square root of power) along the 3 minute period (within the width, as shown in dotted lines in panel-D, obtained from a SolarSoft routine *gt_peaks*.pro) and plot them with the distance of the loop. We plot every 15^{th} point in the panel to avoid crowding of points. The amplitude decay is then fitted with an exponential function of the form $A(y) = A_0 e^{-y/L_d} + C$ where L_d is the damping length of that period. The obtained damping length is equal to 34.0±2.3 Mm.

5.3.2 Multi-period Driver

In real observations we find a range of frequencies which are present simultaneously in the coronal loops. To mimic this situation, we choose four periods (3,5,7 and 10 minutes) which are being generated all together by a driver acting at one of the loop footpoints. Keeping the wavelength for the longest period in our simulation (which is 100 Mm for the 10 minute period), we choose a loop length of 300 Mm as shown in the upper panel in Figure 5.3. The first and last ≈ 18 Mm is left out of the analysis to avoid boundary effects. A rectangular box along the length

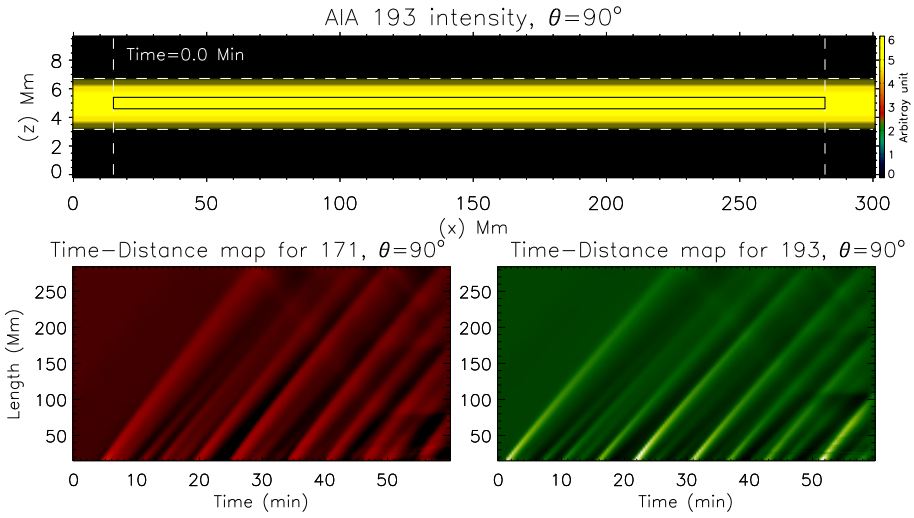

FIGURE 5.3: *Top panel* : Initial intensity image for AIA 193Å channel for θ=90. The Black rectangular box indicates the artificial slit used to create the time-distance maps. *Bottom panel* : Time-distance maps, for the multiperiod driver (3,5,7 and 10 minutes), are shown for AIA 171Å and 193Å channel respectively. The inclined ridges indicate the propagating slow waves through the loop.

of the loop, shown in black in upper panel of Figure 5.3, is chosen to construct the time distance plot as before. The time-distance maps for two AIA channel 171 Å and 193 Å for a line of sight (LOS) angle θ = 90 is shown in bottom panels in Figure 5.3. From these maps, we see different periodicities in the appearances of the inclined ridges in both the channels. We also notice that in these maps, faint reflections generated from the other footpoint are also present. The amplitudes

of these reflections are less than 1% of the input wave amplitudes. Hence, it has negligible effect in the results we produce using these maps.

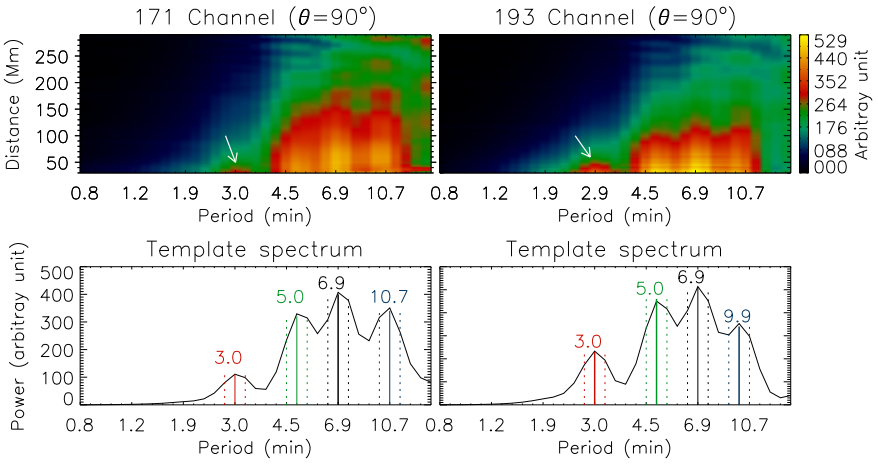

FIGURE 5.4: *Top* : The power-distance maps generated from the time-distance maps of the two AIA channels (171 Å and 193 Å). The white arrow in each panel points to the 3 minute power. *Bottom* : Template spectrum for AIA 193 Å and AIA 171 Å channels respectively. Detected periods (solid lines) are printed on the panels along with their widths (dotted lines) obtained by using *gt_peaks*.pro.

In Figure 5.4 we show the power-distance maps (upper panels) and their corresponding template spectrum for the 171 Å and 193 Å channel. These power-distance maps act as a tool to separate out the powers confined in different periods and their decay with the distance along the loop. Four distinct periods can clearly be identified from the template spectrum. The slight departure of the detected periods from the given period values in the simulation, can be attributed to the period resolution of the wavelet analysis. All the peaks and their widths in the template spectrum have been identified by the *gt_peaks*.pro routine. Similar to the single period analysis, we follow the amplitude of a particular period (within the corresponding width) along the distance in the power-distance map. In Figure 5.5 we plot the amplitude decay for each detected period for the AIA 171Å and 193Å channels. Here also we plot every alternate 30^{th} point to avoid crowding in the amplitude decay plot. The solid lines are the fitted exponential decay function, as described in the previous section and the obtained damping length (L_d)

from the fitted curve, along with the error, is printed in each panel. We notice from the figure that the damping lengths, in the two AIA channels, are different for the waves with same periods. The difference can be attributed to the different responses of the AIA filters.

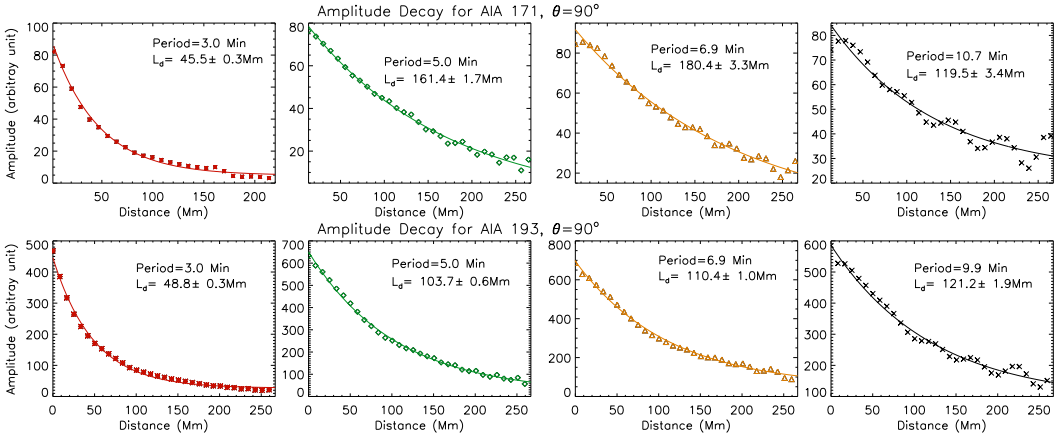

FIGURE 5.5: *Top* : Amplitude decay (symbols) of the detected periods for the AIA 171 Å channel for θ=90. The fitted exponential function is overplotted as the solid lines. The damping length obtained from the fitting, along with the errors, is printed in each panel. *Bottom* : Same as previous but for the AIA 193 Å channel for θ=90.

We perform the same analysis for another LOS angle, $\theta = 30$ for 171 Å and 193 Å channel. The damping lengths obtained from each period, in this case, are listed in Table 5.2. As we are more interested in the change in damping length with the change of period to obtain a frequency/period dependence of the slow waves, we draw a log-log period versus damping length plot (Figure 5.6) for two AIA channels for two LOS angles.

Each panel in Figure 5.6 shows the obtained damping length and the corresponding period in logarithmic scales. Slope values, obtained by fitting a linear function to the data, are printed in each panel. We find the slopes to be positive in all the cases and its value ranges from $\approx +0.8$ to $+1.4$ (with errors less than 0.7). These values match well with the values Krishna Prasad *et al.* (2014) found for the sunspot loops. It is worth mentioning that the parameters we have used in our simulation mostly mimic the coronal sunspot loops rather than the polar plumes

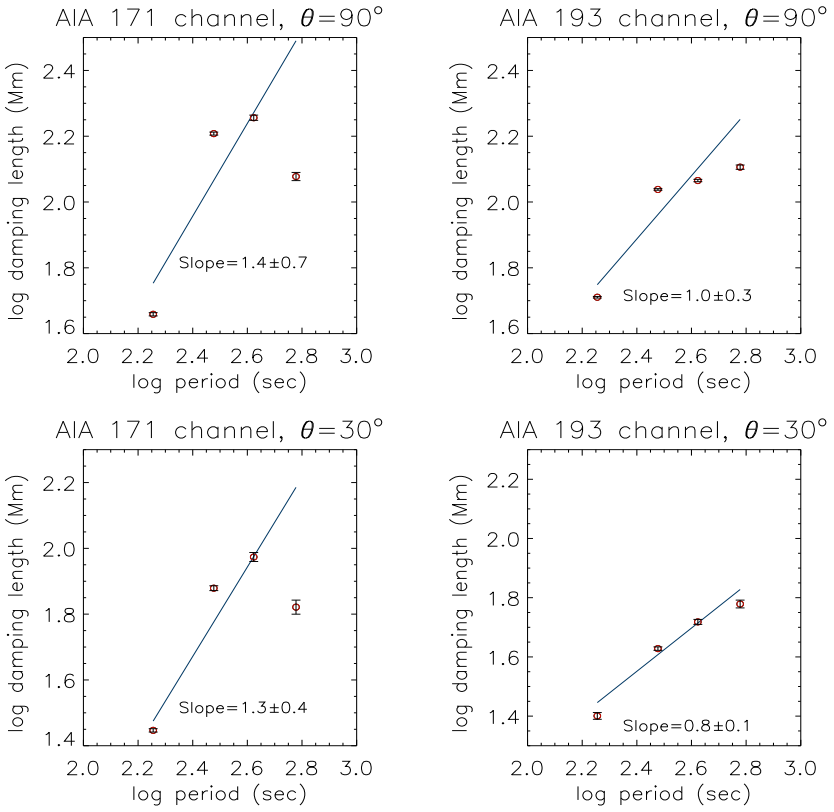

FIGURE 5.6: The log-log plot of period versus damping length for the two LOS (30 and 90) for AIA channels 171 Å and 193 Å. The slope of the fitted straight line is printed in each panel along with the error bars.

and interplume regions which have different physical conditions than the sunspot loops.

5.4 Analysis of density evolution

De Moortel and Bradshaw (2008) showed that the observed intensity perturbation may not necessarily follow the model density and temperature. To investigate this behaviour, we used the density values, from the simulation and repeated the analysis as above to obtain the log-log period versus damping length plot (Fig. 5.7). The panel (*a*) in Figure 5.7 shows the time-distance map from the density values obtained by placing an artificial slit along (x=0,y=0), i.e. the centre of the

TABLE 5.2: Damping Lengths obtained for $\theta = 30$

AIA Channel	*Period* (*Min*)	*Damping Length* (*Mm*)
171 Å	3.0	27.9± 0.3
	5.0	75.6± 0.7
	6.9	94.1± 1.2
	10.7	66.2±1.3
193 Å	3.0	25.1± 0.3
	5.0	42.5± 0.5
	6.9	52.3± 0.5
	9.8	60.1± 0.7

loop. The damping lengths obtained are 86, 155, 158 and 219 Mm (with errors within 1 Mm) for the periods 3, 5, 7, and 10 minutes respectively. Using these damping lengths we obtain a log-log plot of the period versus damping length which has a slope of 0.9±0.2 . This value is very much consistent with the slope obtained using intensity values. We want to remind the reader that these density values are from the simulation (before the use of FoMo code) and the consistency of this result with the result using the intensity values shows that the emission details are not so important for analyzing the power law behaviour for these waves.

5.5 Theory

In this study, we consider only the thermal conduction as the slow wave amplitude damping mechanism. Applying a perturbation of the form $\exp[i(\omega t - kz)]$ on the linearized MHD equations we get the following dispersion relation for the slow waves (Krishna Prasad *et al.* 2014)

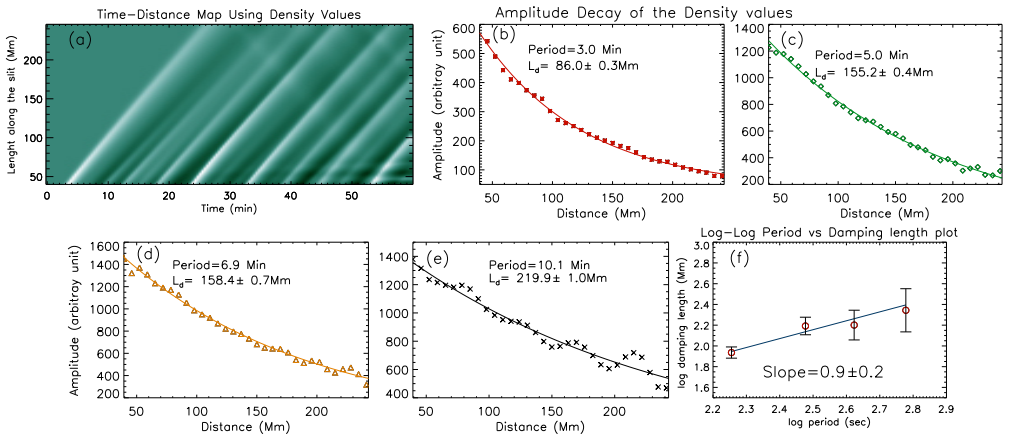

FIGURE 5.7: (a) : Time-distance map from the density values created using an artificial slit located at loop center, $(b)-(e)$: Amplitude decay for each detected period along with the fitted function. Obtained damping lengths are printed in each panel, (f) : The log-log period versus damping length plot. Obtained slope (along with the error) is printed in the panel.

$$\omega^3 - i\gamma d k^2 \omega^2 c_s^2 - \omega k^2 c_s^2 + i d k^4 c_s^4 = 0, \tag{5.2}$$

where ω is the angular frequency, γ is the adiabatic index and c_s is the adiabatic sound speed and d the thermal conduction parameter defined as $d = \dfrac{(\gamma-1)\kappa_{\parallel} T_0}{\gamma c_s^2 p_0}$, which has contributions from the equilibrium values of pressure (p_0), density(ρ_0), temperature (T_0) and also from the conductivity $(\kappa_{\parallel})$ which is parallel to the magnetic field. The damping length (L_d) is derived as the reciprocal of the imaginary part of the wave number k.

Equation 5.2 is a bi-quadratic equation for k. We have thus solved it analytically for k^2 and only retained the solution with the minus sign (corresponding to the solution in Eq. 5.3). Then k was computed as the square root of the complex k^2 and the imaginary part of this was taken as the reciprocal of the damping length L_d. To obtain the frequency dependence of L_d we solved the equation for different periods (within the range 3 to 13 minutes) with the parameters we have used in the simulation and plotted the log-log plot in Figure 5.8 (+ symbols).

We also consider the lower thermal conduction limit ($d\omega \ll 1$)) of the Eq. 5.2 and the equation reduces to

$$k = \frac{\omega}{c_s} - i\frac{d\omega^2}{2c_s}(\gamma - 1) \tag{5.3}$$

The damping length, under this assumption, is $\propto 1/\omega^2$. Solutions of the above equation (Eq.5.3) for periods ranging from 3 to 13 minutes are shown by ($*$) symbols in Figure 5.8. The fitted straight line to these points is shown as a red solid line in Figure 5.8.

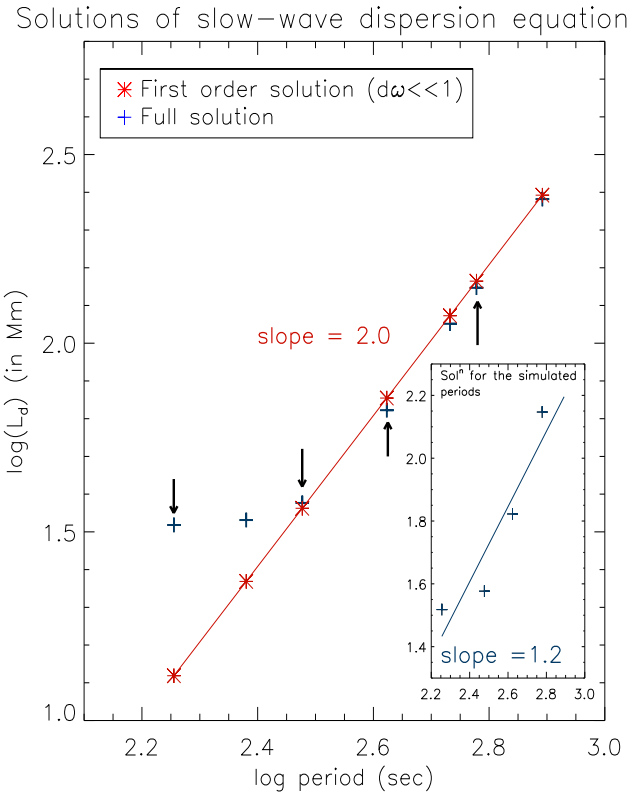

FIGURE 5.8: Log-log plot of damping lengths obtained by solving the Equation 5.2 for a range of periods (3 to 13 minutes). The red ($*$) represent first order solutions corresponding to the lower thermal conduction limit ($d\omega \ll 1$) whereas the blue ($+$) symbols represent the full solutions. The obtained slope for the first order solutions (represented by a red line) is equal to 2 whereas the slope for the full solutions for the frequencies used in the simulation, is equal to 1.2 (as shown in the blue line in the inset plot).

From the figure we see that the full and the lower thermal condition limit approximated solutions follow each other very closely for higher periods. For the periods below 5 minutes, the two solutions deviate from each other significantly resulting in a slope less than 2. The dω values, for the periods used in our simulation (3,5,7,10 minutes), are 1.07, 0.64, 0.45, 0.32 respectively. So we see that the 'small thermal conduction limit' (d$\omega \ll 1$) is not valid for smaller periods.

We also highlight the periods we used for our simulation by the black arrows. To get the power dependence from the theory we fit the full solutions only for the periods used in the simulation and fitted a straight line to these points as shown in the inset in Figure 5.8. The slope measured is equal to 1.2 which is very close to our measured mean value 1.1 .

Following the same approach as above, we drew a log-log plot of the period versus damping length and fit a linear function to obtain a power law index. We obtained a slope of 1.4±0.7 (171Å channel) and 1.0±0.3 (193Å channel) for $\theta = 90$ and 1.3±0.4 (171Å channel) and 0.8±0.1 (193Å channel) for $\theta = 30$. We conclude from these values that the wave is getting damped linearly with change of period. Furthermore, to see the effect of the emissivity and the instrumental responses on the power law index, we have used the density values obtained from the simulation. The identical slope values indicate that these factors are not important in these studies.

5.6 Summary and Conclusion

In this study, we set out to explain the observed dependence of the damping of slow waves with their period. In the previous work, no theoretical prediction for damping dependence could explain the observed values. Here we aimed to simulate

the damping, perform forward modelling and analyze the model output as in the observations in order to explain the unexpected damping length behaviour with the wave period.

In our current study, we first simulated a long coronal loop with a singe period continuous driver at the bottom of the loop footpoint to generate the slow waves. We allowed the waves to decay by applying thermal conduction along the length of the loop. We followed the amplitude of the period along the loop length and fitted an exponentially decaying function to obtain the damping length. In the next phase, we replaced the single period driver with a continuous multiperiod driver.

We have also studied in-depth the theoretical damping behaviour of the slow waves in the case when thermal conduction is not weak. Using linear theory and including thermal conduction as the dominant damping mechanism, one would obtain a slope of 2 in a log-log period versus damping length plot (Krishna Prasad *et al.* 2014). We have found that in the general case (and not the weak conduction limit previously used) a similar positive slope, as in the observation, can be reproduced. This shows that the 'lower thermal conduction limit' ($\mathrm{d}\omega \ll 1$) assumption is not valid for lower periods which in terms shifts the slope towards lower positive value than the theoretically predicted value of 2.

On the other hand the negative slopes for polar plume and the interplume case obtained by Krishna Prasad *et al.* (2014) are still to be explained. They are possibly due to different nature of the polar plumes compared to the sunspot loops. The density and temperature structures in plumes are different from sunspot loops and change very rapidly with the height from the plume footpoint (Wilhelm 2006). We have not considered any magnetic field divergence, density stratification in our loop model, and thus the negative slopes may indicate a different dominant damping source other than the thermal conduction.

Chapter 6

A statistical study on the frequency-dependent damping of slow-mode waves in polar plumes and interplumes[†]

6.1 Introduction

Slow magnetoacoustic waves (or simply, slow waves) are compressible magnetohydrodynamic (MHD) waves which typically propagate along the magnetic field lines in solar corona (Roberts 2000). These waves are found in a variety of structures across different layers of the solar atmosphere (Banerjee *et al.* 2007). However, in this paper, we are only interested in the coronal counterpart of these waves as seen in large-scale coronal structures such as polar plumes (Banerjee and Krishna

[†]Results of this work are published in Mandal *et al.* (2018).

All the animations that are referred to in this chapter are available at `https://doi.org/10.3847/1538-4357/aaa1a3`

Prasad 2016b). Polar plumes are the long and thin 'ray' like structures which trace open magnetic field lines emerging from the unipolar coronal hole regions (Poletto 2015). One of the first detections of slow waves was reported by DeForest and Gurman (1998) where the authors had used EUV imaging data to show propagating intensity disturbances (later interpreted as slow waves) along polar plumes. These waves are ubiquitous in the solar corona (Krishna Prasad *et al.* 2012b) with their apparent speeds ranging from 50 to 150 km s^{-1} (Kiddie *et al.* 2012). Such omnipresent nature, along with easy detectability, often make these slow waves an important tool for coronal seismology (King *et al.* 2003; Van Doorsselaere *et al.* 2011).

Interestingly, these waves are subject to rapid damping while propagating along the coronal structures (Ofman and Wang 2002). This damping is primarily controlled by the thermal conduction whereas the other dissipative mechanisms such as the viscosity and the radiation loss have a little role to play (De Moortel and Hood 2003). Furthermore, the wave damping is not uniform over the entire range of periodicities. In other words, the damping of slow waves has a frequency dependence. Krishna Prasad *et al.* (2012b) showed that waves with shorter periods are restricted close to the base of the coronal features while those with longer periods propagate higher up. Gupta (2014) have found two distinct height ranges (above the solar limb) with two contrasting damping rates. The frequency-dependent damping aspects in different coronal structures (on-disk fan loops and polar plumes/interplumes) have been explicitly shown using a single observation by Krishna Prasad *et al.* (2014). The authors have demonstrated that the frequency dependence of the damping observed in the on-disk loop like structures and the polar plume/interplume regions is different and neither of the observed dependences could be successfully explained by a linear MHD wave theory. However, using 3D MHD simulations, Mandal *et al.* (2016a) have shown that the observed characteristics for the on-disk loops are still consistent with the thermal-conduction-dominated damping of slow waves. Yet, the peculiar frequency dependence found in the polar

region structures remains unexplained. The earlier conclusions of Krishna Prasad *et al.* (2014); Gupta (2014) were derived from isolated case studies based on single dataset and thus, a statistical study is needed to establish the robustness of those results.

6.2 Observation details

In this study, we used high-resolution extreme ultraviolet (EUV) imaging data from the Atmospheric Imaging Assembly (AIA) (Lemen *et al.* 2012), onboard Solar Dynamics Observatory (SDO) (Pesnell *et al.* 2012) from two different pass-bands, namely, AIA 171 Å and AIA 193 Å. We selected a total of 62 datasets, each covering about 180 minutes duration, taken over a span of seven years from 2010–2017. All the datasets have a uniform cadence of 12 s with a spatial pixel

TABLE 6.1: Details of the AIA observations

Year	No. of events	Duration/Event (min)	Cadence (s)
2010	10	180	12
2011	12	180	12
2012	04	180	12
2013	–	–	–
2014	–	–	–
2015	10	180	12
2016	15	180	12
2017	11	180	12

scale $\approx 0.6''$. Since our primary targets are polar plume/interplume structures, all of the selected data are associated with coronal holes. Consequently, the sample

do not contain any datasets observed between the end of 2012 and the end of 2014, i.e., during the maximum of current solar cycle (cycle 24). This also keeps our data free from large-scale background structures, such as streamers. Besides, all the datasets were carefully checked with the JHelioviewer tool (Mueller *et al.* 2013) to exclude the possible presence of large and small-scale jets, missing frames, etc., in the selected data.

6.3 Method

The full-disk data are first reduced to a smaller regions of interest (ROIs) of size $800'' \times 400''$ encompassing the polar region alone as shown in panel (a) of Figure 6.1. The bright plume and the dark interplume structures are then detected by following different intensity contour peaks and valleys (Krishna Prasad *et al.* 2011; Su 2014), respectively, as shown in the Figure. The methodology adopted here to track the slow waves of different periods and study their damping, is similar to that described in Krishna Prasad *et al.* (2014) and Mandal *et al.* (2016a). The overall procedure can be summarized as follows. First, we generate time-distance maps by extracting data from artificial slits placed on top of the detected plume and interplume structures. The white solid and dashed lines marked on Figure 6.1a represent these slits for plume and interplume structures, respectively. The width of each of the slits is kept uniform and wide ($\approx 20''$) to improve the signal to noise ratio in the generated time-distance maps. Figure 6.1b displays one such map obtained from slit 3, which has been further enhanced by subtracting (and then normalizing with) a background constructed from a running average of 300 frames (60 minutes) of the original data. Note that the bottom of the map corresponds to the limb. In this enhanced map, we readily identify the upwardly propagating slow waves as alternative slanted ridges. Such classification of these intensity

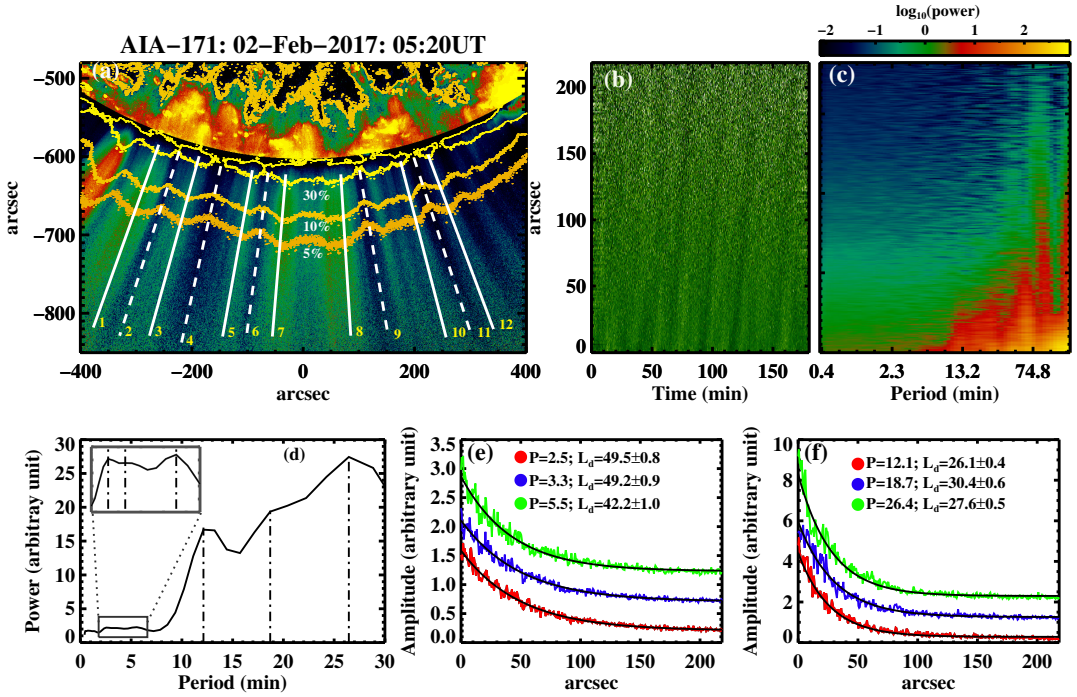

FIGURE 6.1: Methodology adopted to analyze the frequency-dependent damping in slow waves: Panel (a) shows a representative image of our ROI which has been processed using a radial filter to enhance the polar features. Overplotted yellow contours denote different intensity levels (as % of the on-disk intensity), obtained from the original image. Solid and dashed white lines represent the locations of the artificial slits used for generation of time-distance maps. An enhanced time-distance map, generated from slit 3, is shown in panel (b) whereas the corresponding period-distance map is shown in panel (c). Panel (d) displays a template power spectrum constructed from the period-distance map showing different periods present in the data. Panels (e-f) present the amplitude variation with distance for each of the detected periods. The black solid lines, in these plots, show the fitted exponential decay function to the data. The obtained damping lengths (L_d) corresponding to individual periods (P) are printed on the panels.

disturbances is primarily based upon the measurements of their (projected) phase speeds from the time-distance maps (Krishna Prasad *et al.* 2011). A closer look at this map also reveals the simultaneous existence of multiple periods. This is particularly evident near the limb where we see many closely spaced ridges (shorter periods) as compared to a far away region where only sparsely spaced ridges (longer periods) are visible.

In order to isolate the power associated with the individual periods, we convert the original time-distance maps into period-distance maps (Figure 6.1c) by using a wavelet transformation (Torrence and Compo 1998) of the time series at each spatial position. We note that the power at the longer periods is higher compared to that at the shorter periods and the power, at a given period, decreases as one moves away from the solar limb. A template power spectrum (Figure 6.1d) is constructed from the bottom 10 pixels of the period-distance map, which is used to identify the peak oscillation periods present in the data. For each detected period, the variation of the amplitude (defined as the square root of power) along the slit length is extracted as shown in Figures 6.1e and 6.1f. Considering the cadence (12 s) and the duration (180 minutes) of individual datasets, we restrict our analysis to periods between 2 and 30 minutes. As can be seen, the oscillation amplitudes decrease rapidly with the distance. To measure the amplitude decay quantitatively, we fit the data with an exponential function (shown as solid black lines in the figure) defined as $A(x) = A_0 e^{-x/L_d} + C$, where L_d is the damping length. The L_d value obtained from the fit, for each detected period, is noted. In this way, we obtained damping lengths corresponding to multiple periods detected in several plume and interplume structures across all the 62 datasets in both 171 Å and 193 Å channels.

6.4 Analysis

6.4.1 Period distribution

In Figure 6.2 we show a histogram of all the detected periods, in both plume and interplume structures observed in the two AIA passbands. The distribution is quite similar across different structures and passbands. The shorter periods (2–6 min) appear to be far more abundant than the longer periods (>7 min) which

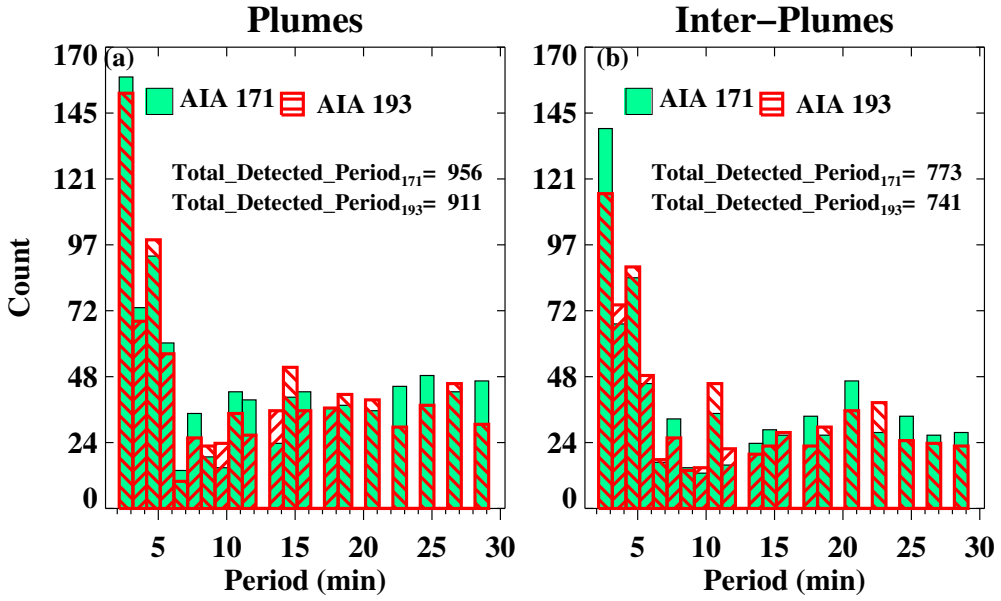

FIGURE 6.2: Distribution of the detected periods in plume (a) and interplume (b) regions. The results from the 171 Å and 193 Å passbands are shown in color-filled and cross-hatched blocks, respectively.

are more or less uniformly distributed. Although some previous studies Krishna Prasad *et al.* (2012b); Gupta (2014) reported the existence of both shorter and longer periods in the polar regions, it is generally believed that the long-period oscillations are more prevalent in these regions. So this behaviour is contradicting. Interestingly, upon carefully inspecting the detected periods from individual datasets, we found that the same set of shorter periods are observed in several plume/interplume structures whereas the longer periods observed in those structures are not necessarily the same. The latter are more or less evenly distributed across the period range between 7 and 30 min, producing such imbalance. Overall, about 41% (43%) of the detected periods in 171Å (193Å) passband are from shorter (2–6 min) periods when the data from both plume and interplume structures are combined. Since the observed oscillations are mainly due to propagating waves (the periodicity of which is determined by the source), it is possible that the shorter and the longer period oscillations are generated from a different source. For instance, the short-period oscillations could be a direct result of leakage of global p-modes (De Pontieu *et al.* 2005; Calabro *et al.* 2013; Krishna Prasad *et al.*

2015) or the chromospheric acoustic resonances (Botha *et al.* 2011) or the acoustic cutoff effect involving impulvise disturbances (Chae and Goode 2015)., while the long-period oscillations are generated from transients (like spicules) in the lower atmosphere (Jiao *et al.* 2015; Samanta *et al.* 2015). One must take these results into account while building a model (such as by Yuan *et al.* (2016)) to investigate the source of slow waves in polar regions.

6.4.2 Frequency dependence

The obtained damping lengths L_d, for all the detected periods P (see section 6.3), are shown in a log-log plot in Figure 6.3 separately for plumes and interplumes and in the two AIA channels. The grey points in these plots represent the actual values with the corresponding uncertainties. As one may notice, the damping length values appear more scattered in 193 Å passband as compared to that in 171 Å passband. This is perhaps due to the lower signal-to-noise ratio in the 193 Å passband. In fact, for a given passband, the scatter is relatively larger at longer periods.

However, it is clear that the damping lengths become progressively shorter for longer periods. To quantitatively determine their dependence, we first construct a histogram of all the L_d values at a period bin and consider the damping length corresponding to the peak of that histogram as the representative L_d value at that period bin. Thus obtained L_d values at each period bin are shown by black circles in Figure 6.3 (the errors are measured as the standard deviations of each distributions). These values are then fitted with a linear function (solid black line in the figure), the slope of which gives a measure of the dependence of damping length on the oscillation period. The obtained slope values are -0.3 ± 0.1, and -0.4 ± 0.1 for the plume and interplume structures, respectively, in the 171 Å

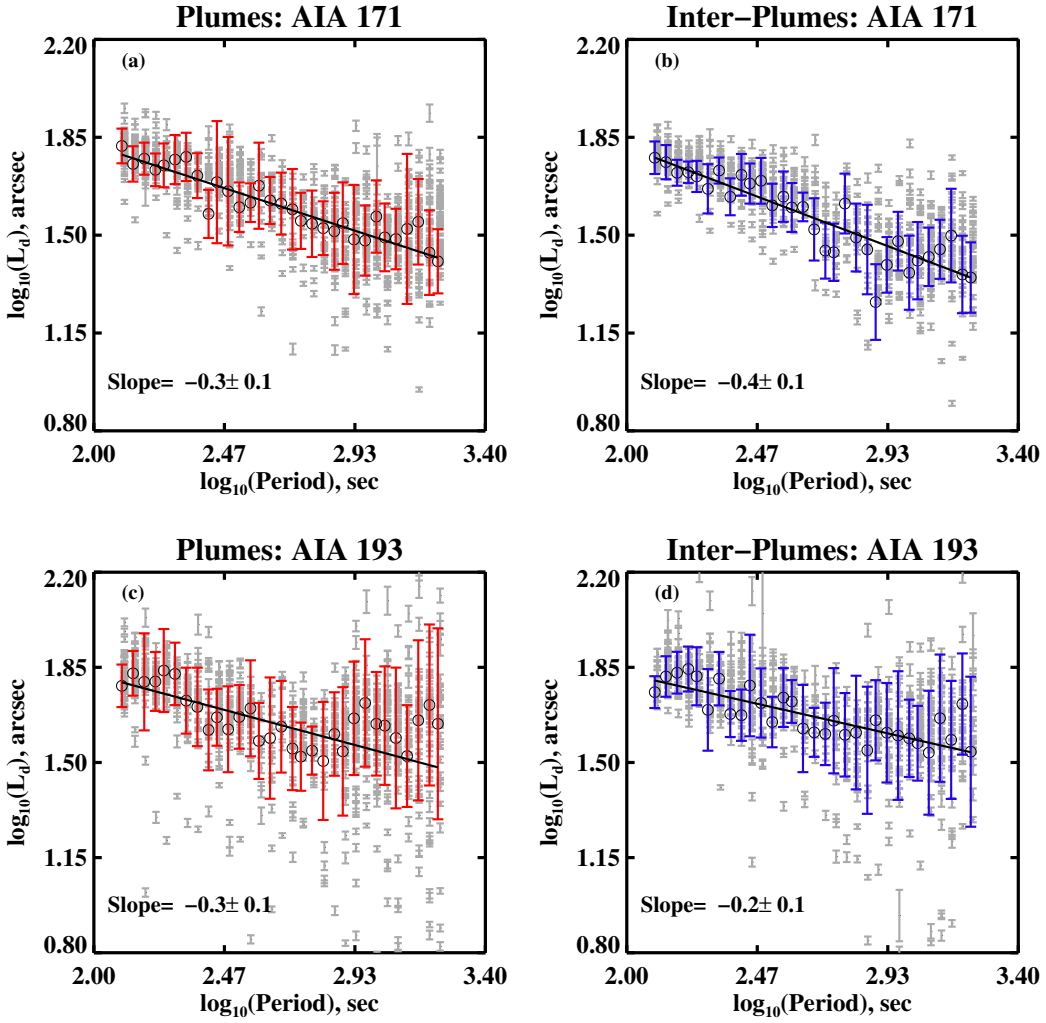

FIGURE 6.3: Damping length as a function of oscillation period in log-log scale. The top (bottom) panels display the results for the AIA 171 Å (193 Å) passband, while the left (right) panels show the results for plumes (interplumes). In each plot, the grey symbols represent the individual measurements whereas the black open circles denote the most frequent value for a given period. See the text for more details.

passband. The corresponding values in the 193 Å passband are -0.3 ± 0.1 and -0.2 ± 0.1 for the plume and interplume structures. For comparison, the slopes obtained by Krishna Prasad *et al.* (2014) are -0.3 ± 0.1 and -0.4 ± 0.1 in the 171 Å and the 193 Å passbands, respectively. Note that Krishna Prasad *et al.* did not obtain separate values for plume and interplume structures due to limited statistics. Nevertheless, the fact that the slopes obtained from a large statistics

in the present study are not very different from that reported by Krishna Prasad *et al.* from a single case study, implies, the observed anomalous dependence of damping length on oscillation period is a general characteristic of slow waves in polar regions.

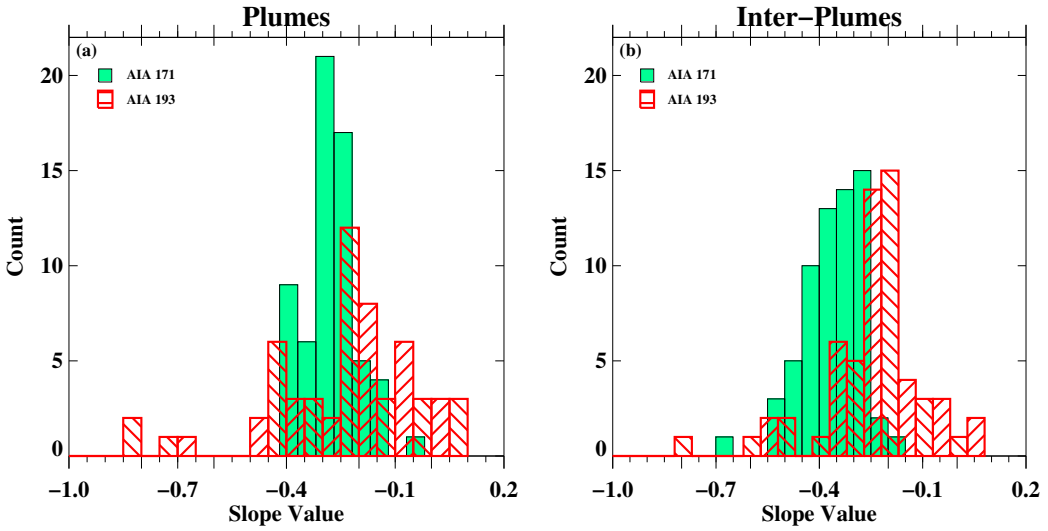

FIGURE 6.4: Distributions of the slope values obtained from damping length-period relation similar to that derived in Figure 6.3, but from individual datasets.

At this point, it is also intriguing to find out the range of the slope values by examining individual datasets. We, therefore, regroup the periods and corresponding damping lengths obtained from individual datasets and fit them separately to obtain respective slope values. Figure 6.4 displays the histograms of these values for plumes and interplumes. It appears the slope values in the 171 Å passband are narrowly distributed around -0.3 for plumes and skewed towards more negative values in interplumes. The corresponding values in the 193 Å passband show a relatively wider distribution even with a few cases of positive (but close to zero) values. A majority of the cases still show negative slopes but the peaks are shifted towards the less negative side compared to that in the 171 Å passband. In order to check the similarities between the distributions shown in Figure 6.4, we perform two non-parametric tests, namely Kolmogorov-Smirnov (K-S) test and the Mood test. The K-S test quantifies the distribution equivalence whereas the Mood test

checks for the equality of scale (Daniel 1990). All these tests have been performed using the statistical analysis software 'R' (Feigelson and Babu 2012). Both the K-S test results (D_{plume}=0.4, $D_{interplume}$=0.6 with P<0.001) and the Mood test results (P<0.001) indicate that the two distributions (panel(a) and panel(b) of Figure 6.4) are statistically different.

Let us now focus on the physical interpretation of the observed frequency dependence. The shorter damping lengths at the longer periods require the damping mechanism to be more efficient at low frequencies. Although there are several physical processes such as thermal conduction, compressive viscosity, radiation loss, gravitational stratification, magnetic field divergence, phase mixing, mode coupling etc., that could contribute to the damping of slow waves (De Moortel and Hood 2003, 2004; De Moortel *et al.* 2004), most of them are independent on frequency while a few (e.g., thermal conduction, compressive viscosity) are rather more efficient at high frequencies according to one-dimensional linear MHD wave theory (see Table 1 in Krishna Prasad *et al.* 2014). One possible scenario is that, a linear theory may not be a good scheme to describe slow waves in polar regions. In fact, Ofman *et al.* (2000) have used 1-D and 2-D MHD codes to study the nonlinear effects associated with slow wave damping in case of polar plumes and interplumes. These authors found that because of lesser plasma density, a stronger dissipation, in the non-linear damping regime, is expected in the interplumes as compared to the plumes. However, from our observations (see Figure 6.3) we do not find any significant difference in damping length values in these two regions. It is also interesting to note that the slope values too are not much different despite the plasma parameters like density, temperature (and their gradients) being quite different in plumes and in surrounding interplumes (Wilhelm 2006; Wilhelm *et al.* 2011). Furthermore, the fundamental mechanism through which the nonlinearly steepened slow waves are expected to dissipate is compressive viscosity which is mainly effective at high frequencies. So it is not yet clear what mechanism causes this unusual frequency dependence in the damping of slow waves. Perhaps, we

need a full three-dimensional description of slow waves to better understand their dissipation characteristics in polar regions.

6.4.3 Gaussian decay of amplitude

It has been shown that the amplitude of damping kink waves could be better described with a Gaussian profile rather than with the regularly used exponential profile (Pascoe *et al.* 2012, 2016). The strong damping observed in these waves is believed to be due to mode coupling (Pascoe *et al.* 2012; Hood *et al.* 2013) which is frequency dependent (Terradas *et al.* 2010). Although the equivalent theory and simulations are not available yet for slow waves, it is possible to check if the damping characteristics of slow waves show similar signatures. Indeed, Krishna Prasad *et al.* (2014) have shown (using a single example from a coronal loop) that for slow waves with longer periods, the amplitude decay is better approximated to a Gaussian function as compared to an exponential one. Using the large statistics available in this study, we explore this behavior by refitting the amplitude profiles (see Figure 6.1e) of all the detected periods with a Gaussian function (defined as $\mathrm{A(x) = A_0 \exp^{-x^2/L_d^2} + C}$). We note the corresponding χ^2 values as a measure of goodness of fit and compare them with analogous values obtained from the exponential function defined in section 6.3. It turns out that in only about 4% of the cases the Gaussian model fares better than the exponential model for the data from the 171 Å passband. This fraction is even less (<3%) for the data from the 193 Å passband. However, interestingly, the periodicities in all those cases were ≥20 min. To check for the robustness of the above results, we also fit the damping curves using the 'maximum likelihood estimation' (MLE) method and calculate the Akaike's 'An Information Criterion' (AIC) to choose between the models (the smaller the AIC, the better the fit). We use the 'mle'(includes 'optim' also) procedure in R to compute the parameters. Similar results were obtained

confirming our finding that the amplitude decay in a very few cases (with periods $\geq$ 20 min) appears to be a Gaussian-like rather than an exponential one.

In any case, at this point, we are inclined to believe that an exponential decay model is good enough to describe the damping of slow waves.

6.4.4 The power-law index

In the previous sections we have discussed how the power at distinct peak periods decreases with distance as a consequence of the damping of slow waves and compared them to study the frequency-dependence. However, it is also important to compare the relative levels of power at the full spectrum of frequencies with respect to each other particularly in the context of understanding MHD wave turbulence (Cranmer *et al.* 2015). One of the common ways to perform this is by fitting a power-law function (f^{α}) to the power spectra and noting the power-law index, α (Battams *et al.* 2017; Kolotkov *et al.* 2016). Such studies have been done in the past for different solar features: in chromospheric network and fibrils (Reardon *et al.* 2008); in active regions (Auchère *et al.* 2014); in polar plumes (Gupta 2014); in sunspot, moss and quite Sun (Ireland *et al.* 2015). In fact, Gupta (2014) studied the power-law behavior only at six locations in the polar region and found that it resembles a Kolmogorov-turbulence like behavior (Kolmogorov 1941). Utilizing the large database, in this study, we derive the power-law indices from intensities at several plume, interplume structures corresponding to the two AIA passbands. A pixel location at about 30″ away from the solar limb (guided by our previously selected artificial slits) is chosen for each plume, interplume structure. In order to minimize the effect of noise, we perform an averaging, during the power spectra generation processed, on a 5×5 pixel^2 area surrounding this location. This averaging, in this case, is done in Fourier domain i.e light curves from each of these pixels (within the mentioned 5×5 area) are subjected to Fourier analysis to get

the corresponding power spectrum and all these power spectra are then averaged to generate the final power spectra which is then fitted with a power-law function to get the power-law index. The locations closer to the limb are selected in order to get the power spectrum in full period range (Gupta 2014). While fitting the spectrum, we use statistical weights (i.e $1/\sqrt{\mathrm{y}}$) to minimize the effect of spurious power fluctuations around the higher frequencies. All the spectra have been fitted with a function $\mathrm{Y} = \mathrm{f}^{-\alpha} + \mathrm{C}$ where the constant term (C) represents the frequency-independent 'white-noise' tail. Panels (a-b) of Figure 6.5 show two representative final Fourier power spectra (in log-log scale) obtained from a plume and an interplume structure. The overplotted black solid curves represent the fitted functions. The obtained α values are also listed in the plot. We fit the spectra only upto 0.27mHz (60 min) keeping in mind that the duration, of every individual dataset, is 180 min. It may be noted that the α values derived in this way may have some influence from the chosen spatial binning of the data due to the autocorrelation and non-Gaussian noise.

We also constructed histograms of all the obtained α values to compare their distributions across different structures and passbands which are shown in panels (c-d) of Figure 6.5.The peak values from the respective data are listed in the plot. An immediate observation reveals that all these distributions (in different structures and passbands) are fairly similar despite the different plasma parameters and magnetic field values in these regions. As we note, though our distributions have peaks around $\alpha{\approx}{-}1.2$ but there are large number of occurrences close to $\alpha{=}{-}1.6$. Such an α value is probably a signature of the classical Kolmogorov like ($\alpha{=}{-}5/3$) turbulence (Kolmogorov 1941). On the other hand, Jiao *et al.* (2016) has shown that the peak at $\alpha{\approx}{-}1.2$ can also be interpreted as a signature of the underlying generation mechanism which these authors attribute to the chromospheric spicules. The presence of both the scenario, as found in this study, demands an in-depth study of the power law index in these coronal structures (in fact, turbulence driven coronal heating models show that turbulence can play a

major role in dissipating the wave energies into the surrounding medium (Cranmer *et al.* 2007; Verdini *et al.* 2010)). Nonetheless, our study reveals a wider spectrum of α values as opposed to the only 'Kolmogorov-like turbulence' case as found by Gupta (2014).

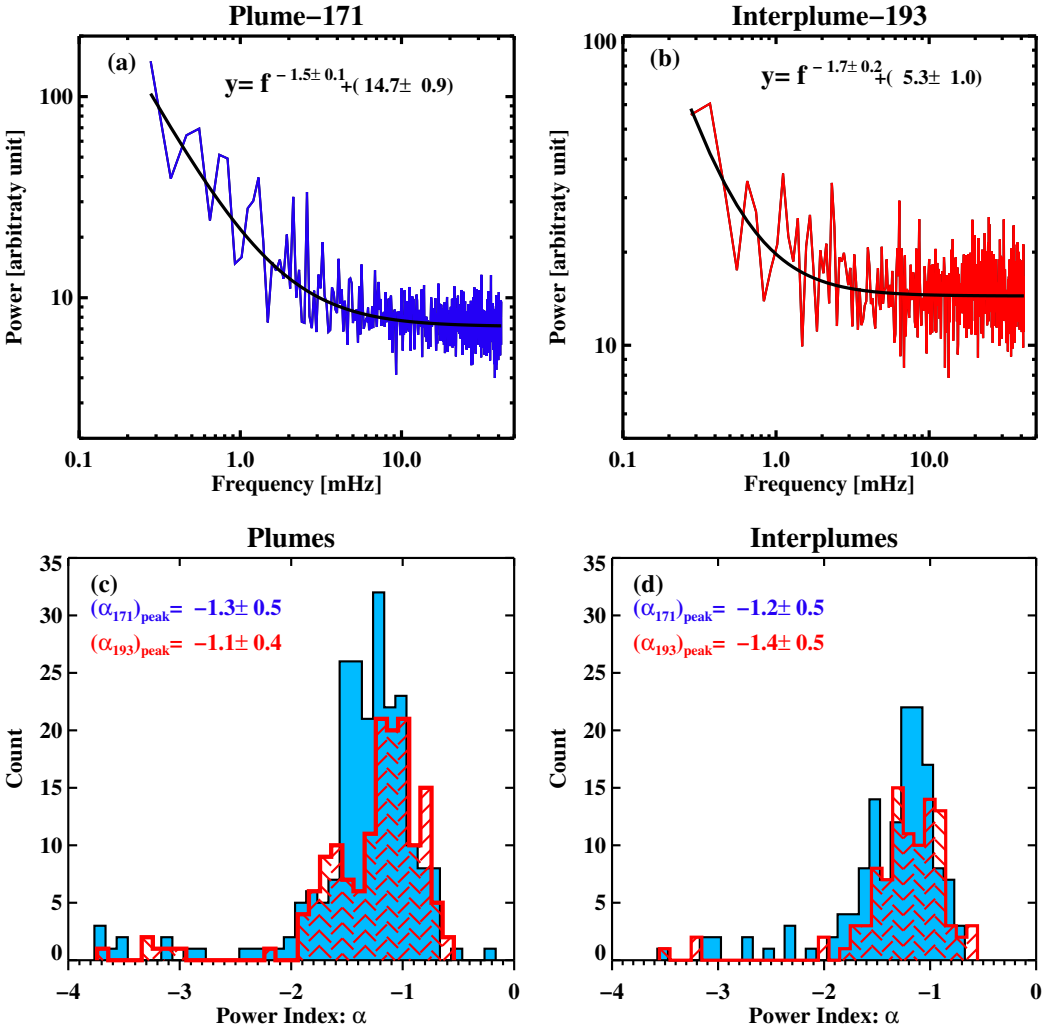

FIGURE 6.5: Panels (a-b) show two representative Fourier power spectra derived from the two AIA channels. The solid black curves represent the power-law fits, the indices of which are listed in the plot. The distributions of the power-law index (α), derived from all the datasets, are shown in panels (c-d) for different structures and passbands. Respective peak α values are printed on the panels.

6.5 Summary and Conclusions

Previous case studies indicate anomalous behavior with longer wave periods damping faster than the shorter ones. In this study, we use a large sample of polar region data, to extract the exact frequency dependence, along with other useful properties. Below we summarize the main results obtained from this study:

• Intensity oscillations, in polar regions, are usually observed at longer periods. However, we find, the short-period (2–6 min) oscillations are at least as abundant as the long-period (>7 min) ones in both plume and interplume structures. The larger power available at the long-period oscillations makes them readily apparent suppressing the shorter periods.

• The damping length and the oscillation period are weakly related through an inverse power-law function as previously found. The slope, as obtained by fitting the logarithmic values of these quantities, is -0.33 ± 0.05 for the plume and -0.38 ± 0.05 for the interplume structures, in the 171 Å passband. The corresponding values in the 193 Å passband are -0.28 ± 0.08 and -0.23 ± 0.07 for the plume and the interplume structures, respectively. The negative slopes could not be explained within the one-dimensional linear MHD description of slow waves. Future theoretical and numerical studies with full three-dimensional MHD are required.

• A comparison of slopes obtained from individual datasets show that the values in the 193 Å passband are mostly negative but lower indicating a shallow dependence. On the other hand, the data from interplumes in the 171 Å passband show steeper dependence for a majority of the cases.

• The decay of amplitude could be well described with an exponential function. A Gaussian profile was found to serve better only in about 4% of the cases, all of which correspond to longer periods (>20 min).

• Lastly, the Fourier power spectra near the limb show a power-law distribution with a peak close to α=−1.2, suggesting a possible connection between the lower atmosphere transients with the generation of the observed coronal slow waves (Jiao *et al.* 2016). However, significant number of cases around α=−5/3 perhaps indicate the physical nature of the underlying turbulence mechanism.

These results an also be useful to put some constraints on the numerical models of slow wave propagation and dissipation. Also, further studies are required to explore more about the effects of turbulence on the damping of slow waves.

Chapter 7

Conclusions & Future Work

Sun, as we know by now, is not a simple 'ball of fire' but rather made up of hot plasma which has distinct atmospheric structure. Infact, such stratifications in plasma density and temperature give rise to different solar features. The shapes and sizes of these features are also dictated by the magnetic field associated with these structures. Solar magnetic fields, which are believed to be coming out in the form of flux tubes, are continuously subjected to perturbations due to the convective motions in the photosphere. As these fields spread out in the atmosphere, they interact dynamically with the ambient field and the plasma. Such interactions lead to transient phenomenon such as small and large scale flares, CME's *etc*. Along with these, it also excites different MHD modes which propagate along (or across) various structures. Apart from being a tool to diagnose the host plasma properties, theoretical studies also reveal that these waves could play a pivotal role in solving the coronal heating problem. With the rapid advancement in technologies, we now have access to high resolution data which is revealing new finer structures, which further allows us to study the underlying physical mechanisms. In this thesis, we set out to explore different properties of slow waves using high resolution imaging and spectroscopic data. The main results along with the future

followup studies are presented in the following section.

7.1 Major Results & Future Directions

In the first section, we tried to identify a unique signature which can be used to distinctly identify the propagating disturbances (PDs) as slow waves or mass upflows. The major source of confusion arises due to the similar observable (such as intensity change or Doppler variations) that can be produced by any of these two scenarios. Using high resolution spectroscopic observations, we show that these PDs produce strong blueward R-B asymmetry (Tian *et al.* 2011b). Along with that, it also shows signatures of coherent oscillations in all three line parameters. These evidences support the idea of these PDs being the mass upflows whereas the analysis of imaging data promote the idea of slow waves as we demonstrated by the change in propagation speeds as we move to different temperature plasma. Thus, we concluded that with current instrumental capabilities it is difficult to isolate these two cases (wave and flows) from each other. De Moortel *et al.* (2015) pointed out, based on analytical calculation, that one can distinguish these two effects if the source region (*i.e* active region) can be observed at multiple LoS. Such limb to limb observations of active regions are not available currently, but observing proposal can be written to take up such investigations in future.

After investigating the nature of the PDs, we studied the source (or trigger) for such phenomena. We identified four unique events of slow wave reflections in coronal structures and analyzed multi-wavelength imaging data. The wave appears after a micro-flare occurs at one of the footpoints. In a detailed analysis on the generation mechanism, we find that the flare produces an ejecta and as soon as it gets detached from the source footpoints, it evolves as a wave. The DEM analysis, performed on the AIA data, show that the plasma temperature is

≈10 MK. Moreover, the estimated speed of propagation is comparable or lower than the local sound speed suggesting it to be a propagating slow wave. The other important aspect *i.e* wave damping is also explored and we find that the damping time is comparable to the wave period. To check the consistency of such reflection signatures with the obtained loop parameters, we perform a 2.5D MHD simulation, which uses the parameters obtained from our observation as inputs and performed forward modelling to synthesize AIA 94 Å images. Analyzing the synthesized images, we obtain the same properties of the observables as for the real observation. From the analysis we conclude that a footpoint heating can generate slow wave which then reflects back and forth in the coronal loop before fading out. Our analysis on the simulated data shows that the main agent for this damping is the anisotropic thermal conduction.

The role of thermal conduction in damping out the slow waves is not fully understood and we extend this investigation of slow wave damping by performing a 3-D MHD simulation, followed by forward modelling to explore the frequency dependent damping. Results show that the damping lengths vary linearly with the periods. We also measure the contributions of the emission properties on the damping lengths by using density values from the simulation and found that emission details are not so important for analyzing the power law behavior for these waves. These results are consistent with observational findings (Krishna Prasad *et al.* 2014) but contradicts the theoretical predictions. To resolve this issue, we analytically solve the slow wave dispersion and found that the assumption that 'lower thermal conduction limit' ($d\omega \ll 1$) is not valid for lower periods. Though our results can explain the observed frequency dependence seen in on-disc coronal loops but could not account for the power law behavior found in polar plumes and interplumes. Such a scenario point towards a different damping mechanism, other than the thermal conduction.

Next, we probe the statistical behavior of this damping mechanism by using high

resolution EUV multi-wavelength coronal imaging data from AIA 171 Å and AIA 193 Å channels. We found that the short-period (2–6 min) waves are relatively more abundant than their long period (7–30 min) counterparts in contrast to the general belief that the polar regions are dominated by the longer-period slow waves. We also derived the slope of the power spectra (α, the power-law index) statistically to better understand the characteristics of turbulence present in the region. It is found that the α values and their distributions are similar in both plume and interplume structures across the two AIA passbands. At the same time, the spread of these distributions also indicate the complexity of the underlying turbulence mechanisms.

In a followup study, we plan to conduct a further statistical study by tracking multiple active regions across their passage over the solar disc. This will also enable us to track the temporal change of slope values in the log-log period vs damping plot and this may be connected with the structural evolution. To explain the peculiar slope values, a full 3-D simulation with a stratified atmospheric model can also be perused in future.

Bibliography

Antolin, P. and Van Doorsselaere, T., 2013, "Line-of-sight geometrical and instrumental resolution effects on intensity perturbations by sausage modes", *Astron. Astrophys.*, **555**, A74. [DOI], [ADS], [arXiv:1303.6147 [astro-ph.SR]]

Antolin, P., Yokoyama, T. and Van Doorsselaere, T., 2014, "Fine Strand-like Structure in the Solar Corona from Magnetohydrodynamic Transverse Oscillations", *Astrophys. J. Lett.*, **787**, L22. [DOI], [ADS], [arXiv:1405.0076 [astro-ph.SR]]

Antolin, P., Vissers, G., Pereira, T. M. D., Rouppe van der Voort, L. and Scullion, E., 2015, "The Multithermal and Multi-stranded Nature of Coronal Rain", *Astrophys. J.*, **806**, 81. [DOI], [ADS], [arXiv:1504.04418 [astro-ph.SR]]

Aschwanden, M. J., 2005, *Physics of the Solar Corona. An Introduction with Problems and Solutions (2nd edition)*. [ADS]

Aschwanden, M. J., Fletcher, L., Schrijver, C. J. and Alexander, D., 1999a, "Coronal Loop Oscillations Observed with the Transition Region and Coronal Explorer", *Astrophys. J.*, **520**, 880–894. [DOI], [ADS]

Aschwanden, M. J., Newmark, J. S., Delaboudinière, J.-P., Neupert, W. M., Klimchuk, J. A., Gary, G. A., Portier-Fozzani, F. and Zucker, A., 1999b, "Three-dimensional Stereoscopic Analysis of Solar Active Region Loops. I. SOHO/EIT Observations at Temperatures of (1.0-1.5) $\times$ 10^6 K", *Astrophys. J.*, **515**, 842–867. [DOI], [ADS]

Aschwanden, M. J., Boerner, P., Schrijver, C. J. and Malanushenko, A., 2013, "Automated Temperature and Emission Measure Analysis of Coronal Loops and Active Regions Observed with the Atmospheric Imaging Assembly on the Solar Dynamics Observatory (SDO/AIA)", *Solar Phys.*, **283**, 5–30. [DOI], [ADS]

Auchère, F., Bocchialini, K., Solomon, J. and Tison, E., 2014, "Long-period intensity pulsations in the solar corona during activity cycle 23", *Astron. Astrophys.*, **563**, A8. [DOI], [ADS], [arXiv:1312.3792 [astro-ph.SR]]

Banerjee, D. and Krishna Prasad, S., 2016a, "MHD Waves in Coronal Holes", *Washington DC American Geophysical Union Geophysical Monograph Series*, **216**, 419–430. [DOI], [ADS], [arXiv:1505.04475 [astro-ph.SR]]

Banerjee, D. and Krishna Prasad, S., 2016b, "MHD Waves in Coronal Holes", *Washington DC American Geophysical Union Geophysical Monograph Series*, **216**, 419–430. [DOI], [ADS], [arXiv:1505.04475 [astro-ph.SR]]

Banerjee, D., O'Shea, E., Doyle, J. G. and Goossens, M., 2001, "Signatures of very long period waves in the polar coronal holes", *Astron. Astrophys.*, **380**, L39–L42. [DOI], [ADS]

Banerjee, D., Erdélyi, R., Oliver, R. and O'Shea, E., 2007, "Present and Future Observing Trends in Atmospheric Magnetoseismology", *Solar Phys.*, **246**, 3–29. [DOI], [ADS]

Banerjee, D., Gupta, G. R. and Teriaca, L., 2011, "Propagating MHD Waves in Coronal Holes", *Space Sci. Rev.*, **158**, 267–288. [DOI], [ADS], [arXiv:1009.2980 [astro-ph.SR]]

Battams, K., Gallagher, B. M. and Weigel, R. S., 2017, "A Global Survey of EUV Corona Power Spectra", *ArXiv e-prints*. [ADS], [arXiv:1707.02448 [astro-ph.SR]]

Berghmans, D and Clette, F, 1999, "Active region EUV transient brightenings–First Results by EIT of SOHO JOP 80", *Solar Physics*, **186**(1-2), 207–229

Boerner, P., Edwards, C., Lemen, J., Rausch, A., Schrijver, C., Shine, R., Shing, L., Stern, R., Tarbell, T., Title, A., Wolfson, C. J., Soufli, R., Spiller, E., Gullikson, E., McKenzie, D., Windt, D., Golub, L., Podgorski, W., Testa, P. and Weber, M., 2012, "Initial Calibration of the Atmospheric Imaging Assembly (AIA) on the Solar Dynamics Observatory (SDO)", *Solar Phys.*, **275**, 41–66. [DOI], [ADS]

Bogdan, T. J., Carlsson, M., Hansteen, V. H., McMurry, A., Rosenthal, C. S., Johnson, M., Petty-Powell, S., Zita, E. J., Stein, R. F., McIntosh, S. W. and Nordlund, Å., 2003, "Waves in the Magnetized Solar Atmosphere. II. Waves from Localized Sources in Magnetic Flux Concentrations", *Astrophys. J.*, **599**, 626–660. [DOI], [ADS]

Botha, G. J. J., Arber, T. D., Nakariakov, V. M. and Zhugzhda, Y. D., 2011, "Chromospheric Resonances above Sunspot Umbrae", *Astrophys. J.*, **728**, 84. [DOI], [ADS]

Brooks, D. H. and Warren, H. P., 2012, "The Coronal Source of Extreme-ultraviolet Line Profile Asymmetries in Solar Active Region Outflows", *Astrophys. J. Lett.*, **760**, L5. [DOI], [ADS], [arXiv:1210.1274 [astro-ph.SR]]

Bruno, R. and Carbone, V., 2013, "The Solar Wind as a Turbulence Laboratory", *Living Reviews in Solar Physics*, **10**, 2. [DOI], [ADS]

Calabro, B., McAteer, R. T. J. and Bloomfield, D. S., 2013, "Oscillatory Behavior in the Corona", *Solar Physics*, **286**(2), 405–415. [DOI]URL: `https://doi.org/10.1007/s11207-013-0283-y`

Chae, J. and Goode, P. R., 2015, "Acoustic Waves Generated by Impulsive Disturbances in a Gravitationally Stratified Medium", *Astrophys. J.*, **808**, 118. [DOI], [ADS]

Choudhuri, A. R., 2007, "An Elementary Introduction to Solar Dynamo Theory", in *Kodai School on Solar Physics*, (Eds.) Hasan, S. S., Banerjee, D., American Institute of Physics Conference Series, 919, [DOI], [ADS]

Colgan, J., Abdallah, Jr., J., Sherrill, M. E., Foster, M., Fontes, C. J. and Feldman, U., 2008, "Radiative Losses of Solar Coronal Plasmas", *Astrophys. J.*, **689**, 585-592. [DOI], [ADS]

Cooper, F. C., Nakariakov, V. M. and Tsiklauri, D., 2003, "Line-of-sight effects on observability of kink and sausage modes in coronal structures with imaging telescopes", *Astron. Astrophys.*, **397**, 765–770. [DOI], [ADS], [astro-ph/0207167]

Cranmer, S. R., van Ballegooijen, A. A. and Edgar, R. J., 2007, "Self-consistent Coronal Heating and Solar Wind Acceleration from Anisotropic Magnetohydrodynamic Turbulence", *Astrophys. J. Suppl.*, **171**, 520–551. [DOI], [ADS], [astro-ph/0703333]

Cranmer, S. R., Asgari-Targhi, M., Miralles, M. P., Raymond, J. C., Strachan, L., Tian, H. and Woolsey, L. N., 2015, "The role of turbulence in coronal heating and solar wind expansion", *Philosophical Transactions of the Royal Society of London Series A*, **373**, 20140 148–20140 148. [DOI], [ADS], [arXiv:1412.2307 [astro-ph.SR]]

Culhane, J. L., Harra, L. K., James, A. M., Al-Janabi, K., Bradley, L. J., Chaudry, R. A., Rees, K., Tandy, J. A., Thomas, P., Whillock, M. C. R., Winter, B., Doschek, G. A., Korendyke, C. M., Brown, C. M., Myers, S., Mariska, J., Seely, J., Lang, J., Kent, B. J., Shaughnessy, B. M., Young, P. R., Simnett, G. M., Castelli, C. M., Mahmoud, S., Mapson-Menard, H., Probyn, B. J., Thomas, R. J., Davila, J., Dere, K., Windt, D., Shea, J., Hagood, R., Moye, R., Hara, H., Watanabe, T., Matsuzaki, K., Kosugi, T., Hansteen, V. and Wikstol, Ø., 2007, "The EUV Imaging Spectrometer for Hinode", *Solar Phys.*, **243**, 19–61. [DOI], [ADS]

Daniel, Wayne, 1990, *Applied nonparametric statistics*, Duxbury/Thomson Learning, Australia Pacific Grove, CA

De Moortel, I., 2006, "Propagating magnetohydrodynamics waves in coronal loops", *Philosophical Transactions of the Royal Society of London Series A*, **364**, 461–472. [DOI], [ADS]

de Moortel, I., 2009, "Longitudinal Waves in Coronal Loops", *Space Sci. Rev.*, **149**, 65–81. [DOI], [ADS]

De Moortel, I. and Bradshaw, S. J., 2008, "Forward Modelling of Coronal Intensity Perturbations", *Solar Phys.*, **252**, 101–119. [DOI], [ADS]

De Moortel, I. and Hood, A. W., 2003, "The damping of slow MHD waves in solar coronal magnetic fields", *Astron. Astrophys.*, **408**, 755–765. [DOI], [ADS]

De Moortel, I. and Hood, A. W., 2004, "The damping of slow MHD waves in solar coronal magnetic fields. II. The effect of gravitational stratification and field line divergence", *Astron. Astrophys.*, **415**, 705–715. [DOI], [ADS]

De Moortel, I. and Nakariakov, V. M., 2012, "Magnetohydrodynamic waves and coronal seismology: an overview of recent results", *Philosophical Transactions of the Royal Society of London Series A*, **370**, 3193–3216. [DOI], [ADS], [arXiv:1202.1944 [astro-ph.SR]]

De Moortel, I., Ireland, J. and Walsh, R. W., 2000, "Observation of oscillations in coronal loops", *Astron. Astrophys.*, **355**, L23–L26. [ADS]

De Moortel, I., Hood, A. W., Gerrard, C. L. and Brooks, S. J., 2004, "The damping of slow MHD waves in solar coronal magnetic fields. III. The effect of mode coupling", *Astron. Astrophys.*, **425**, 741–752. [DOI], [ADS]

De Moortel, I., Antolin, P. and Van Doorsselaere, T., 2015, "Observational Signatures of Waves and Flows in the Solar Corona", *Solar Phys.*, **290**, 399–421. [DOI], [ADS]

De Pontieu, B. and McIntosh, S. W., 2010, "Quasi-periodic Propagating Signals in the Solar Corona: The Signature of Magnetoacoustic Waves or High-velocity

Upflows?", *Astrophys. J.*, **722**, 1013–1029. [DOI], [ADS], [arXiv:1008.5300 [astro-ph.SR]]

De Pontieu, B., Erdélyi, R. and James, S. P., 2004, "Solar chromospheric spicules from the leakage of photospheric oscillations and flows", *Nature*, **430**, 536–539. [DOI], [ADS]

De Pontieu, B., Erdélyi, R. and De Moortel, I., 2005, "How to Channel Photospheric Oscillations into the Corona", *Astrophys. J. Lett.*, **624**, L61–L64. [DOI], [ADS]

de Pontieu, B., McIntosh, S., Hansteen, V. H., Carlsson, M., Schrijver, C. J., Tarbell, T. D., Title, A. M., Shine, R. A., Suematsu, Y., Tsuneta, S., Katsukawa, Y., Ichimoto, K., Shimizu, T. and Nagata, S., 2007, "A Tale of Two Spicules: The Impact of Spicules on the Magnetic Chromosphere", *Pub. Astron. Soc. Japan*, **59**, S655–S662. [DOI], [ADS], [arXiv:0710.2934]

De Pontieu, B., McIntosh, S. W., Hansteen, V. H. and Schrijver, C. J., 2009, "Observing the Roots of Solar Coronal Heatingin the Chromosphere", *Astrophys. J. Lett.*, **701**, L1–L6. [DOI], [ADS], [arXiv:0906.5434 [astro-ph.SR]]

De Pontieu, B., McIntosh, S. W., Carlsson, M., Hansteen, V. H., Tarbell, T. D., Boerner, P., Martinez-Sykora, J., Schrijver, C. J. and Title, A. M., 2011, "The Origins of Hot Plasma in the Solar Corona", *Science*, **331**, 55–. [DOI], [ADS]

DeForest, C. E. and Gurman, J. B., 1998, "Observation of Quasi-periodic Compressive Waves in Solar Polar Plumes", *Astrophys. J. Lett.*, **501**, L217–L220. [DOI], [ADS]

Del Zanna, G., O'Dwyer, B. and Mason, H. E., 2011, "SDO AIA and Hinode EIS observations of "warm" loops", *Astron. Astrophys.*, **535**, A46. [DOI], [ADS]

Fang, X., Yuan, D., Van Doorsselaere, T., Keppens, R. and Xia, C., 2015, "Modeling of Reflective Propagating Slow-mode Wave in a Flaring Loop", *Astrophys. J.*, **813**, 33. [DOI], [ADS], [arXiv:1509.04536 [astro-ph.SR]]

Feigelson, E.D. and Babu, G.J., 2012, *Modern Statistical Methods for Astronomy: With R Applications*, Cambridge University PressURL: `https://books.google.co.in/books?id=M6O1yxpvf2gC`

Gibson, S., 2015, "Data-model comparison using FORWARD and CoMP", in *Polarimetry*, (Eds.) Nagendra, K. N., Bagnulo, S., Centeno, R., Jesús Martínez González, M., IAU Symposium, 305, [DOI], [ADS], [arXiv:1511.04416 [astro-ph.SR]]

Golub, L., Deluca, E., Austin, G., Bookbinder, J., Caldwell, D., Cheimets, P., Cirtain, J., Cosmo, M., Reid, P., Sette, A., Weber, M., Sakao, T., Kano, R., Shibasaki, K., Hara, H., Tsuneta, S., Kumagai, K., Tamura, T., Shimojo, M., McCracken, J., Carpenter, J., Haight, H., Siler, R., Wright, E., Tucker, J., Rutledge, H., Barbera, M., Peres, G. and Varisco, S., 2007, "The X-Ray Telescope (XRT) for the Hinode Mission", *Solar Phys.*, **243**, 63–86. [DOI], [ADS]

Gupta, G. R., 2014, "Observations of dissipation of slow magneto-acoustic waves in a polar coronal hole", *Astron. Astrophys.*, **568**, A96. [DOI], [ADS], [arXiv:1407.1017 [astro-ph.SR]]

Gupta, G. R., O'Shea, E., Banerjee, D., Popescu, M. and Doyle, J. G., 2009, "On the statistical detection of propagating waves in polar coronal holes", *Astron. Astrophys.*, **493**, 251–257. [DOI], [ADS], [arXiv:0902.2676 [astro-ph.SR]]

Gupta, G. R., Teriaca, L., Marsch, E., Solanki, S. K. and Banerjee, D., 2012, "Spectroscopic observations of propagating disturbances in a polar coronal hole: evidence of slow magneto-acoustic waves", *Astron. Astrophys.*, **546**, A93. [DOI], [ADS], [arXiv:1209.3524 [astro-ph.SR]]

Hara, H., Watanabe, T., Harra, L. K., Culhane, J. L., Young, P. R., Mariska, J. T. and Doschek, G. A., 2008, "Coronal Plasma Motions near Footpoints of Active Region Loops Revealed from Spectroscopic Observations with Hinode EIS", *Astrophys. J. Lett.*, **678**, L67–L71. [DOI], [ADS]

Hathaway, D. H., 2015, "The Solar Cycle", *Living Reviews in Solar Physics*, **12**, 4. [DOI], [ADS], [arXiv:1502.07020 [astro-ph.SR]]

Hood, A. W., Ruderman, M., Pascoe, D. J., De Moortel, I., Terradas, J. and Wright, A. N., 2013, "Damping of kink waves by mode coupling. I. Analytical treatment", *Astron. Astrophys.*, **551**, A39. [DOI], [ADS]

Ireland, J., McAteer, R. T. J. and Inglis, A. R., 2015, "Coronal Fourier Power Spectra: Implications for Coronal Seismology and Coronal Heating", *Astrophys. J.*, **798**, 1. [DOI], [ADS], [arXiv:1410.2171 [astro-ph.SR]]

Jiao, F., Xia, L., Li, B., Huang, Z., Li, X., Chandrashekhar, K., Mou, C. and Fu, H., 2015, "Sources of Quasi-periodic Propagating Disturbances above a Solar Polar Coronal Hole", *Astrophys. J. Lett.*, **809**, L17. [DOI], [ADS], [arXiv:1507.08440 [astro-ph.SR]]

Jiao, Fang-Ran, Xia, Li-Dong, Huang, Zheng-Hua, Li, Bo, Fu, Hui, Yuan, Ding and Chandrashekhar, Kalugodu, 2016, "Damping and power spectra of quasi-periodic intensity disturbances above a solar polar coronal hole", *Research in Astronomy and Astrophysics*, **16**(6), 093URL: `http://stacks.iop.org/1674-4527/16/i=6/a=008`

Judge, P., 2008, "An Explanation of the Solar Transition Region", *Astrophys. J. Lett.*, **683**, L87. [DOI], [ADS], [arXiv:0807.1706]

Kaniel, S. and Kovetz, A., 1967, "Schwarzschild's Criterion for Instability", *Physics of Fluids*, **10**, 1186–1193. [DOI], [ADS]

Keppens, R., Meliani, Z., van Marle, A. J., Delmont, P., Vlasis, A. and van der Holst, B., 2012, "Parallel, grid-adaptive approaches for relativistic hydro and magnetohydrodynamics", *Journal of Computational Physics*, **231**, 718–744. [DOI], [ADS]

Kiddie, G., 2014, *The propagation and damping of MHD waves in the solar atmosphere*, Ph.D. thesis, University of St. Andrews (United Kingdom)

Kiddie, G., De Moortel, I., Del Zanna, G., McIntosh, S. W. and Whittaker, I., 2012, "Propagating Disturbances in Coronal Loops: A Detailed Analysis of Propagation Speeds", *Solar Phys.*, **279**, 427–452. [DOI], [ADS], [arXiv:1205.0891 [astro-ph.SR]]

King, D. B., Nakariakov, V. M., Deluca, E. E., Golub, L. and McClements, K. G., 2003, "Propagating EUV disturbances in the Solar corona: Two-wavelength observations", *Astron. Astrophys.*, **404**, L1–L4. [DOI], [ADS]

Kitagawa, N., Yokoyama, T., Imada, S. and Hara, H., 2010, "Mode Identification of MHD Waves in an Active Region Observed with Hinode/EIS", *Astrophys. J.*, **721**, 744–749. [DOI], [ADS], [arXiv:1008.1823 [astro-ph.SR]]

Kolmogorov, A., 1941, "The Local Structure of Turbulence in Incompressible Viscous Fluid for Very Large Reynolds' Numbers", *Akademiia Nauk SSSR Doklady*, **30**, 301–305. [ADS]

Kolotkov, D. Y., Anfinogentov, S. A. and Nakariakov, V. M., 2016, "Empirical mode decomposition analysis of random processes in the solar atmosphere", *Astron. Astrophys.*, **592**, A153. [DOI], [ADS]

Kosugi, T., Matsuzaki, K., Sakao, T., Shimizu, T., Sone, Y., Tachikawa, S., Hashimoto, T., Minesugi, K., Ohnishi, A., Yamada, T., Tsuneta, S., Hara, H., Ichimoto, K., Suematsu, Y., Shimojo, M., Watanabe, T., Shimada, S., Davis, J. M., Hill, L. D., Owens, J. K., Title, A. M., Culhane, J. L., Harra, L. K., Doschek, G. A. and Golub, L., 2007, "The Hinode (Solar-B) Mission: An Overview", *Solar Phys.*, **243**, 3–17. [DOI], [ADS]

Krishna Prasad, S., Banerjee, D. and Gupta, G. R., 2011, "Propagating intensity disturbances in polar corona as seen from AIA/SDO", *Astron. Astrophys.*, **528**, L4. [DOI], [ADS], [arXiv:1102.2979 [astro-ph.SR]]

Krishna Prasad, S., Banerjee, D. and Singh, J., 2012a, "Oscillations in Active Region Fan Loops: Observations from EIS/ Hinode and AIA/SDO", *Solar Phys.*, **281**, 67–85. [DOI], [ADS], [arXiv:1208.1377 [astro-ph.SR]]

Krishna Prasad, S., Banerjee, D., Van Doorsselaere, T. and Singh, J., 2012b, "Omnipresent long-period intensity oscillations in open coronal structures", *Astron. Astrophys.*, **546**, A50. [DOI], [ADS], [arXiv:1209.2536 [astro-ph.SR]]

Krishna Prasad, S., Banerjee, D. and Van Doorsselaere, T., 2014, "Frequency-dependent Damping in Propagating Slow Magneto-acoustic Waves", *Astrophys. J.*, **789**, 118. [DOI], [ADS], [arXiv:1406.3565 [astro-ph.SR]]

Krishna Prasad, S., Jess, D. B. and Khomenko, E., 2015, "On the Source of Propagating Slow Magnetoacoustic Waves in Sunspots", *Astrophys. J. Lett.*, **812**, L15. [DOI], [ADS], [arXiv:1510.03275 [astro-ph.SR]]

Kumar, P., Innes, D. E. and Inhester, B., 2013, "Solar Dynamics Observatory/Atmospheric Imaging Assembly Observations of a Reflecting Longitudinal Wave in a Coronal Loop", *Astrophys. J. Lett.*, **779**, L7. [DOI], [ADS], [arXiv:1409.3896 [astro-ph.SR]]

Kumar, P., Nakariakov, V. M. and Cho, K.-S., 2015, "X-Ray and EUV Observations of Simultaneous Short and Long Period Oscillations in Hot Coronal Arcade Loops", *Astrophys. J.*, **804**, 4. [DOI], [ADS], [arXiv:1502.07117 [astro-ph.SR]]

Lemen, J. R., Title, A. M., Akin, D. J., Boerner, P. F., Chou, C., Drake, J. F., Duncan, D. W., Edwards, C. G., Friedlaender, F. M., Heyman, G. F., Hurlburt, N. E., Katz, N. L., Kushner, G. D., Levay, M., Lindgren, R. W., Mathur, D. P., McFeaters, E. L., Mitchell, S., Rehse, R. A., Schrijver, C. J., Springer, L. A., Stern, R. A., Tarbell, T. D., Wuelser, J.-P., Wolfson, C. J., Yanari, C., Bookbinder, J. A., Cheimets, P. N., Caldwell, D., Deluca, E. E., Gates, R., Golub, L., Park, S., Podgorski, W. A., Bush, R. I., Scherrer, P. H., Gummin, M. A., Smith, P., Auker, G., Jerram, P., Pool, P., Soufli, R., Windt, D. L., Beardsley, S., Clapp, M., Lang, J. and Waltham, N., 2012, "The Atmospheric Imaging Assembly (AIA) on the Solar Dynamics Observatory (SDO)", *Solar Phys.*, **275**, 17–40. [DOI], [ADS]

Mandal, S., Samanta, T., Banerjee, D., Krishna Prasad, S. and Teriaca, L., 2015, "Propagating disturbances along fan-like coronal loops in an active region", *Research in Astronomy and Astrophysics*, **15**, 1832. [DOI], [ADS], [arXiv:1505.04710 [astro-ph.SR]]

Mandal, S., Magyar, N., Yuan, D., Van Doorsselaere, T. and Banerjee, D., 2016a, "Forward Modeling of Propagating Slow Waves in Coronal Loops and Their Frequency-dependent Damping", *Astrophys. J.*, **820**, 13. [DOI], [ADS], [arXiv:1602.00787 [astro-ph.SR]]

Mandal, S., Yuan, D., Fang, X., Banerjee, D., Pant, V. and Van Doorsselaere, T., 2016b, "Reflection of Propagating Slow Magneto-acoustic Waves in Hot Coronal Loops: Multi-instrument Observations and Numerical Modeling", *Astrophys. J.*, **828**, 72. [DOI], [ADS], [arXiv:1604.08133 [astro-ph.SR]]

Mandal, S., Krishna Prasad, S. and Banerjee, D., 2018, "A Statistical Study on the Frequency-dependent Damping of the Slow-mode Waves in Polar Plumes and Interplumes", *Astrophys. J.*, **853**, 134. [DOI], [ADS]

Mariska, J. T., 2005, "Observations of Solar Flare Doppler Shift Oscillations with the Bragg Crystal Spectrometer on Yohkoh", *Astrophys. J. Lett.*, **620**, L67–L70. [DOI], [ADS], [astro-ph/0501093]

Mariska, J. T., 2006, "Characteristics of Solar Flare Doppler-Shift Oscillations Observed with the Bragg Crystal Spectrometer on Yohkoh", *Astrophys. J.*, **639**, 484–494. [DOI], [ADS], [astro-ph/0511070]

Marsh, M. S. and Walsh, R. W., 2009, "Using HINODE/Extreme-Ultraviolet Imaging Spectrometer to Confirm a Seismologically Inferred Coronal Temperature", *Astrophys. J. Lett.*, **706**, L76–L79. [DOI], [ADS], [arXiv:0910.3823 [astro-ph.SR]]

Marsh, M. S., Walsh, R. W. and Plunkett, S., 2009, "Three-dimensional Coronal Slow Modes: Toward Three-dimensional Seismology", *Astrophys. J.*, **697**, 1674–1680. [DOI], [ADS], [arXiv:0903.4039 [astro-ph.SR]]

Martínez-Sykora, J., De Pontieu, B., Hansteen, V. and McIntosh, S. W., 2011, "What do Spectral Line Profile Asymmetries Tell us About the Solar Atmosphere?", *Astrophys. J.*, **732**, 84. [DOI], [ADS]

Moore, R. L., Sterling, A. C., Falconer, D. A. and Robe, D., 2013, "The Cool Component and the Dichotomy, Lateral Expansion, and Axial Rotation of Solar X-Ray Jets", *Astrophys. J.*, **769**, 134. [DOI], [ADS]

Mueller, D., Dimitoglou, G., Caplins, B., Garcia Ortiz, J. P., Wamsler, B., Hughitt, K., Alexanderian, A., Ireland, J., Amadigwe, D. and Fleck, B., 2013, "JHelioviewer: Visualization software for solar physics data", [ADS]

Nakariakov, V. M. and Ofman, L., 2001, "Determination of the coronal magnetic field by coronal loop oscillations", *Astron. Astrophys.*, **372**, L53–L56. [DOI], [ADS]

Nakariakov, V. M., Ofman, L., Deluca, E. E., Roberts, B. and Davila, J. M., 1999, "TRACE observation of damped coronal loop oscillations: Implications for coronal heating", *Science*, **285**, 862–864. [DOI], [ADS]

Nakariakov, Valery M. and Verwichte, Erwin, 2005, "Coronal Waves and Oscillations", *Living Reviews in Solar Physics*, **2**(3). [DOI]URL: `http://www.livingreviews.org/lrsp-2005-3`

Nightingale, R. W., Aschwanden, M. J. and Hurlburt, N. E., 1999, "Time Variability of EUV Brightenings in Coronal Loops Observed with TRACE", *Solar Phys.*, **190**, 249–265. [DOI], [ADS]

Nightingale, Richard W, Aschwanden, Markus J and Hurlburt, Neal E, 2000, "Time variability of EUV brightenings in coronal loops observed with TRACE", in *Physics of the Solar Corona and Transition Region*, pp. 249–265, Springer

Nishizuka, N. and Hara, H., 2011, "Spectroscopic Observations of Continuous Outflows and Propagating Waves from NOAA 10942 with Extreme Ultraviolet Imaging Spectrometer/Hinode", *Astrophys. J. Lett.*, **737**, L43. [DOI], [ADS]

Nita, G. M., Fleishman, G. D., Kuznetsov, A. A., Kontar, E. P. and Gary, D. E., 2015, "Three-dimensional Radio and X-Ray Modeling and Data Analysis Software: Revealing Flare Complexity", *Astrophys. J.*, **799**, 236. [DOI], [ADS], [arXiv:1409.0896 [astro-ph.SR]]

Ofman, L. and Selwa, M., 2009, "Three-dimensional MHD modeling of waves in active region loops", in *IAU Symposium*, (Eds.) Gopalswamy, N., Webb, D. F., IAU Symposium, 257, [DOI], [ADS]

Ofman, L. and Wang, T., 2002, "Hot Coronal Loop Oscillations Observed by SUMER: Slow Magnetosonic Wave Damping by Thermal Conduction", *Astrophys. J. Lett.*, **580**, L85–L88. [DOI], [ADS]

Ofman, L., Romoli, M., Poletto, G., Noci, G. and Kohl, J. L., 1997, "Ultraviolet Coronagraph Spectrometer Observations of Density Fluctuations in the Solar Wind", *Astrophys. J. Lett.*, **491**, L111–L114. [DOI], [ADS]

Ofman, L., Nakariakov, V. M. and Sehgal, N., 2000, "Dissipation of Slow Magnetosonic Waves in Coronal Plumes", *Astrophys. J.*, **533**, 1071–1083. [DOI], [ADS]

Ofman, L., Wang, T. J. and Davila, J. M., 2012, "Slow Magnetosonic Waves and Fast Flows in Active Region Loops", *Astrophys. J.*, **754**, 111. [DOI], [ADS], [arXiv:1205.5732 [astro-ph.SR]]

Parker, E. N., 1958, "Dynamics of the Interplanetary Gas and Magnetic Fields.", *Astrophys. J.*, **128**, 664. [DOI], [ADS]

Pascoe, D. J., Hood, A. W., de Moortel, I. and Wright, A. N., 2012, "Spatial damping of propagating kink waves due to mode coupling", *Astron. Astrophys.*, **539**, A37. [DOI], [ADS]

Pascoe, D. J., Goddard, C. R., Nisticò, G., Anfinogentov, S. and Nakariakov, V. M., 2016, "Damping profile of standing kink oscillations observed by SDO/AIA", *Astron. Astrophys.*, **585**, L6. [DOI], [ADS]

Pesnell, W. D., Thompson, B. J. and Chamberlin, P. C., 2012, "The Solar Dynamics Observatory (SDO)", *Solar Phys.*, **275**, 3–15. [DOI], [ADS]

Podladchikova, O., Vourlidas, A., Van der Linden, R. A. M., Wülser, J.-P. and Patsourakos, S., 2010, "Extreme Ultraviolet Observations and Analysis of Micro-Eruptions and Their Associated Coronal Waves", *Astrophys. J.*, **709**, 369–376. [DOI], [ADS]

Poedts, S., 2002, "MHD waves and heating of the solar corona", in *SOLMAG 2002. Proceedings of the Magnetic Coupling of the Solar Atmosphere Euroconference*, (Ed.) Sawaya-Lacoste, H., ESA Special Publication, 505, [ADS]

Poletto, G., 2015, "Solar Coronal Plumes", *Living Reviews in Solar Physics*, **12**, 7. [DOI], [ADS]

Porth, O., Xia, C., Hendrix, T., Moschou, S. P. and Keppens, R., 2014, "MPI-AMRVAC for Solar and Astrophysics", *Astrophys. J. Suppl.*, **214**, 4. [DOI], [ADS], [arXiv:1407.2052 [astro-ph.IM]]

Priest, E., 2014, *Magnetohydrodynamics of the Sun*. [ADS]

Reardon, K. P., Lepreti, F., Carbone, V. and Vecchio, A., 2008, "Evidence of Shock-driven Turbulence in the Solar Chromosphere", *Astrophys. J. Lett.*, **683**, L207. [DOI], [ADS], [arXiv:0809.4243]

Roberts, B., 2000, "Waves and Oscillations in the Corona - (Invited Review)", *Solar Phys.*, **193**, 139–152. [DOI], [ADS]

Roberts, B., Edwin, P. M. and Benz, A. O., 1984, "On coronal oscillations", *Astrophys. J.*, **279**, 857–865. [DOI], [ADS]

Sakurai, T., 2017, "Heating mechanisms of the solar corona", *Proceeding of the Japan Academy, Series B*, **93**, 87–97. [DOI], [ADS]

Samanta, T., Pant, V. and Banerjee, D., 2015, "Propagating Disturbances in the Solar Corona and Spicular Connection", *Astrophys. J. Lett.*, **815**, L16. [DOI], [ADS], [arXiv:1511.07354 [astro-ph.SR]]

Schou, J., Scherrer, P. H., Bush, R. I., Wachter, R., Couvidat, S., Rabello-Soares, M. C., Bogart, R. S., Hoeksema, J. T., Liu, Y., Duvall, T. L., Akin, D. J., Allard, B. A., Miles, J. W., Rairden, R., Shine, R. A., Tarbell, T. D., Title, A. M., Wolfson, C. J., Elmore, D. F., Norton, A. A. and Tomczyk, S., 2012, "Design and Ground Calibration of the Helioseismic and Magnetic Imager (HMI) Instrument on the Solar Dynamics Observatory (SDO)", *Solar Phys.*, **275**, 229–259. [DOI], [ADS]

Sechler, M., McIntosh, S. W., Tian, H. and De Pontieu, B., 2012, "Hinode/EIS Line Profile Asymmetries and Their Relationship with the Distribution of SDO/AIA Propagating Coronal Disturbance Velocities", in *4th Hinode Science Meeting: Unsolved Problems and Recent Insights*, (Eds.) Bellot Rubio, L., Reale, F., Carlsson, M., Astronomical Society of the Pacific Conference Series, 455, [ADS], [arXiv:1201.5028 [astro-ph.SR]]

Selwa, M. and Ofman, L., 2009, "3-D numerical simulations of coronal loops oscillations", *Annales Geophysicae*, **27**, 3899–3908. [DOI], [ADS]

Selwa, M., Murawski, K. and Solanki, S. K., 2005, "Excitation and damping of slow magnetosonic standing waves in a solar coronal loop", *Astron. Astrophys.*, **436**, 701–709. [DOI], [ADS]

Selwa, M., Ofman, L. and Murawski, K., 2007, "Numerical Simulations of Slow Standing Waves in a Curved Solar Coronal Loop", *Astrophys. J. Lett.*, **668**, L83–L86. [DOI], [ADS]

Srivastava, A. K. and Dwivedi, B. N., 2010, "Observations from Hinode/EIS of intensity oscillations above a bright point: signature of the leakage of acoustic oscillations in the inner corona", *Mon. Not. Roy. Astron. Soc.*, **405**, 2317–2326. [DOI], [ADS]

Sterling, A. C., Moore, R. L., Falconer, D. A. and Adams, M., 2015, "Small-scale filament eruptions as the driver of X-ray jets in solar coronal holes", *Nature*, **523**, 437–440. [DOI], [ADS]

Su, J. T., 2014, "Statistical Detection of Slow-mode Waves in Solar Polar Regions with SDO/AIA", *Astrophys. J.*, **793**, 117. [DOI], [ADS]

Terradas, J., Goossens, M. and Verth, G., 2010, "Selective spatial damping of propagating kink waves due to resonant absorption", *Astron. Astrophys.*, **524**, A23. [DOI], [ADS], [arXiv:1004.4468 [astro-ph.SR]]

Tian, H., McIntosh, S. W. and De Pontieu, B., 2011a, "The Spectroscopic Signature of Quasi-periodic Upflows in Active Region Timeseries", *Astrophys. J. Lett.*, **727**, L37. [DOI], [ADS], [arXiv:1012.5112 [astro-ph.SR]]

Tian, H., McIntosh, S. W., De Pontieu, B., Martínez-Sykora, J., Sechler, M. and Wang, X., 2011b, "Two Components of the Solar Coronal Emission Revealed by Extreme-ultraviolet Spectroscopic Observations", *Astrophys. J.*, **738**, 18. [DOI], [ADS], [arXiv:1106.1141 [astro-ph.SR]]

Tian, H., McIntosh, S. W., Wang, T., Ofman, L., De Pontieu, B., Innes, D. E. and Peter, H., 2012, "Persistent Doppler Shift Oscillations Observed with Hinode/EIS in the Solar Corona: Spectroscopic Signatures of Alfvénic Waves and Recurring Upflows", *Astrophys. J.*, **759**, 144. [DOI], [ADS], [arXiv:1209.5286 [astro-ph.SR]]

Tomczyk, S., McIntosh, S. W., Keil, S. L., Judge, P. G., Schad, T., Seeley, D. H. and Edmondson, J., 2007, "Alfvén Waves in the Solar Corona", *Science*, **317**, 1192. [DOI], [ADS]

Torrence, C. and Compo, G. P., 1998, "A Practical Guide to Wavelet Analysis.", *Bulletin of the American Meteorological Society*, **79**, 61–78. [DOI], [ADS]

Tripathi, D. and Klimchuk, J. A., 2013, "Asymmetries in Coronal Spectral Lines and Emission Measure Distribution", *Astrophys. J.*, **779**, 1. [DOI], [ADS], [arXiv:1310.0168 [astro-ph.SR]]

Tripathi, D., Mason, H. E., Del Zanna, G. and Bradshaw, S., 2012, "Observations of Plasma Upflow in a Warm Loop with Hinode/EIS", *Astrophys. J. Lett.*, **754**, L4. [DOI], [ADS], [arXiv:1206.3367 [astro-ph.SR]]

Ugarte-Urra, I. and Warren, H. P., 2011, "Temporal Variability of Active Region Outflows", *Astrophys. J.*, **730**, 37. [DOI], [ADS], [arXiv:1008.4730 [astro-ph.SR]]

Van Doorsselaere, T., Wardle, N., Del Zanna, G., Jansari, K., Verwichte, E. and Nakariakov, V. M., 2011, "The First Measurement of the Adiabatic Index in the Solar Corona Using Time-dependent Spectroscopy of Hinode/EIS Observations", *Astrophys. J. Lett.*, **727**, L32. [DOI], [ADS]

Van Doorsselaere, T., Antolin, P., Yuan, D., Reznikova, V. and Magyar, N., 2016, "Forward modelling of optically thin coronal plasma with the FoMo tool", *Frontiers in Astronomy and Space Sciences*, **3**, 4. [DOI], [ADS]

Verdini, A., Velli, M., Matthaeus, W. H., Oughton, S. and Dmitruk, P., 2010, "A Turbulence-Driven Model for Heating and Acceleration of the Fast Wind in Coronal Holes", *Astrophys. J. Lett.*, **708**, L116–L120. [DOI], [ADS], [arXiv:0911.5221 [astro-ph.SR]]

Verwichte, E., Marsh, M., Foullon, C., Van Doorsselaere, T., De Moortel, I., Hood, A. W. and Nakariakov, V. M., 2010, "Periodic Spectral Line Asymmetries in Solar Coronal Structures from Slow Magnetoacoustic Waves", *Astrophys. J. Lett.*, **724**, L194–L198. [DOI], [ADS]

Verwichte, E., Van Doorsselaere, T., White, R. S. and Antolin, P., 2013, "Statistical seismology of transverse waves in the solar corona", *Astron. Astrophys.*, **552**, A138. [DOI], [ADS]

Voitenko, Y., Andries, J., Copil, P. D. and Goossens, M., 2005, "Damping of phase-mixed slow magneto-acoustic waves: Real or apparent?", *Astron. Astrophys.*, **437**, L47–L50. [DOI], [ADS]

Wang, T., 2011, "Standing Slow-Mode Waves in Hot Coronal Loops: Observations, Modeling, and Coronal Seismology", *Space Sci. Rev.*, **158**, 397–419. [DOI], [ADS], [arXiv:1011.2483 [astro-ph.SR]]

Wang, T., Solanki, S. K., Curdt, W., Innes, D. E. and Dammasch, I. E., 2002, "Doppler Shift Oscillations of Hot Solar Coronal Plasma Seen by SUMER: A Signature of Loop Oscillations?", *Astrophys. J. Lett.*, **574**, L101–L104. [DOI], [ADS]

Wang, T., Innes, D. E. and Qiu, J., 2007, "Determination of the Coronal Magnetic Field from Hot-Loop Oscillations Observed by SUMER and SXT", *Astrophys. J.*, **656**, 598–609. [DOI], [ADS], [astro-ph/0612566]

Wang, T., Ofman, L. and Davila, J. M., 2012, "Spectroscopic Diagnosis of Propagating Disturbances in Coronal Loops: Waves or flows?", in *Fifth Hinode Science Meeting*, (Eds.) Golub, L., De Moortel, I., Shimizu, T., Astronomical Society of the Pacific Conference Series, 456, [ADS]

Wang, T. J., Solanki, S. K., Curdt, W., Innes, D. E., Dammasch, I. E. and Kliem, B., 2003a, "Hot coronal loop oscillations observed with SUMER: Examples and statistics", *Astron. Astrophys.*, **406**, 1105–1121. [DOI], [ADS]

Wang, T. J., Solanki, S. K., Innes, D. E., Curdt, W. and Marsch, E., 2003b, "Slow-mode standing waves observed by SUMER in hot coronal loops", *Astron. Astrophys.*, **402**, L17–L20. [DOI], [ADS]

Wang, T. J., Solanki, S. K., Innes, D. E. and Curdt, W., 2005, "Initiation of hot coronal loop oscillations: Spectral features", *Astron. Astrophys.*, **435**, 753–764. [DOI], [ADS]

Wang, T. J., Ofman, L. and Davila, J. M., 2009a, "Propagating Slow Magnetoacoustic Waves in Coronal Loops Observed by Hinode/EIS", *Astrophys. J.*, **696**, 1448–1460. [DOI], [ADS], [arXiv:0902.4480 [astro-ph.SR]]

Wang, T. J., Ofman, L., Davila, J. M. and Mariska, J. T., 2009b, "Hinode/EIS observations of propagating low-frequency slow magnetoacoustic waves in fan-like coronal loops", *Astron. Astrophys.*, **503**, L25–L28. [DOI], [ADS], [arXiv:0908.0310 [astro-ph.SR]]

Wilhelm, K., 2006, "Solar coronal-hole plasma densities and temperatures", *Astron. Astrophys.*, **455**, 697–708. [DOI], [ADS]

Wilhelm, K., Abbo, L., Auchère, F., Barbey, N., Feng, L., Gabriel, A. H., Giordano, S., Imada, S., Llebaria, A., Matthaeus, W. H., Poletto, G., Raouafi, N.-E., Suess, S. T., Teriaca, L. and Wang, Y.-M., 2011, "Morphology, dynamics and plasma parameters of plumes and inter-plume regions in solar coronal holes", *Astron. Astrophys. Rev.*, **19**. [DOI], [ADS], [arXiv:1103.4481 [astro-ph.SR]]

Xia, C., Chen, P. F. and Keppens, R., 2012, "Simulations of Prominence Formation in the Magnetized Solar Corona by Chromospheric Heating", *Astrophys. J. Lett.*, **748**, L26. [DOI], [ADS], [arXiv:1202.6185 [astro-ph.SR]]

Young, P. R., Watanabe, T., Hara, H. and Mariska, J. T., 2009, "High-precision density measurements in the solar corona. I. Analysis methods and results for Fe XII and Fe XIII", *Astron. Astrophys.*, **495**, 587–606. [DOI], [ADS], [arXiv:0805.0958]

Yuan, D. and Nakariakov, V. M., 2012, "Measuring the apparent phase speed of propagating EUV disturbances", *Astron. Astrophys.*, **543**, A9. [DOI], [ADS]

Yuan, D., Van Doorsselaere, T., Banerjee, D. and Antolin, P., 2015, "Forward Modeling of Standing Slow Modes in Flaring Coronal Loops", *Astrophys. J.*, **807**, 98. [DOI], [ADS], [arXiv:1504.07475 [astro-ph.SR]]

Yuan, D., Su, J., Jiao, F. and Walsh, R. W., 2016, "Stochastic Transients as a Source of Quasi-periodic Processes in the Solar Atmosphere", *Astrophys. J. Suppl.*, **224**, 30. [DOI], [ADS], [arXiv:1603.08977 [astro-ph.SR]]

Zhang, J. and Wang, J., 2001, "Filament Eruptions and Halo Coronal Mass Ejections", *Astrophys. J.*, **554**, 474–487. [DOI], [ADS]